

1-1-2009

Fatigue damage assessment of particle-reinforced metal matrix composite materials under uniaxial and multiaxial loading conditions

Christopher E. Sutton
Ryerson University

Follow this and additional works at: <http://digitalcommons.ryerson.ca/dissertations>



Part of the [Aerospace Engineering Commons](#)

Recommended Citation

Sutton, Christopher E., "Fatigue damage assessment of particle-reinforced metal matrix composite materials under uniaxial and multiaxial loading conditions" (2009). *Theses and dissertations*. Paper 973.

011575112

FATIGUE DAMAGE ASSESSMENT OF PARTICLE-REINFORCED METAL MATRIX COMPOSITE MATERIALS UNDER UNIAXIAL AND MULTIAXIAL LOADING CONDITIONS

By

Christopher E. Sutton

Bachelor of Engineering in Aerospace Engineering

Ryerson University, June 2007

A thesis to the Ryerson University

In fulfillment of the thesis requirement for the degree of

Master of Applied Science

in

Aerospace Engineering

Toronto, Ontario, Canada, 2009

© Christopher E. Sutton

AUTHOR'S DECLARATION

I hereby declare that I am the sole author of this thesis.

I authorize the Ryerson University to lend this thesis to other institutions or individuals for the purpose of scholarly research.



I further authorize the Ryerson University to reproduce this thesis by photocopying or by other means, in total or in part, at the request of other institutions or individuals for the purpose of scholarly research.



The Ryerson University requires the signatures of all persons using or photocopying this thesis.

Please sign below, and give address and date.

ACKNOWLEDGMENTS

The process of writing this thesis has seen many long days and nights by the computer typing a paper longer than any other I have written to date, but the individual effort put forth by myself can not be over shadowed by the contributions of the people that made this all happen.

My most sincere thanks go out to my supervising professor Dr. A. Varvani-Farahani from the Department of Mechanical and Industrial Engineering for his timely support, endless encouragement, and valued constructive criticism throughout my Masters program in the Department of Aerospace Engineering at Ryerson University. Dr. Varvani was a brilliant supervising professor that always knew how to drive the best out of myself and my work, which undoubtedly led to the completion and success of this work.

I would also like to thank my friends; you guys have been a strong presence in my life over the course of my research, and I hope for only the best for you in your future endeavours. Thanks must also be given to Dr. Mohamad Noban at the University of Waterloo for his effort to take the time to review and critique any research I approached him with. His advice was always appreciated and considered.

The financial funding support of NSERC through Professor A. Varvani-Farahani of the Department of Mechanical Engineering at Ryerson University was greatly appreciated.

I must also give my heartfelt thanks to Tara. You believed in me when at times I doubted myself.

Lastly, I must give my deepest thanks to my family. The support and encouragement you have extended my way has been remarkable.

Chris Sutton, June 2009

ABSTRACT

Fatigue Damage Assessment of Particle-Reinforced Metal Matrix Composite Materials under Uniaxial and Multiaxial Loading Conditions, Chris Sutton, Master of Applied Science Thesis in Aerospace Engineering, Ryerson University, Toronto, Canada, 2009.

The proposed study intended to investigate the fatigue damage of Particle Metal Matrix (PMM) composites under uniaxial and multiaxial loading conditions. Five damage models of Smith-Watson-Topper (S.W.T), Ellyin, Brown-Miller, Fatemi-Socie and Varvani were tested for various PMM composite materials for their ability to correlate the uniaxial, torsional and combined tension-torsion damage-life data. Four PMM composite materials of Al 6061 / Al₂O₃ / 20p-T6, Al 6061 / Al₂O₃ / 22p-T6, Al 6061 / SiC / 17w-T6 and Ti-6Al-4V / TiC / 10p were evaluated for damage-life based on their strain-life fatigue data. The results of the fatigue damage correlation of uniaxial, torsional and combined tension-torsion fatigue damage versus life for the four PMM composites were investigated in this thesis. The critical plane approaches of Brown-Miller and Fatemi-Socie should almost have the same degree of success in damage assessment of composite materials. These strain based critical plane approaches scaled damage values versus fatigue life data as the lowest range (0.001-0.01) over low-cycle and high-cycle fatigue regimes. While energy based models of S.W.T and Ellyin holding both the stress and strain terms correlated damage data at the highest range (1-10) with a relatively larger scatter band for various fatigue lives as compared with other damage approaches. Varvani critical plane-energy approach incorporated the critical plane as the plane of crack initiation and damage growth as well as the strain energy density as a function of stress and strain components acting on the critical plane, which successfully evaluated fatigue damage values within a narrow band. Damage values based on this approach ranged between the highest (S.W.T and Ellyin) and the lowest (Brown-Miller and Fatemi-Socie) ranges and presented an intermediate range of (0.05-

0.1). Varvani damage model was further enhanced by means of material dependent terms of α and β to account for the magnitude of difference between Coffin-Manson coefficients for the metallic matrix and PMMC. Terms α and β enables to estimate fatigue damage of PMMCs if the strain-life curve for the base metal matrix is known. A finite element unit cell model was also developed to simulate stress-strain responses of Al 6061 / Al₂O₃ / 10p-T6 and Al 6061 / Al₂O₃ / 20p-T6 under monotonic tensile loading. The simulated numerical results of stress-strain showed good agreement with the experimental data and prove to be a good tool in the estimation of stress-strain behaviour of PMM composites with various volume fractions.

TABLE OF CONTENTS

| | |
|--|------|
| AUTHOR'S DECLARATION..... | ii |
| ACKNOWLEDGMENTS | iv |
| ABSTRACT..... | vi |
| TABLE OF CONTENTS..... | viii |
| LIST OF FIGURES | xii |
| LIST OF TABLES..... | xvi |
| NOMENCLATURE | xvii |
| OBJECTIVE AND SCOPE OF THE THESIS..... | xix |
| PREFACE..... | xxi |
| Chapter 1..... | 1 |
| Introduction..... | 1 |
| 1.1. Composites-Historical Review..... | 1 |
| 1.2. Metal Matrix Composites (MMCs)..... | 3 |
| 1.2.1. Discontinuous MMC production methods | 4 |
| 1.2.2. Types of MMCs..... | 4 |
| 1.3. Applications of MMCs..... | 7 |
| 1.4. Particle-Reinforced Metal Matrix Composites (PMMCs) | 8 |
| 1.4.1. Tensile Properties | 8 |
| 1.4.2. Fatigue Response of PMMCs..... | 14 |
| Chapter 2..... | 16 |
| PMMC Constitutive Equations | 16 |
| 2.1. Stress Relations | 16 |
| 2.2. Strain Relations | 20 |
| 2.3. Stress/Strain Constitutive Relations..... | 21 |
| 2.3.1. Elastic Deformation..... | 21 |
| 2.3.2. Plastic Deformation | 23 |
| 2.3.3. Elastic Strain Energy | 29 |
| Chapter 3..... | 32 |
| Finite Element Analysis of Stress-Strain Response of Al 6061 / Al ₂ O ₃ -T6 Composite..... | 32 |

| | |
|--|----|
| 3.1. Introduction | 32 |
| 3.2. ANSYS Finite Element Equations | 33 |
| 3.3. Unit Cell Model..... | 39 |
| 3.4. Results of Finite Element | 44 |
| Chapter 4 | 47 |
| Fatigue Damage Approaches | 47 |
| 4.1. Fatigue Damage Behaviour of Materials | 47 |
| 4.2. Fatigue Damage Approaches | 47 |
| 4.2.1. Smith-Watson-Topper (S.W.T) Approach | 48 |
| 4.2.2. Critical Plane Approach..... | 49 |
| 4.2.2.1. Brown-Miller Approach | 50 |
| 4.2.2.2. Fatemi-Socie Approach | 51 |
| 4.2.3. Energy Approach..... | 51 |
| 4.2.4. Critical Plane-Energy Approach..... | 57 |
| 4.3. Comparison of Damage Approaches..... | 61 |
| 4.3.1. Advantages/Disadvantages | 61 |
| Chapter 5 | 63 |
| Damage Assessment of PMMCs and Results..... | 63 |
| 5.1. General Parameters in Damage of PMMCs | 63 |
| 5.1.1. Crack Initiation and Growth..... | 63 |
| 5.1.2. The Effect of Particle Size and Volume fraction..... | 65 |
| 5.1.3. The Effect of Aging Treatment | 66 |
| 5.2. Fatigue Tests and Data | 66 |
| 5.2.1. Aluminum 6061 / Al ₂ O ₃ / 20p-T6 | 66 |
| 5.2.2. Aluminum 6061 / Al ₂ O ₃ / 22p-T6 | 69 |
| 5.2.3. Aluminum 6061 / SiC / 17w-T6..... | 71 |
| 5.2.4. Ti-6Al-4V / TiC / 10p..... | 72 |
| 5.3. Results of Fatigue Damage Assessment..... | 73 |
| 5.3.1. Smith-Watson-Topper Damage Assessment..... | 73 |
| 5.3.1.1. Al 6061 / Al ₂ O ₃ / 20p-T6..... | 75 |

| | |
|---|-----|
| 5.3.1.2. Al 6061 / Al ₂ O ₃ / 22p-T6..... | 75 |
| 5.3.1.3. Al 6061 / SiC / 17w-T6 | 77 |
| 5.3.1.4. Ti-6Al-4V / TiC / 10p..... | 77 |
| 5.3.2. Critical Plane Damage Assessment | 78 |
| 5.3.2.1. Al 6061 / Al ₂ O ₃ / 20p-T6..... | 79 |
| 5.3.2.2. Al 6061 / Al ₂ O ₃ / 22p-T6..... | 80 |
| 5.4.2.3. Al 6061 / SiC / 17w-T6 | 82 |
| 5.3.2.4. Ti-6Al-4V / TiC / 10p..... | 82 |
| 5.3.3. Ellyin's Energy Damage Assessment..... | 84 |
| 5.3.3.1. Al 6061 / Al ₂ O ₃ / 20p-T6..... | 85 |
| 5.3.3.2. Al 6061 / Al ₂ O ₃ / 22p-T6 | 85 |
| 5.3.3.3. Al 6061 / SiC / 17w-T6 | 87 |
| 5.3.3.4. Ti-6Al-4V / TiC / 10p..... | 87 |
| Chapter 6..... | 89 |
| Fatigue Model for PMMC Developed Based on Critical Plane-Energy Approach..... | 89 |
| 6.1. Strain-Life in PMMCs..... | 89 |
| 6.2. Coffin-Manson Relation for PMMCs | 89 |
| 6.3. Results of α and β for Various PMM Composites | 92 |
| 6.4. Fatigue Damage Approach..... | 93 |
| 6.5. Damage Assessment..... | 95 |
| 6.5.1. Al 6061 / Al ₂ O ₃ / 20p-T6..... | 95 |
| 6.5.2. Al 6061 / Al ₂ O ₃ / 22p-T6..... | 96 |
| 6.5.3. Al 6061 / SiC / 17w-T6 | 96 |
| 6.5.4. Ti-6Al-4V / TiC / 10p..... | 98 |
| 6.6. Life Prediction Results..... | 99 |
| Chapter 7..... | 102 |
| Discussion of Results..... | 102 |

| | |
|--|-----|
| 7.1. Stress-Strain Response using FE Analysis..... | 102 |
| 7.2. Fatigue Damage Models Assessment and their Capabilities | 103 |
| 7.2.1. Mean Stress Effect..... | 103 |
| 7.2.2. Strain Hardening Effect..... | 104 |
| 7.2.3. Continuum Mechanics Fundamentals in Models | 105 |
| 7.3. Damage Assessment of PMMC's based on Damage Models | 106 |
| 7.4. The Effect of Particle Volume Fraction | 108 |
| Chapter 8..... | 112 |
| Conclusions and Future Research Recommendations | 112 |
| 8.1. Conclusions | 112 |
| 8.2. Future Recommendations..... | 113 |
| References..... | 114 |
| Appendix A..... | 120 |

LIST OF FIGURES

| | |
|--|----|
| Figure 1.1: (A) Cross-section of continuously reinforced MMC. (B) Cross-section of a discontinuously reinforced MMC. | 3 |
| Figure 1.2: Composite material classification tree. | 4 |
| Figure 1.3: Axial Stress-Strain curve of the reinforced and un-reinforced Al-Alumina MMC | 9 |
| Figure 1.4: Shear Stress-Strain curve of the reinforced and un-reinforced Al-Alumina MMC [11] | 10 |
| Figure 5: Effect of particle volume fraction | 11 |
| Figure 1.6: Temperature effect on ultimate tensile strength [23]. | 13 |
| Figure 1.7: Stress-strain curve of MMCs with three different heat treatments [24]..... | 14 |
| Figure 2.1: stress states on a 3-dimensional cubic element. | 17 |
| Figure 2.2: Geometry of the principal directions..... | 18 |
| Figure 2.3: Stress-strain diagram undergoing plastic deformation..... | 24 |
| Figure 2.4: Other common hardening functions..... | 26 |
| Figure 2.5: Associated generated energy from elastic and plastic stress-strain curves. | 30 |
| Figure 3.1: PMM composite idealized from a 3-D hexagonal prism to a cylindrical matrix with a spherical particle located at the centre [5]. | 33 |
| Figure 3.2: Variation of the dependent field variable over a 2D domain [28]..... | 34 |
| Figure 3.3: A 3D body with displacement constraints, surface tractions, body forces, and concentrated forces. | 38 |
| Figure 3.4: Al 6061-T6 plastic strain-stress curve at room temperature. | 40 |
| Figure 3.5: Typical cross-section model of a single unit cell PMM composite. | 41 |

| | |
|--|----|
| Figure 3.6: Typical Mesh generated for the PMM composite using ANSYS Workbench 11..... | 42 |
| Figure 3.7: Typical normal strain distribution of an Al 6061-T6 PMM composite. | 44 |
| Figure 4.1: Stable hysteresis loop. | 49 |
| Figure 4.2: Elastic and plastic strain energy densities for a single uniaxial cycle [35]. | 53 |
| Figure 4.3: Master curve and coordinate system | 54 |
| Figure 4.4: log-log plot of true stress versus plastic strain. | 55 |
| Figure 4.5: (a) Strain Mohr's circle; (b) Stress Mohr's | 59 |
| Figure 4.6: Graphical representation of fatigue life-strain curve for (a) axial strain (b) shear strain | 61 |
| Figure 5.1: Test specimen geometries (a) uniaxial specimen, (b) tubular specimen used for torsional and uniaxial/torsion tests (dimensions in mm) | 68 |
| Figure 5.2: Geometry of the thin-walled tubular specimens used for multiaxial fatigue testing.. | 69 |
| Figure 5.3: Schematic diagram of the test set-up rig | 70 |
| Figure 5.4: Stress-Life data for the four PMMC materials examined in this thesis [46,56,57,58]. | 74 |
| Figure 5.5: S.W.T. damage assessment methodological flowchart. | 75 |
| Figure 5.6: The S.W.T. damage parameter versus fatigue lives for Al 6061 / Al ₂ O ₃ / 20p-T6.... | 76 |
| Figure 5.7: S.W.T. damage parameter versus fatigue lives for Al 6061 / Al ₂ O ₃ / 22p-T6. | 76 |
| Figure 5.8: S.W.T. damage parameter versus fatigue lives for Al 6061 / SiC / 17w-T6..... | 77 |
| Figure 5.9: S.W.T. damage parameter versus fatigue lives for Ti-6Al-4V / TiC / 10p. | 78 |
| Figure 5.10: (a) Brown-Miller and (b) Fatemi-Socie's damage assessment methodological flowcharts..... | 79 |

| | |
|--|----|
| Figure 5.11: Brown-Miller damage parameter versus fatigue lives for Al 6061 / Al ₂ O ₃ / 20p-T6. | 80 |
| Figure 5.12: Fatemi-Socie damage parameter versus fatigue lives for Al 6061 / Al ₂ O ₃ / 20p-T6. | 80 |
| Figure 5.13: Brown-Miller damage parameter versus fatigue lives for Al 6061 / Al ₂ O ₃ / 22p-T6. | 81 |
| Figure 5.14: Fatemi-Socie damage parameter versus fatigue lives for Al 6061 / Al ₂ O ₃ / 22p-T6. | 81 |
| Figure 5.15: Brown-Miller damage parameter versus fatigue lives for Al 6061 / SiC / 17w-T6. | 82 |
| Figure 5.16: Fatemi-Socie damage parameter versus fatigue lives for Al 6061 / SiC / 17w-T6.. | 83 |
| Figure 5.17: Brown-Miller damage parameter versus fatigue lives for Ti-6Al-4V / TiC / 10p... | 83 |
| Figure 5.18: Fatemi-Socie damage parameter versus fatigue lives for Ti-6Al-4V / TiC / 10p.... | 84 |
| Figure 5.19: Ellyin's Energy damage assessments methodological flowchart..... | 85 |
| Figure 5.20: Ellyin energy damage parameter versus fatigue lives for Al 6061 / Al ₂ O ₃ / 20p-T6. | 86 |
| Figure 5.21: Ellyin energy damage parameter versus fatigue lives for Al 6061 / Al ₂ O ₃ / 22p-T6. | 86 |
| Figure 5.22: Ellyin energy damage parameter versus fatigue lives for Al 6061 / SiC / 17w-T6 Energy..... | 87 |
| Figure 5.23: Ellyin energy damage parameter versus fatigue lives for Ti-6Al-4V / TiC / 10p.... | 88 |
| Figure 6.1: Comparison of Strain-Fatigue Life of Al 6061 and Al 6061 / Al ₂ O ₃ / 20p [62]...... | 90 |
| Figure 6.2: Schematic strain-life diagram of metal matrix and PMM composite. | 91 |

| | |
|---|-----|
| Figure 6.3: (a) $\epsilon f'$ coefficients used to determine α ratios (b) (σ'_f/E) coefficients used to determine β ratios..... | 93 |
| Figure 6.4: Varvani Critical Plane-Energy damage assessment methodological flowchart..... | 95 |
| Figure 6.5: Varvani damage parameter versus fatigue lives for Al 6061 / Al ₂ O ₃ / 20p-T6..... | 96 |
| Figure 6.6: Varvani damage parameter versus fatigue lives for Al 6061 / Al ₂ O ₃ / 22p-T6..... | 97 |
| Figure 6.7: Varvani damage parameter versus fatigue lives for Al 6061 / SiC / 17w-T6. | 97 |
| Figure 6.8: Varvani damage parameter versus fatigue lives for Ti-6Al-4V / TiC / 10p..... | 98 |
| Figure 6.9: Predicted fatigue lives versus experimental fatigue lives for three different PMM composites tested under various loading conditions..... | 101 |
| Figure 7.1: Fatigue damage models versus fatigue lives for Al 6061 / Al ₂ O ₃ / 10P-T6, Al 6061 / Al ₂ O ₃ / 20P-T6, and Al 6061 / SiC / 17W-T6 composites tested under various uniaxial and multiaxial loading conditions..... | 107 |
| Figure 7.2: Effect of particle volume fraction for Al 6061/ Al ₂ O ₃ composites tested under uniaxial loading conditions. | 109 |
| Figure 7.3: Effect of particle volume fraction for Al 6061/ Al ₂ O ₃ composites tested under torsional loading condition. | 109 |

LIST OF TABLES

| | |
|---|-----|
| Table 1.1: Mechanical properties of various MMC materials | 9 |
| Table 3.1: Meshing properties for both PMM composites. | 43 |
| Table 5.1: Uniaxial mechanical properties of Al 6061 / Al ₂ O ₃ / 20p-T6 and its constituents..... | 67 |
| Table 5.2: Mechanical properties of Al 6061 PMMC and the base alloy [10,45]..... | 71 |
| Table 6.1: Comparison of calculated damage values V (Eqn (6.5)) based on experimental fatigue data with fatigue damage data predicted using terms α and β and equation (6.6). | 100 |
| Table 7.1: Slopes of D-N curves for Al 6061/ Al ₂ O ₃ with Vf = 20% and Vf = 22% tested under uniaxial loading condition..... | 110 |
| Table 7.2: Slopes of D-N curves for Al 6061/ Al ₂ O ₃ with Vf = 20% and Vf = 22% tested under torsional loading conditions..... | 111 |

NOMENCLATURE

| | |
|--|---|
| $\Delta(\gamma_{ap}/2), \Delta\varepsilon_{ap}$ | The shear and axial strain ranges respectively |
| $\Delta(\gamma_{max}/2), \Delta\varepsilon_n$ | Maximum shear strain range and normal strain range acting on the critical plane, respectively |
| $\Delta\varepsilon_a, \Delta\sigma_a, \Delta\varepsilon_n$ | Applied tensorial strain range, stress range, and shear stress range, respectively |
| $\Delta\varepsilon_{ij}, \Delta\sigma_{ij}$ | The strain and stress tensor ranges (where i and $j=1, 2, 3$) |
| $\Delta\tau_{max}, \Delta\sigma_n$ | Maximum shear stress range and normal stress range, respectively |
| E | The elastic modulus |
| $\varepsilon_1, \varepsilon_2, \varepsilon_3$ | Principal strains ($\varepsilon_1 > \varepsilon_2 > \varepsilon_3$) |
| $\varepsilon_e, \varepsilon_p$ | Elastic strain and plastic strain respectively |
| ν_e, ν_p, ν_{eff} | Elastic, plastic, and effective Poisson's ratios respectively |
| θ_1, θ_2 | Angles during loading and unloading parts of a cycle respectively at which the Mohr's circles are the largest |
| $\sigma_1, \sigma_2, \sigma_3$ | Principal stresses ($\sigma_1 > \sigma_2 > \sigma_3$) |
| $\sigma'_f, \varepsilon'_f$ | The axial fatigue strength coefficient and axial fatigue ductility coefficient, respectively |
| τ'_f, γ'_f | The shear fatigue strength coefficient and shear fatigue ductility coefficient, respectively |
| K', n' | Ramberg-Osgood coefficient and exponent, respectively |
| G | Shear modulus |
| N_f | Life cycles |
| $W_{ten}^e, W_{ten}^p, W_{ten}$ | Tensile elastic, plastic and total strain energies |
| $W_{shear}^e, W_{shear}^p, W_{shear}$ | Shear elastic, plastic and total strain energies |
| W | Total strain energy |
| ρ | Density |
| σ_y, σ_u | Yield and ultimate strengths, respectively |

| | |
|------------------------|---|
| V_f | Volume fraction of reinforcement |
| r, R, H | radius of spherical particle, radius of cylindrical metal matrix and height of metal matrix |
| S, K | Damage model constants for Brown-Miller and Fatemi-Socie models, respectively |
| λ | Bi-axial strain ratio |
| $(V_c)_{\text{pred.}}$ | Predicted Varvani damage parameter for a PMM composite |
| $(V_c)_{\text{exp.}}$ | Experimental Varvani damage parameter for a PMM composite |
| α, β | Modified critical plane-energy material constants |

OBJECTIVE AND SCOPE OF THE THESIS

Particle Metal Matrix composites (PMMCs) have been extensively investigated since 1980 for applications where light weight structures with high strength and fatigue resistance were required. Currently very little published fatigue data are available in the literature and studies that examine the capabilities of earlier developed fatigue damage models for discontinuous particle metal matrix composites. A crucial objective of the current thesis is to examine the fatigue damage response of PMM composites and discuss the capability of damage models incorporating phenomenological parameters of reinforced particle volume fraction, mean stress effect, strain hardening and material properties of the base metallic matrix and reinforced particles in PMMCs.

The fatigue damage assessment of the discontinuous PMM composites investigated in this study were evaluated based on the Smith-Watson-Topper (S.W.T), Ellyin, Brown-Miller, Fatemi-Socie and Varvani damage approaches. Fatigue stress-life data of various uniaxial and multiaxial loading for PMM composites of Al 6061 / Al₂O₃ / 20p-T6, Al 6061 / Al₂O₃ / 22p-T6, Al 6061 / SiC / 17w-T6 and Ti-6Al-4V / TiC / 10p were extracted from literature to evaluate fatigue damage models and to further enhance a damage model taking into account the related phenomenological parameters.

Considering material dependent parameters of α and β in Varvani damage, the model enabled damage assessment of PMM composite materials. This makes a direct damage assessment of PMMCs by having strain-life Coffin-Manson coefficients for the metallic matrix.

To better understand the effect of volume fraction with a PMM composite, a finite element unit cell models was generated with Solidworks 2005 and evaluated using Ansys Workbench 11 for the stress-strain behaviour response of Al 6061 / Al₂O₃ composites under monotonic tensile loading. The results obtained from numerical simulation help to approximate the tensile stress-strain behaviour of these composites for various particle fractions.

PREFACE

The following provides a brief description of material covered in the chapters of this thesis.

Chapter 1 reveals the history of composites and the origins of modern day metal matrix composites. Particle-reinforced metal matrix composites are introduced along with their tensile and fatigue behaviour.

Chapter 2 presents the PMM composite constitutive equations of stress, strain and the stress-strain relations of elastic, plastic and strain energy.

Chapter 3 simulates the stress-strain response of PMM composites using a unit cell finite element model. Simulated stress-strain response under monotonic loading is compared with experimental data of the same material reported in literature.

Chapter 4 presents fatigue damage models of Smith-Watson-Topper, Ellyin, Brown-Miller, Fatemi-Socie and Varvani and discusses their terms and capabilities in assessing fatigue damage under various loading conditions. S.W.T and Ellyin are energy based approaches while Brown-Miller and Fatemi-Socie are strain-based critical plane approaches. Varvani's damage model incorporates the critical plane of crack and energy resulting from stress and strain components acting on the critical plane.

Chapter 5 discusses the parameters of damage assessment for PMM composites, which include crack initiation and growth, and the effects of particle size, volume fraction and heat treatment. Results of damage assessment based on S.W.T, Ellyin, Brown-Miller, and Fatemi-Socie approaches for various PMM composite materials tested under various loading conditions are presented.

Chapter 6 incorporates material dependent parameters of α and β in Varvani critical plane-energy approach to account for the effects of shear and normal fatigue properties in the damage model. Results for the damage assessment of the modified Varvani model with the various PMM composites are included.

Chapter 7 compares and discusses the capabilities of the fatigue damage models with Varvani's approach for various PMM composites tested under uniaxial and multiaxial loading conditions. Results of stress-strain simulated using an FE unit cell model are compared with experimentally obtained values of stress-strain data for Al 6061 / Al₂O₃. The effect of particle volume fraction on fatigue damage of Al 6061 / Al₂O₃ / 20p-T6 and Al 6061 / Al₂O₃ / 22p-T6 under uniaxial and torsional fatigue loading is discussed. These damage-life curves are evaluated based on damage approaches discussed in this thesis.

Chapter 8 summarizes the conclusions achieved from this study. This chapter brings attention to the applicability of various fatigue damage models in assessing damage for PMM composites under various loading conditions and recommends some research investigation on fatigue of PMMCs as a future outlook.

Appendix A at the end of this thesis lists composite material data including material properties, fatigue S-N data tested under various loading conditions, and results of damage analysis based on various damage models.

Chapter 1

Introduction

1.1. Composites-Historical Review

Man has always been intrigued with the ability to innovate something better, and the area of material engineering is a perfect example of man's ability to manipulate naturally occurring materials to desired specifications. Engineering materials can date back to the time of the Egyptians, Mayans, and Incans. During this time evidence has shown that standard clay was mixed with plant fibres or straw to make bricks and other pottery stronger. The modern history of composite materials began in 1930 with the development of fibreglass. The fibreglass was actually developed by accident while an engineer became interested in a type of fibre that was forming while he was applying lettering to a glass bottle. This new finely drawn glass was initially produced as insulations with structural applications soon to follow. The development of composite materials for both structural and semi-structural parts was accelerated during WWII because of the increase in aircraft production, and also in the area of tooling. One of the first major production parts of composite materials on aircraft were the air supply ducts. Since the ducts were the last system to be installed, they frequently had to bend and twist around other fixed systems. Since metal ducts were difficult to engineer into these variable shapes, fibre-resin composites seemed to be the logical choice [1]. As WWII accelerated the applications of fibre-resin composites, the end of the war saw the adaption of composite materials into many more commercial applications. Boat hauls in the late 1940's had been engineered with fibreglass materials, and in 1953 Chevrolet manufactured the first ever all fibreglass body car; the Corvette.

As time continued to march forward, more and more commercial applications involving composite materials were being produced as the manufacturing methods of these composites were being refined to reduce costs. The 1960's and 1970's brought forth a significant leap in composite materials with the development of carbon fibres, boron filaments, and aramid fibres (Kevlar®). These new fibre reinforcements provided a much higher strength than previous glass fibres.

The development of Metal Matrix Composites (MMCs) in the 1970s emerged in response to the need for new materials to fulfill the capabilities of advanced designs within the military sector [2]. This initial phase of MMC research and design at this time in history provided an improved affordability of the technology as well as a large amount of engineering data and results of the capabilities of these new materials. By the late 1970s, demand for affordability and safety of research with MMC materials started to slow production of MMC materials, even within the military sector. These heightened expectations of MMCs made it difficult for producers to certify these materials for different applications [3]. Also during this time, advanced military projects were decreasing as countries were switching from active military projects to a more conservative strategy of extending the life to existing systems. This stance to conserve military spending on new projects made the development of high performance materials such as MMCs very difficult to move forward.

The 1980s saw a rejuvenation of MMC research and design. The reason for this revitalization was mainly due to the development of discontinuously reinforced MMCs. Even though discontinuously reinforced MMCs provided inferior mechanical properties to continuously reinforced MMCs, what they provided to industry was an improved affordability and ease of processing. These two main improvements made it possible for MMCs to find a place in the

commercial markets. The main efforts of research and design for discontinuously reinforced MMCs focused on the right balance between performance, cost, and risk acceptability.

1.2. Metal Matrix Composites (MMCs)

There has been plenty of research that shows that the inclusion of ceramic particles or whiskers, whether continuously or discontinuously (see figure 1.1) in a metallic matrix leads to improved properties of stiffness, strength, wear, and creep resistance. The reasoning behind MMCs is that they take the best characteristics of two materials and combine them to make a superior product. The combination of the ductile and tough matrix alloy combined with the high strength and modulus of the reinforcement provides properties that can not be matched by any unreinforced alloy.

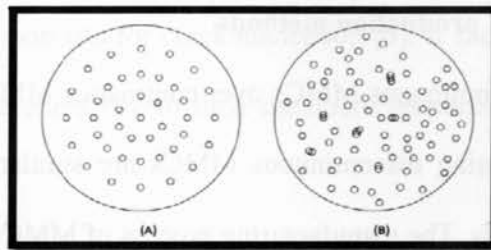


Figure 1.1: (A) Cross-section of continuously reinforced MMC. (B) Cross-section of a discontinuously reinforced MMC.

The behaviour of discontinuously reinforced MMCs can be assumed isotropic because of the random orientation of the fibres or particles as well as the lower aspect ratio of the reinforcements. However, the same can not be said about continuously reinforced MMC. Due to the extent of information regarding both continuously and discontinuously reinforced MMCs, this thesis will only focus on discontinuously reinforced MMCs from this point forward.

Figure 1.2 outlines the classification of composite materials as a tree diagram. Notice the dark bold line showing the class of composite materials that is under evaluation in this paper.

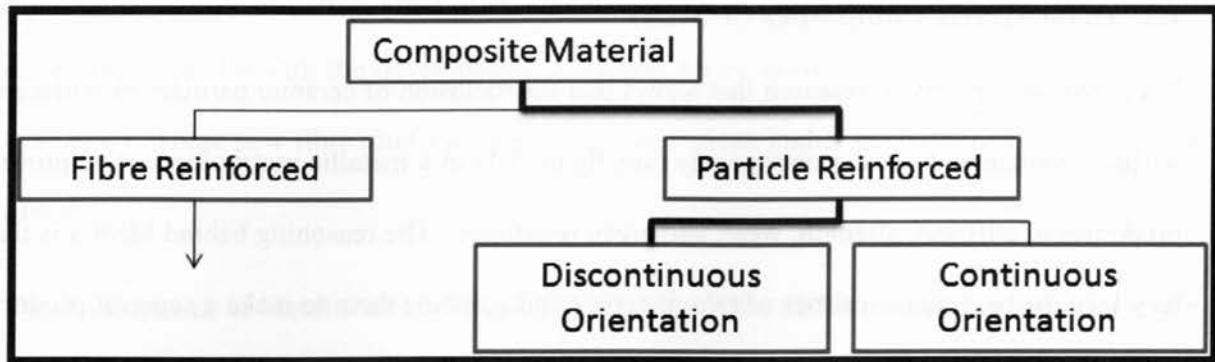


Figure 1.2: Composite material classification tree.

1.2.1. Discontinuous MMC production methods

The main advantage of discontinuous MMCs over continuous MMCs is the ease of processing. Modern methods of processing discontinuous MMCs are similar to the techniques used for unreinforced matrix materials. The manufacturing process of MMCs essentially takes the molten metal matrix and mixes in the reinforcements through stir and squeeze casting, spray co-deposition, or through solid-state consolidation using powder metallurgy techniques. The process of casting usually requires a secondary process of either extrusion, forging, or rolling to break apart any reinforcements, distribute the reinforcement throughout the matrix, eliminate any porosity, and in effect, improve the bonding between the reinforcement and the matrix [4,5].

1.2.2. Types of MMCs

The choice of the matrix material strongly depends on the strength, temperature, density, and cost of the intended application of the MMC. For most high strength and moderate temperature

applications, titanium alloys seem to be the obvious candidate as the matrix material. There are however many applications where aluminum alloys can compete with titanium alloys as the matrix material, even though the strength and temperature capabilities of aluminum are less than that of titanium. The advantage of aluminum alloys as the matrix material is the cost and availability compared to that of titanium. Aside from the main factors of strength, thermal efficiency, and cost, the matrix material is also considered based on other factors such as ductility, fracture toughness, and fatigue resistance. The interaction between the matrix material and the reinforcement is also crucial as to avoid any undesirable chemical reaction at the interface between the two materials. Possible reactions between the two materials in the MMC may lead to the formulation of intermetallic compounds at the interface which would lead to detrimental effects in transferring the load from the matrix to the reinforcement. The harmful reaction may also be a common site for crack nucleation [6]. It should be noted that pure metals are not desirable matrix materials due to their mediocre properties when compared with their alloy counterparts.

There are three main classes of aluminum alloys that have been selected in the past and used in the present as matrix materials for MMCs. The first class of aluminum alloys are the wrought commercial alloys of 6061, 2124, 2024, and 7075. The second being the lighter aluminum-lithium alloys of 8090, and the last being the high-temperature alloys of aluminum-iron and aluminum-scandium. For the most part the development of new matrix materials that would be better suited for MMC applications has been overshadowed by modifying pre-existing aluminum alloy materials. The first classes of aluminum alloys mentioned above are all chosen as suitors for MMCs because they offer adequate mechanical properties and more importantly they are readily available commercially. These aluminum alloys have been well established and studied

over the years, and articles such as [7,8] have outlined their acceptance as MMC matrix materials. The same can not be said about the second category of aluminum alloys. There is considerable interest in aluminum-lithium alloys in terms of reducing the overall density of the MMC as well as improving the modulus, but to date there has been little research that approves the potential of this alloy for MMC applications. There are several forms of reinforcement that are used in producing discontinuously reinforced aluminum (DRA) MMCs. Of the many reinforcements that can be used with aluminum alloy matrices, SiC is the one reinforcement that requires the alloy matrix to have approximately 8-9 weight percentage of silicon in it. The inclusion of Si in the aluminum alloy reduces the dislocation of SiC in the MMC and avoids any adverse reaction with the reinforcement. Any aluminum alloy with insufficient silicon content can not be used in conjunction with SiC, but can be used with such reinforcements of Al₂O₃ (Alumina), TiB₂ (Titanium Boride), TiC (Titanium Carbide) and B₄C (Boron Carbide). If the aluminum alloy matrix contains any magnesium, then it will react with Al₂O₃ reinforcements forming MgAl₂O₃. This reaction is not hazardous to the properties of the MMC; however any reinforcements that react with the matrix alloy should be avoided all together.

Titanium alloys as matrix materials are the preferable choices when compared to aluminum alloys when cost is not a concern. Titanium alloys offer a higher strength and temperature capability than aluminum alloys and therefore one would assume plenty of research and development in this area of MMCs, however, until recently titanium alloys as a matrix material with discontinuous particle reinforcement has seen very little progress. The common titanium alloy of Ti-6Al-4V (alpha-beta alloy) is the main focus of matrix material in MMC applications under investigation today. Most modern day titanium alloy MMCs are reinforced with TiB₂ or TiC particles since SiC particles create an unfavourable reaction with the titanium matrix [6].

1.3. Applications of MMCs

MMCs have found a common place in the aerospace industry, where the need for high performance materials drove the research and development of MMCs and today the cost of production of these materials has dropped to allow for further applications in other commercial markets. The aerospace industries requirement for high performance materials saw the development of MMCs with tailored properties of low density, high strength and stiffness, and thermal expansion and conductivity. These materials were very costly to produce which is why large aerospace budgets accommodated the research and development of MMCs. For the most part, many MMCs used in aerospace applications are of the continuous reinforced type. Continuously reinforced MMCs offer superior performance over discontinuously reinforced composites, which is why the Hubble Telescope used pitch-based continuously reinforced carbon fibre with aluminum as the wave-guide booms since this material provided high strength and stiffness, while reducing the weight and lowering the coefficient of thermal expansion. The automotive industry has also capitalized on the use of MMCs with the application of replacing diesel piston crowns made originally of nickel cast iron with short alumina fibres in an aluminum alloy matrix. This replacement of materials allowed for the production of lighter, more abrasion resistant, and cheaper components. The Honda Motor Company has also found a use for MMCs as engine cylinder liners in the Prelude model of motor vehicles. These liners were composed of carbon and alumina fibres reinforced in an aluminum alloy matrix. The automotive industry has also seen a potential application of MMCs in the design of drive-shafts. The critical speed of a drive shaft is dependent on the diameter and its length of the component, as well as the material parameter of specific stiffness (E/ρ). As the drive shaft gets longer and the shaft diameter decreases, the critical speed of the shaft reduces. One can increase the critical speed of the drive

shaft by increasing the specific stiffness. The use of MMCs as materials for drive-shaft design would allow for higher values of specific stiffness while allowing for shaft components to be produced with smaller diameters and longer length [3].

1.4. Particle-Reinforced Metal Matrix Composites (PMMCs)

1.4.1. Tensile Properties

Discontinuous particle reinforced metal matrix composites have started to mature as one of the most widely known MMC class of materials because of their advanced mechanical properties of strength, stiffness, wear, and corrosion resistance. Of all the reinforcements used in MMC production, SiC particles reinforced in an aluminum alloy matrix are among the most common commercially available MMCs. The tensile properties of this form of MMC has been studied and researched, where it has been determined that multiaxial surface tension in the MMC decreases the ductility of the matrix material [9]. Table 1.1 shows three different Al 2124 matrices reinforced with both alumina and SiC. The mechanical properties of the various Al 2124 MMCs reveal that there is little increase in weight with an increase in strength; however the added stiffness of the ceramic particles reinforcing the matrix decreases the fracture toughness of the material.

Table 1.1: Mechanical properties of various MMC materials [10].

| Material | ρ [kg/m ³] | σ_y [Mpa] | σ_u [Mpa] | ν | K [Mpa · m ^{1/2}] |
|---|-----------------------------|------------------|------------------|-------|-----------------------------|
| Al 2124 - 10% Al ₂ O ₃ p | 2900 | 450 | 490 | 0.31 | 17.5 |
| Al 2124 - 20% SiCp | 2850 | 405 | 590 | 0.325 | 18 |
| Al 2124 - 15% SiCw | 2830 | 475 | 585 | 0.3 | 18 |
| Al 2124 | 2760 | 440 | 480 | 0.33 | 30 |

Research by Owolabi [11] has shown through static tensile and torsional monotonic loading of Al 6061-T6 reinforced with various volume fractions (V_f) of alumina particles that the stress-strain curve of the unreinforced alloy falls below that of the MMC. Figures 1.3 and 1.4 below outline the stress-strain curve of the Al-alumina MMC under both tension and torsion loading.

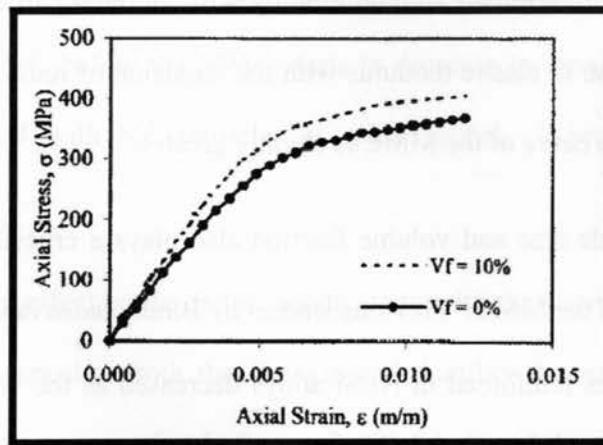


Figure 1.3: Axial Stress-Strain curve of the reinforced and un-reinforced Al-Alumina MMC [11].

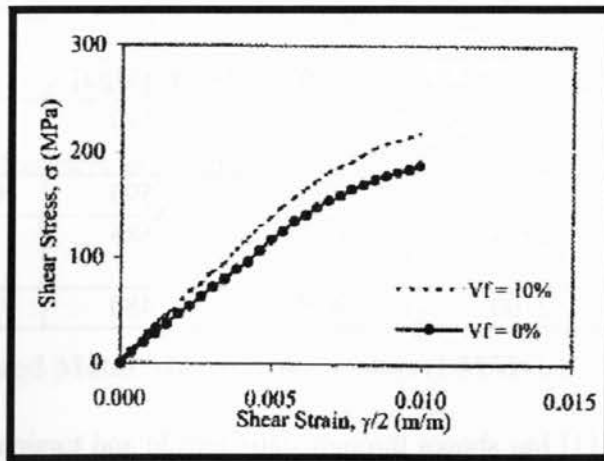


Figure 1.4: Shear Stress-Strain curve of the reinforced and un-reinforced Al-Alumina MMC [11].

Both figures 1.3 and 1.4 reveal a similar elastic-plastic transition between the un-reinforced aluminum alloy and the reinforced aluminum alloy with alumina particles. Both these figures also confirm the increase in elastic modulus with the inclusion of reinforcing particles since the slope of the stress-strain curve of the MMC is slightly greater.

The effect of the particle size and volume fraction also plays a crucial role in the mechanical stress-strain response of the MMC. Previous studies by Bindumadhavan [12] recognized that the ductility of SiC particles reinforced in Al-Si alloys decreased as the volume fraction (V_f) was increased. So it was advantageous to produce composites with SiC particles with low volume fraction for ease of processing and machining. It was also found that wear resistance of the composite is reduced as the particle size of the reinforcement is reduced. As well, the tensile strength properties of the MMCs tend to increase with the increase in particle size [13], while the fracture toughness of the composite improves with particle size increase [14]. Figure 1.5 below outlines the effect of volume fraction of SiC particles reinforced in Al 2024 on the ultimate and yield strength.

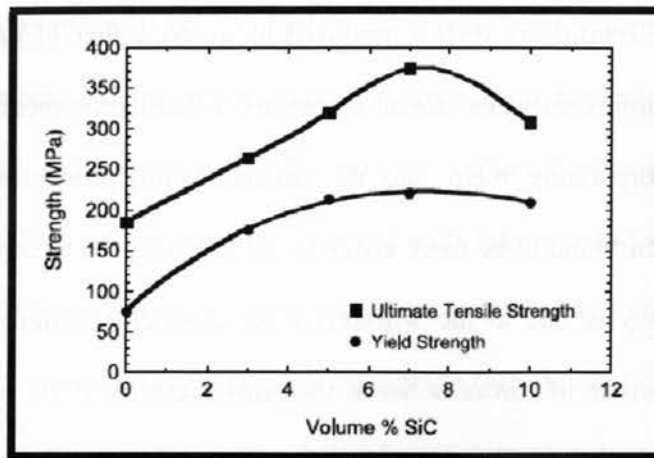


Figure 5: Effect of particle volume fraction (V_f) on strength of Al 2024 reinforced with SiC [12].

The effect of volume percentage is shown to have a significant effect on the tensile properties of the composites; however, for the Al 2024 matrix reinforced with SiC, there is a limit to the volume percentage of SiC before the MMC starts to decrease in terms of its tensile properties. This limit for Al 2024 with SiC particles is approximately 7 percent volume fraction of reinforcement.

Particle size also has an effect on the failure mode along with the previously mentioned strength and ductility of the composite. Both the strength and ductility decrease as the particle size is increased. The failure process for both small ($<6.5\mu\text{m}$) and large ($>23\mu\text{m}$) particles are distinctively different. For small particles, failure has shown to occur in the matrix material with very few fractured or broken reinforcements. However, the opposite is true for large particle reinforcement, where failure in this case occurs by particle breakage. The optimal choice of particle size reinforcement is in between these two size ranges, where neither mode of failure dominates the other [15].

Most discontinuously reinforced MMCs produced today are either of the form of particles or whiskers. Particle reinforcement has found a common place in commercial MMC markets due to their ease in incorporating them into the matrix during production. However, whisker reinforcement has been found to be more efficient in increasing the strength and modulus of the MMCs. This efficiency is due to the whiskers more distinctive length/diameter ratio, which allows for greater transfer of forces between the reinforcement to the matrix when compared with particles. Whiskers just like particles maintain random reinforcement geometry when produced. This allows for good strength characteristics in all directions of the material [1].

The strain rate imposed on an MMC is another factor that affects the stress-strain behaviour of the composite during loading. Research conducted by H. Zhang et. al. [16] on Al 6092 with 15 percent boron carbide revealed that variations in low strain rates have an effect on the stress-strain behaviour of the material. For strain rates $<1s^{-1}$, the strength of the material decreases with increasing strain. This behaviour is characteristically associated with dynamic strain aging, which is caused by the presence of fast diffusing solute atoms interacting with moving dislocations [17]. Other research by Yadav et. al. [18] showed that the effect of strain rate in particulate reinforced MMCs is strongly dependent on the particle volume fraction. It was then later found that the effect of strain rate is coupled with the volume fraction of the particulate along with the strain hardening of the composite [19].

It has been established that MMCs have superior room temperature mechanical properties, but also show stronger, more creep resistant, and more wear resistant at elevated temperature than their corresponding unreinforced alloys [20]. However, MMCs do have drawbacks since at elevated temperatures they have limited ductility and crack growth resistance [21]. One study [22] observed that aluminum alloy reinforced with alumina showed that favoured void nucleation

sites typically at the interface of the reinforcement and the matrix normal to the applied load, changed to those exhibiting sharp corners in the direction of the loading axis as the temperature increased. Onoro et. al. [23] studied the high temperature effects on the mechanical properties of aluminum 6061 and 7015 as the matrix reinforced with boron carbide particles [23]. It was found that the Al 7015 alloy with 5 wt. % reinforced particles was stronger than that of the unreinforced Al 7015 until about 500 degrees centigrade (see figure 1.6). This is very similar with that of the Al 6061 alloy as the matrix; however the strength values are lower than those of the Al 7015.

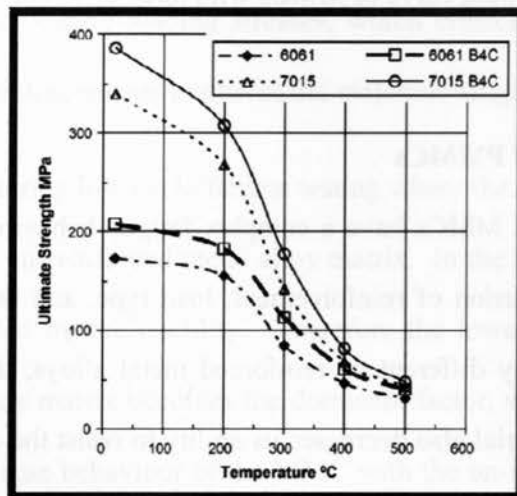


Figure 1.6: Temperature effect on ultimate tensile strength [23].

Heat treatments of the MMCs have also been shown to change the mechanical response of the material during monotonic loading. Xia et al. [24] has shown that the MMC material with the T6 heat treatment has the highest stiffness and strength, with its stress-strain curve becoming flat when the strain exceeds one percent. Also, there was no clear linear response observed for the material with the T0 heat treatment (see figure 1.7).

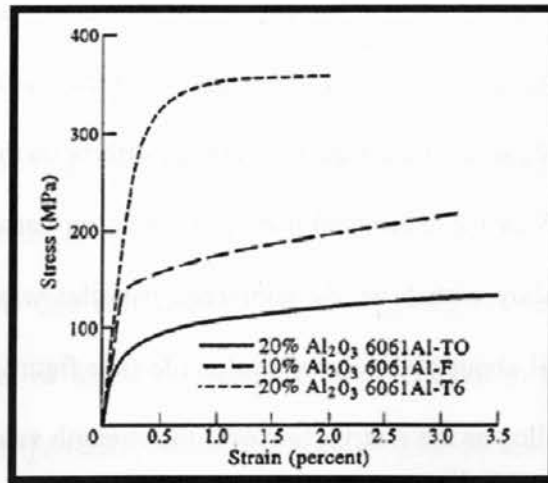


Figure 1.7: Stress-strain curve of MMCs with three different heat treatments [24].

1.4.2. Fatigue Response of PMMCs

Discontinuously reinforced MMCs have a complex fatigue behaviour that can be improved or even degraded by the inclusion of reinforcement, load type, and the type of fatigue test. For MMCs, as well as in many different un-reinforced metal alloys, the factors that improve the crack initiation of the material also decreases its ability to resist the crack growth once initiated. A common example of this behaviour is the influence of reinforcement on the fatigue performance of aluminum alloys. With under-aged aluminum alloys, the inclusion of reinforcement leads to improvements in fatigue behaviour during stress controlled tests, but causes an increase in fatigue crack propagation rates. However, over-aged aluminum alloys with reinforcements generates both an improvement with the fatigue behaviour and the resistance to fatigue crack propagation. Stress controlled testing also determined that for high cycle fatigue conditions, high volume fractions of fine reinforcement particles are preferred to increase the

fatigue crack initiation resistance. For an improvement in the fatigue crack growth resistance, a higher volume fraction of coarser particles is favoured [25].

The fatigue life of discontinuously reinforced MMCs under high cycle stress-life testing has generally shown to be higher or better than that of the un-reinforced metal alloy. The reason for this type of behaviour can be explained by the influence of reinforcement on the materials modulus and work hardening. Since the reinforcements are generally much stronger and stiffer than that of the matrix metal alloy, they in turn cause the MMC to increase in work hardening rate and a reduce in modulus under both monotonic loading and cyclic loading conditions. Therefore during low to moderate loading stresses, which creates high cycle fatigue lives of MMCs, the inclusion of reinforcements improves the materials fatigue characteristics [25].

The opposite can be said during low cycle fatigue testing where the fatigue strength of the MMC converges with that of the un-reinforced metal alloy matrix. In the low cycle regime, the fatigue of the material is controlled by the ductility. Therefore the lower tensile strength and cyclic ductility's of the metal alloy matrix becomes the dominant factor, which explains the reason for the convergence of the fatigue behaviour of the MMC with the un-reinforced metal matrix alloy [25]. During strain-life testing, the opposite fatigue behaviour is observed when compared with stress-life testing. The discontinuously reinforced MMC has clearly shown to have lower fatigue strength when evaluated against the un-reinforced metal matrix alloy. During strain controlled tests, the elastic strain is lower in the MMC than in the un-reinforced alloy at the same stress level. Since the MMC has a higher modulus than the un-reinforced alloy, the same strain in both will result in an increase in plastic strain in the MMC thereby accelerating the fatigue damage in the composite [25]

Chapter 2

PMMC Constitutive Equations

2.1. Stress Relations

The deformation/strain of a specimen is the response of the material body to an applied force or stress. To understand the stress and strain behaviour of a material, relations that allow the strain to be calculated straight from the stress and vice versa are essential, which are called constitutive relations. There are an unlimited number of constitutive parameters/constants which relate a particular response to a specific perturbation of a continuum system. A constitutive parameter and a constitutive equation both predict a response usually under a set of strict limits. In order to understand the consequences from a given constitutive parameter a model for the mechanical behaviour must be considered based on the understanding of both structure and morphology for a given material.

The general state of stress follows that a positive stress vector acts normal to a positive cubic face and points to a positive coordinate direction.

In a homogeneous material, for each of the three surfaces on a cubic element shown in figure 2.1, there are a total of 3 stress components of a normal and two shear stresses. This makes a 9 component second order stress tensor. In basic Cartesian coordinates, the second order tensor, σ_{ij} , is given by:

$$\sigma_{ij} = \begin{bmatrix} \sigma_{xx} & \sigma_{xy} & \sigma_{xz} \\ \sigma_{yx} & \sigma_{yy} & \sigma_{yz} \\ \sigma_{zx} & \sigma_{zy} & \sigma_{zz} \end{bmatrix} \quad (2.1)$$

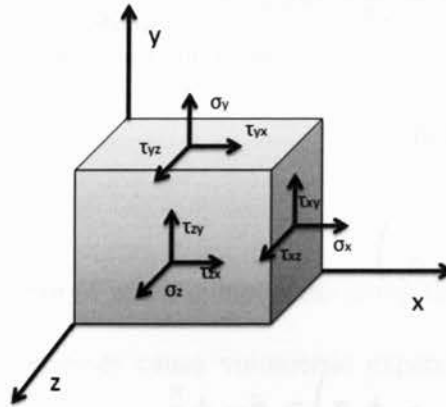


Figure 2.1: stress states on a 3-dimensional cubic element.

The general stress state has been shown to have nine components, in which three are normal stresses and six are shear stresses. In a homogeneous material, these nine components are reduced to 6 where $\tau_{xy} = \tau_{yx}$, $\tau_{xz} = \tau_{zx}$ and $\tau_{yz} = \tau_{zy}$.

The stress on a body is a function of the angle of rotation, where there occurs a specific angle in which the normal stresses are either maximum or minimum. These maximum and minimum stresses are called principal stresses. When principal stresses are achieved, the corresponding shear stresses on the element are all equal to zero. Since there are three principal directions in the three-dimensional stress state, there are always three principal stresses ordered as $\sigma_1 > \sigma_2 > \sigma_3$. To calculate the principal stresses one would have to determine the angular direction of θ in which the derivative of the function $\sigma = f(\theta)$ set equal to zero is a maximum or a minimum. Solving for these principal stresses:

$$\frac{d\sigma}{d\theta} = 0 = (\sigma_x - \sigma_y) \cdot \sin 2\theta + \cos 2\theta$$

$$\rightarrow \frac{\sin 2\theta}{\cos 2\theta} = \tan 2\theta = \frac{2\tau_{xy}}{(\sigma_x - \sigma_y)} \quad (2.2)$$

Solving equation (2.2) results in,

$$\theta_{N1} = 0.5 \cdot \tan^{-1} \left(\frac{2\tau_{xy}}{\sigma_x - \sigma_y} \right) \quad (2.3)$$

$$\theta_{N2} = 0.5 \cdot \tan^{-1} \left(\frac{2\tau_{xy}}{\sigma_x - \sigma_y} + \pi \right) = \theta_{N1} + \frac{\pi}{2} \quad (2.4)$$

The geometric representation of the principal directions found above in equations (2.3) and (2.4) are shown below in figure 2.2.

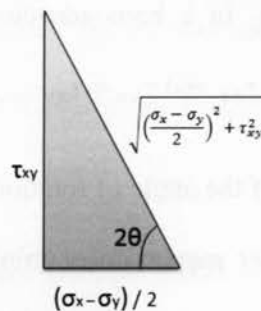


Figure 2.2: Geometry of the principal directions.

Using trigonometric identity relations, the plane stress case can be solved to find the maximum and minimum values of principal stress as:

$$\sigma_{\theta} = \sigma_{1,2} = \frac{\sigma_x + \sigma_y}{2} \pm \sqrt{\left(\frac{\sigma_x - \sigma_y}{2}\right)^2 + \tau_{xy}^2} \quad (2.5)$$

For the plane stress case, in the x-y plane, the stress of σ_z is equal to zero. Therefore the values of σ_1 and σ_2 are not always necessarily the first two principal stresses until they are compared with $\sigma_z = 0$. Performing further trigonometric substitution similar to how equation 2.5 was derived gives the planes stress case of maximum shear stress as:

$$\tau_{max} = \sqrt{\left(\frac{\sigma_x - \sigma_y}{2}\right)^2 + \tau_{xy}^2} \quad (2.6)$$

Recalling equation (2.1), the mean of stress components along the diagonal is referred to as the hydrostatic stress. Hydrostatic stresses cause volumetric expansion or contraction of a cubic stress element. For a material specimen studied in atmosphere conditions, the hydrostatic component of stress is a 3-D tensile stress that has a magnitude of atmospheric pressure P. The hydrostatic stress is the first of three scalar invariants for the total stress tensor. The hydrostatic stress, σ_h , is obtained from the average of normal stress components as:

$$\sigma_h = \frac{\sigma_{xx} + \sigma_{yy} + \sigma_{zz}}{3} = \frac{I_{1\sigma}}{3} \quad (2.7)$$

where $I_{1\sigma}$, from equation (2.7), is the first invariant of the total stress tensor. Sometimes it is desirable to remove the hydrostatic stress from the stress tensor. The total stress tensor always has the contribution of hydrostatic stress in it, while the deviatoric stress tensor excludes the value of hydrostatic pressure and is usually denoted as τ , as is shown as:

$$\tau = \begin{bmatrix} \sigma_{xx} - \sigma_h & \sigma_{xy} & \sigma_{xz} \\ \sigma_{yx} & \sigma_{yy} - \sigma_h & \sigma_{yz} \\ \sigma_{zx} & \sigma_{zy} & \sigma_{zz} - \sigma_h \end{bmatrix} \quad (2.8)$$

Equation (2.8) revealed the first of the three scalar invariants of the total stress tensor. The other two scalar invariants of the total stress tensor are given as:

$$I_{2\sigma} = \frac{1}{2}(\sigma_{ik}\sigma_{ki} - \sigma_{ii}\sigma_{kk}) = \begin{vmatrix} \sigma_{22} & \sigma_{23} \\ \sigma_{23} & \sigma_{33} \end{vmatrix} + \begin{vmatrix} \sigma_{11} & \sigma_{13} \\ \sigma_{13} & \sigma_{33} \end{vmatrix} + \begin{vmatrix} \sigma_{11} & \sigma_{12} \\ \sigma_{12} & \sigma_{22} \end{vmatrix} \quad (2.9)$$

$$I_{3\sigma} = \frac{1}{6}(2\sigma_{ij}\sigma_{jk}\sigma_{ki} - 3\sigma_{ij}\sigma_{ji}\sigma_{kk} + \sigma_{ii}\sigma_{jj}\sigma_{kk}) = \begin{vmatrix} \sigma_{xx} & \sigma_{xy} & \sigma_{xz} \\ \sigma_{xy} & \sigma_{yy} & \sigma_{yz} \\ \sigma_{xz} & \sigma_{zy} & \sigma_{zz} \end{vmatrix} \quad (2.10)$$

2.2. Strain Relations

Materials will tend to change shape and deform under applied stresses. Such deformation is known as dilation, which is volumetric change caused by the normal stress components of the stress tensor. Material deformation is referred as distortion if the shear stress component in the total stress tensor is dominant.

In general, the strain tensor is of second order, with nine components and is defined by both normal, e_{ii} , and shear, e_{ij} , components as:

$$\mathbf{e}_{ij} = \begin{bmatrix} e_{xx} & e_{xy} & e_{xz} \\ e_{xy} & e_{yy} & e_{yz} \\ e_{xz} & e_{yz} & e_{zz} \end{bmatrix} \quad (2.11)$$

The total strain tensor is usually decomposed into two components consisting of the strain tensor, $\mathbf{\epsilon}_{ij}$, and the vorticity/rotational tensor, $\boldsymbol{\omega}_{ij}$, where the components are:

$$\mathbf{\epsilon}_{ij} = \frac{(e_{ij} + e_{ji})}{2} \quad (2.12)$$

$$\boldsymbol{\omega}_{ij} = \frac{(e_{ij} - e_{ji})}{2} \quad (2.13)$$

The strain tensor shown in equation (2.12) is a symmetric 6 component tensor while the rotational tensor, equation (2.13), is an asymmetric 3 component tensor.

2.3. Stress/Strain Constitutive Relations

The materials response is prone to stress, strain, strain rate, and the constitutive equations relating stress and strain components. In this section, materials deformation (elastic and plastic) will be discussed and constitutive models relating applied stress and induced deformation (strain) will be presented.

2.3.1. Elastic Deformation

In general we consider each component of the total stress tensor as having a direct relationship with each component of the total strain tensor. This general case generates $9 \times 9 = 81$ possible components of the elastic modulus tensor. For τ_{ij} and ϵ_{kl} we find that C_{ijkl} has 81 components,

$$\tau_{ij} = C_{ijkl}\epsilon_{kl} \quad (2.14)$$

However, both τ_{ij} and ϵ_{kl} are symmetric tensors ($\tau_{ij} = \tau_{ji}$). This reduces the modulus tensor to 36 independent components.

$$\begin{bmatrix} \sigma_{11} \\ \sigma_{22} \\ \sigma_{33} \\ \sigma_{23} \\ \sigma_{31} \\ \sigma_{12} \end{bmatrix} = \begin{bmatrix} c_{11} & c_{12} & c_{13} & c_{14} & c_{15} & c_{16} \\ c_{21} & c_{22} & c_{23} & c_{24} & c_{25} & c_{26} \\ c_{31} & c_{32} & c_{33} & c_{34} & c_{35} & c_{36} \\ c_{41} & c_{42} & c_{43} & c_{44} & c_{45} & c_{46} \\ c_{51} & c_{52} & c_{53} & c_{54} & c_{55} & c_{56} \\ c_{61} & c_{62} & c_{63} & c_{64} & c_{65} & c_{66} \end{bmatrix} \cdot \begin{bmatrix} \epsilon_{11} \\ \epsilon_{22} \\ \epsilon_{33} \\ \epsilon_{23} \\ \epsilon_{31} \\ \epsilon_{12} \end{bmatrix} \quad (2.15)$$

When the elastic constant matrix is independent of orientation of the material, the material is referred to as mechanically isotropic. Materials such as metal alloys and discontinuous PMMCs are of isotropic form. Because of this isotropic symmetry, the 36 independent elastic constants reduce to 21 terms in the tensor. Most materials display some degree of mechanical symmetry. The materials used in this research study displayed 3 orthogonal planes of symmetry, which reduced the independent elastic constants to 9 parameters.

$$3 \text{ Orthogonal Planes of Symmetry} \begin{bmatrix} c_{11} & c_{12} & c_{13} & 0 & 0 & 0 \\ c_{12} & c_{22} & c_{23} & 0 & 0 & 0 \\ c_{13} & c_{23} & c_{33} & 0 & 0 & 0 \\ 0 & 0 & 0 & c_{44} & 0 & 0 \\ 0 & 0 & 0 & 0 & c_{55} & 0 \\ 0 & 0 & 0 & 0 & 0 & c_{66} \end{bmatrix} \quad (2.16)$$

For an isotropic material, the elastic constants are independent of the orientation of the coordinate axes. This reduces the elastic constant tensor to 2 independent parameters.

$$\text{Isotropic Material} \begin{bmatrix} \beta + 2\mu & \beta & \beta & 0 & 0 & 0 \\ \beta & \beta + 2\mu & \beta & 0 & 0 & 0 \\ \beta & \beta & \beta + 2\mu & 0 & 0 & 0 \\ 0 & 0 & 0 & \mu & 0 & 0 \\ 0 & 0 & 0 & 0 & \mu & 0 \\ 0 & 0 & 0 & 0 & 0 & \mu \end{bmatrix} \quad (2.17)$$

Therefore for an isotropic material, all that is required to characterize the mechanical response of the material is a normal and a shear stress-strain component.

$$\tau_{11} = E\varepsilon_{11} \text{ and } \tau_{12} = G\varepsilon_{12} \quad (2.18)$$

where E and G are the elastic modulus and the shear modulus of the material, respectively.

When a tensile stress in the direction of the x-axis produces an elongation along that axis, it also generates a contraction in the y and z directions. This contraction is described by the Poisson ratio, ν ,

$$\varepsilon_{22} = \varepsilon_{33} = -\nu\varepsilon_{11} = -\frac{\nu\sigma_{11}}{E} \quad (2.19)$$

For most metals and PMMCs the value of Poisson's ratio ranges from 0.28-0.35. Since for an isotropic material, there are two independent variables of modulus (β and μ in equation (2.19)), the tensile elastic modulus, the Poisson's ratio, and the shear elastic modulus are related by:

$$G = \frac{E}{2(1+\nu)} \quad (2.20)$$

Another modulus can be considered that is associated with the volumetric change (dilatometric deformation). This modulus is called the bulk modulus, K , which relates the hydrostatic stress, σ_h , to the dilation, $\Delta = \varepsilon_{11} + \varepsilon_{22} + \varepsilon_{33}$,

$$K = \frac{\sigma_h}{\Delta} = \frac{1}{\delta} \quad (2.21)$$

where δ corresponds to the compressibility. The bulk modulus can be related back to the two elastic modulus and Poisson's ratio by:

$$K = \frac{E}{3(1-2\nu)} = \frac{EG}{(9G-3E)} \quad (2.22)$$

So for an isotropic material, the principal strain component is given by:

$$\varepsilon_{ii} = \frac{1}{E} (\sigma_{ii} - \nu(\sigma_{jj} + \sigma_{kk})) \quad (2.23)$$

The normal stress is related to the normal strain using Hooke's Law:

$$\sigma_{ij} = E\varepsilon_{ij} \quad (2.24)$$

Similarly, the shear stress is related to the shear strain as:

$$\tau_{ij} = G\gamma_{ij} \quad (2.25)$$

2.3.2. Plastic Deformation

Experimentally it has been shown that under uniaxial loading, the strain at a given stress has two distinct parts; the recoverable elastic strain, and the irreversible plastic strain as shown in figure

2.3.

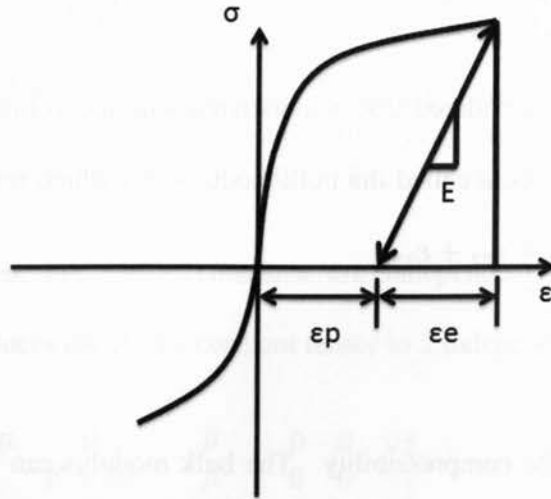


Figure 2.3: Stress-strain diagram undergoing plastic deformation.

The total strain of a specimen is composed of both the elastic and plastic strain components:

$$\varepsilon = \varepsilon^e + \varepsilon^p \quad (2.26)$$

The reversible part of elastic strain is related to the stress through the typical linear elastic equations (Hooke's Law). Plastic constitutive relations are concerned with characterizing the irreversible part.

For multiaxial loading conditions, the general strain increment $d\varepsilon_{ij}$ is decomposed into elastic and plastic parts as:

$$d\varepsilon_{ij} = d\varepsilon_{ij}^e + d\varepsilon_{ij}^p \quad (2.27)$$

Recall that the elastic part of the total strain is related to the stress using the linear elastic equation:

$$C_{ijkl}d\varepsilon_{kl}^e = d\sigma_{ij} \quad (2.28)$$

Before establishing a full description that relates plastic strain to stress, it should first be noted the criteria that predicts the onset of plastic deformation. The general nature of a polycrystalline solid assumes that yield (transition from elastic to inelastic deformation) is independent of hydrostatic stress and that the material is isotropic. The first of these assumptions implies that the yield criterion can only depend on the deviatoric stress components as:

$$S_{ij} = \sigma_{ij} - \frac{\sigma_{kk}}{3} \delta_{ij} \quad (2.29)$$

The assumption of the material being isotropic implies that the onset of yield strictly depends on the magnitudes of the principal stresses, S_1, S_2, S_3 , and can not depend on the principal normal stress directions, and materials yielding is dominantly dependent upon the invariants of the deviatoric stress tensor.

$$J_1 = 0, \quad J_2 = \frac{1}{2} S_{ij} S_{ij}, \quad J_3 = \frac{1}{3} S_{ik} S_{kj} S_{ji} \quad (2.30)$$

The conditions necessary to cause yield of the material can be expressed as $f(\sigma_1, \sigma_2, \sigma_3, \text{material state variables}) = 0$ or $F(J_2, J_3, \text{material state variables}) = 0$, where the material state variables characterizes the strength of the solid.

Upon loading of a ductile material beyond yielding point, unloading, and then re-loading it a further plastic flow in material is induced and the material gains a higher resistance to plastic flow. This phenomenon is known as strain hardening. Strain hardening can be modeled by relating the size and shape of the yield surface to the plastic strain. The easiest way to do this is to make the yield surface increase in size but remain the same shape as the result of plastic deformation. This is known as isotropic hardening. So for isotropic hardening, some appropriate relationship between the material constants of Y or k and the plastic strain is

required. To get a suitable scalar measure of the plastic strain, the accumulated plastic work or accumulated plastic strain magnitude (equations (2.31) and (2.32), respectively) can be used:

$$W = \int \sigma_{ij} d\varepsilon_{ij}^p \quad (2.31)$$

$$\lambda = \int \sqrt{\frac{2}{3} d\varepsilon_{ij}^p d\varepsilon_{ij}^p} \quad (2.32)$$

Then by putting $Y = H(\lambda)$, the function H can be determined by curve fitting a uniaxial tension test. Several other common forms of hardening functions are shown below in figure 2.4

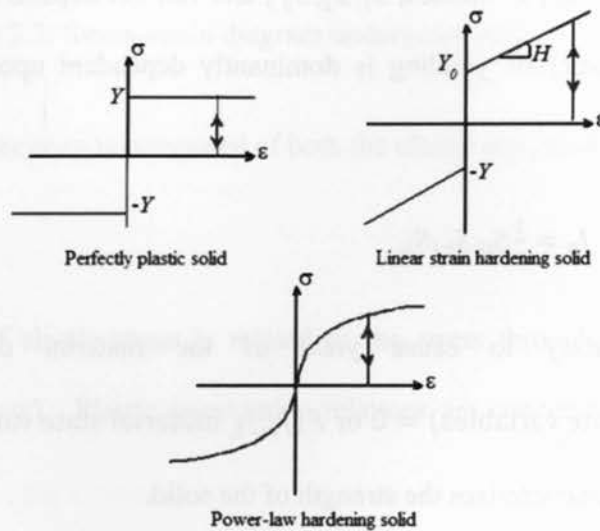


Figure 2.4: Other common hardening functions.

Isotropic hardening laws are generally not very useful in situations where components are subjected to repeated or cyclic loading. Isotropic hardening fails to differentiate materials yielding under tension and compression as to include the Bauschinger's effect.

To account for this effect, the kinematic hardening law was established that allows the yield surface to translate, without changing shape. As the material is deformed in tension, the yield

surface is dragged in the direction of increasing stress. This also allows for the softening of the material in compression, and thus allowing this constitutive law to model cyclic plastic deformation.

There is still a need to calculate the plastic strains induced by loading that exceed the materials yield. The plastic flow rule is a method to calculate these strains. Note that the magnitude of the plastic strain is determined by the hardening rule as the continued plastic flow. This is the case because during continued plastic flow, the stress state must present a point on the yield surface at all times. Since the position for kinematic hardening of the yield surface is related to the magnitude of the plastic strain increment through an appropriate hardening law, it therefore means that the plastic strain magnitude must be related to the stress increment. The plastic strain increment is given as:

$$d\lambda = \sqrt{\frac{2}{3} d\epsilon_{ij}^P d\epsilon_{ij}^P} \quad (2.33)$$

Assuming $f(\sigma_{ij}, \lambda) = 0$ represents the yield criterion, then, the material yielding is defined as:

$$\frac{\partial f}{\partial \sigma_{ij}} d\sigma_{ij} + \frac{df}{d\lambda} d\lambda = 0 \quad (2.34)$$

Equation (2.33) is known as the consistency equation. Rearranging equation (2.33):

$$d\lambda = \frac{1}{h} \frac{\partial f}{\partial \sigma_{ij}} d\sigma_{ij} \quad (2.35)$$

where $h = -\frac{\partial f}{\partial \lambda}$ is the slope of the stress-plastic strain curve under uniaxial loading.

The flow rule can also be applied to develop the plastic strain direction. It is necessary therefore to specify only the ratios of the plastic strain components. The general form of plastic strain is defined as:

$$d\epsilon_{ij}^p = d\lambda G_{ij} \quad (2.36)$$

where G_{ij} is a function of stress and strain history, and needs to be satisfied by $G_{ij} = G_{ji}$ and

$$G_{ij}G_{ij} = \frac{3}{2}.$$

There are restrictions involved in G_{ij} . The first is that plastic strains are volume preserving, so $G_{ii} = 0$. Second, plastic strain increments for crystalline solids are independent of hydrostatic loading, and lastly annealed polycrystalline solids are mainly isotropic at least for small strains.

The constitutive law with these features can be constructed by setting $G_{ij} = \frac{\partial g}{\partial \sigma_{ij}}$, where the function, $g = g(J_2, J_3, \text{strain history, temperature})$, is known as the plastic flow potential for the solid. It must be observed that although the plastic strain magnitude depends on $d\sigma_{ij}$, the ratios of the plastic strain components depends on the current stress, and not the increment in stress.

The associated plasticity model with yield surface must satisfy $f(\sigma_{ij}) = 0$. Therefore, setting $g(\sigma_{ij}) = Cf(\sigma_{ij})$, where the constant C is chosen such that:

$$C^2 \frac{\partial f}{\partial \sigma_{ij}} \frac{\partial f}{\partial \sigma_{ij}} = \frac{3}{2} \quad (2.37)$$

Equation (2.37) ensures that $\sqrt{\frac{2}{3}} d\epsilon_{ij}^p d\epsilon_{ij}^p = d\lambda$. Therefore this gives:

$$d\sigma_{ij}^P = d\lambda C \frac{\partial f}{\partial \sigma_{ij}} \quad (2.38)$$

For a material with an isotropic hardening response, Von-Mises yield function is defined as:

$$\sqrt{\frac{3}{2} S_{ij} S_{ij}} - H(\lambda) = 0 \quad (2.39)$$

$$\text{where } S_{ij} = \sigma_{ij} - \frac{1}{3} \sigma_{kk} \delta_{ij} \text{ and } \frac{\partial f}{\partial \sigma_{ij}} = \frac{3}{2} \frac{S_{ij}}{\sqrt{\frac{3}{2} S_{kl} S_{kl}}}$$

Then plastic strain is expressed as:

$$d\varepsilon_{ij}^P = d\lambda \frac{3}{2} \frac{S_{ij}}{\sqrt{\frac{3}{2} S_{kl} S_{kl}}} \quad (2.40)$$

Equation (2.40) is known as the Levy-Mises flow rule. The Levy-Mises flow law is also often expressed in terms of principal stresses and strains:

$$d\varepsilon_1 - d\varepsilon_2 = d\lambda \sqrt{\frac{3}{2}} \frac{S_1 - S_2}{\sqrt{S_1^2 + S_2^2 + S_3^2}} = d\lambda \sqrt{\frac{3}{2}} \frac{\sigma_1 - \sigma_2}{\sqrt{S_1^2 + S_2^2 + S_3^2}} \quad (2.41a)$$

$$d\varepsilon_1 - d\varepsilon_3 = d\lambda \sqrt{\frac{3}{2}} \frac{S_1 - S_3}{\sqrt{S_1^2 + S_2^2 + S_3^2}} = d\lambda \sqrt{\frac{3}{2}} \frac{\sigma_1 - \sigma_3}{\sqrt{S_1^2 + S_2^2 + S_3^2}} \quad (2.41b)$$

Combining equations (2.41a) and (2.41b):

$$\frac{d\varepsilon_1 - d\varepsilon_2}{d\varepsilon_1 - d\varepsilon_3} = \frac{\sigma_1 - \sigma_2}{\sigma_1 - \sigma_3} \quad (2.42)$$

2.3.3. Elastic Strain Energy

The elastic strain energy is acquired by calculating the area under the stress-strain curve. The calculated area corresponds to the dissipated energy as the material deforms under the applied

strain. Figure 2.5 represents a stress-strain diagram. The area below the stress-strain curve corresponds to amount of energy absorbed by the material undergoing elastic/plastic deformation when subjected to axial loads.

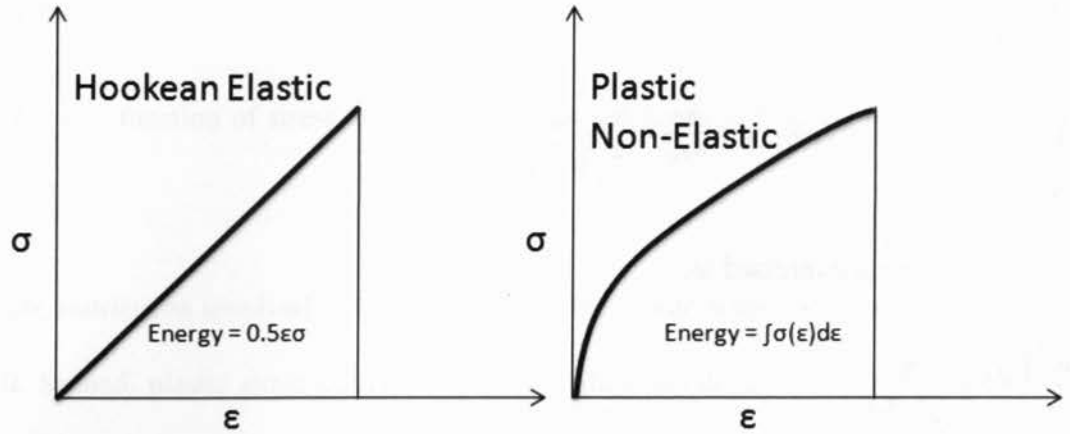


Figure 2.5: Associated generated energy from elastic and plastic stress-strain curves.

To understand the relationship between strain-energy and stress-strain data one can consider that energy is equal to a force, F , applied over a distance, x .

$$dU = F(x)dx = xF(\epsilon)d\epsilon \quad (2.43)$$

The force in the Hookean elastic curve shown in figure 2.5 follows the basic function:

$$F(\epsilon) = AE\epsilon = x^2E\epsilon \quad (2.44)$$

where A is the unit area of the applied stress, which reduces equation (2.44) to:

$$dU = F(x)dx = V_{unit}E\epsilon d\epsilon \quad (2.45)$$

where V is the unit volume of the specimen. The strain energy density, U_0 , is calculated by dividing the energy by the unit volume.

The integration of equation (2.45) leads to:

$$U_0 = \int_{\epsilon=0}^{\epsilon} E \epsilon d\epsilon = \frac{1}{2} E \epsilon^2 = \frac{1}{2} \sigma \epsilon \quad (2.46)$$

Equation (2.46) is applicable for both tensile and shear stress-strain relations. Similarly for a 3-D stress tensor, the strain energy is given as:

$$U_0 = \frac{1}{2} \sigma_{ij} \epsilon_{ij} \quad (2.47)$$

Chapter 3

Finite Element Analysis of Stress-Strain Response of Al 6061 / Al₂O₃-T6 Composite

3.1. Introduction

It is evident that the mechanical behaviour of PMMCs not only depends on the metal matrix microstructure, but also on the load transfer from the metallic matrix through to the rigid reinforcement. This load transfer can be studied through micromechanical models based on the concepts of continuum mechanics. The method of analysis that was employed to study this mechanical behaviour was simulated by modeling a periodic unit cell of the PMMC through Finite Element Analysis (FEA) [26]. These FE models were used to study the interaction between an Al 6061-T6 metallic matrix and Al₂O₃ spherical ceramic particles with volume fractions of 10 and 20 percent versus the un-reinforced Al 6061-T6 matrix metal subjected to uniaxial loading conditions.

The unit cell method of analysis used to formulate the finite element PMMC model is based on the representation shown in figure 3.1, where the PMMC is idealized as a three dimensional array of hexagonal prisms.

The reinforcement particle is located at the centre of each cylindrical metallic matrix, where the size of the particle was determined by the volume percentage of particles in the PMM composite. The amount of volume fraction of particles in the PMMC was equated to the total volume percentage of the single particle in the cylindrical metallic matrix.

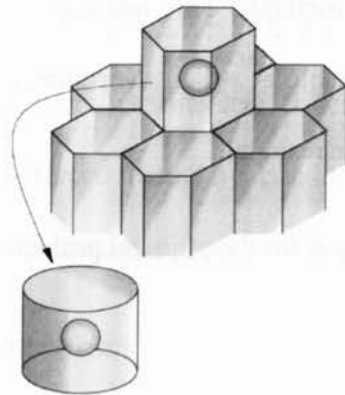


Figure 3.1: PMM composite idealized from a 3-D hexagonal prism to a cylindrical matrix with a spherical particle located at the centre [5].

The idealization of the hexagonal unit cell model transposed into a cylindrical matrix with a single particle located at the centre was first proposed by Tvergaard [27]. The idealized cylindrical unit cell is also required to remain cylindrical during deformation to ensure that the displacement compatibility between neighbouring hexagonal prisms (neighbouring prisms are illustrated in figure 3.1). Therefore the straight lines bounding each cell must remain straight during loading. The reinforcement particle and the surrounding matrix are considered perfectly bonded by maintaining displacement continuity across the interface.

3.2. ANSYS Finite Element Equations

The finite element equations used in the ANSYS solver capture the characteristics of the field equations. The formulation of these equations is based on the governing differential equations or the global energy balance [28].

The approach of utilizing the governing differential equations is known as the method of weighted residuals (Galerkin's method). This method is the approximation of the functional behaviour of the dependent variable at which their substitution into the governing differential equation leads to an error called a residual.

The governing differential equation for the physical problem, as shown as domain D in figure 3.2 is expressed as:

$$L(\phi) - f = 0 \quad (3.1)$$

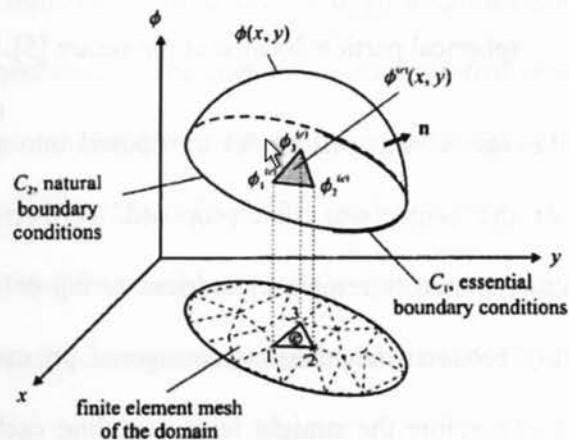


Figure 3.2: Variation of the dependent field variable over a 2D domain [28].

where ϕ is a dependent variable and f is a known forcing function. The ordinary or partial differential operator, L , which has its order specified by p , can be either linear or non-linear. The boundary conditions are set as:

$$B_j(\phi) = g_j \text{ on } C_1 \quad (3.2)$$

and

$$E_j(\phi) = h_j \text{ on } C_2 \quad (3.3)$$

Where B_j and E_j are operators, with $j = 1, 2, 3, \dots, p$. The known functions of g_j and h_j impose the boundary conditions on the dependent variable and its derivatives. The dependent variable over C_1 is referred to as essential/forced boundary conditions, with the derivatives of the dependent variable over C_2 referred to as natural boundary conditions.

The weighted residuals method requires that:

$$\int [L(\tilde{\phi}) - f] W_k dD = 0, \text{ with } k = 1, 2, 3, \dots, n \quad (3.4)$$

where W_k are the weighting functions. These functions approximate the dependent variable as:

$$\phi = \tilde{\phi} = \sum_{k=1}^n \alpha_k W_k \quad (3.5)$$

The unknown coefficients of α_k are found by solving for the system equations, while satisfying the essential boundary conditions on C_1 .

Partitioning the domain, D , into sub-domains or elements, $D^{(e)}$, then applying Galerkin's method with weighting functions $W_k = N_k^{(e)}$ over the elements domain results in:

$$\sum_{e=1}^E \int N^{(e)} (L(\tilde{\phi}^{(e)}) - f) dD = 0 \quad (3.6)$$

where E represents the number of elements and the subscript "e" denoting the specific element whose domain is $D^{(e)}$. The approximation to the dependent variable within the element is expressed as:

$$\tilde{\phi}^{(e)} = \sum_{i=1}^n N_i^{(e)} \phi_i^{(e)} \quad (3.7)$$

or

$$\bar{\phi}^{(e)} = N^{(e)T} \phi^{(e)T} \quad (3.7-1)$$

where

$$N^{(e)T} = \{N_1^{(e)} \quad N_2^{(e)} \quad N_3^{(e)} \quad \dots \quad N_n^{(e)}\} \quad (3.8)$$

and

$$\phi^{(e)T} = \{\varphi_1^{(e)} \quad \varphi_2^{(e)} \quad \varphi_3^{(e)} \quad \dots \quad \varphi_n^{(e)}\} \quad (3.9)$$

with n representing the number of nodes associated with element e . For each element, the nodal unknowns and shape functions are denoted by $\phi_i^{(e)}$ and $N_i^{(e)}$, with $i = 1, 2, \dots, n$, respectively. The shape functions do not need to satisfy the boundary conditions, but they must satisfy the inter-element continuity conditions which are necessary for the assembly of the element equations. The essential boundary conditions are thus imposed after assembling the global matrix. The natural boundary conditions are not implemented directly; however, they have a direct influence on the derivation of the element equations.

The specific order of the element continuity is equal to one less than the highest derivative of the dependent variable appearing in the integrand. This requirement is relaxed by applying integration by parts in the minimization procedure of the residual error in Galerkin's method.

The approach that involves the global energy balance is referred to as the variational method (Rayleigh-Ritz method). The global energy balance approach is utilized to determine the stationary values of global energy. This requires the functional behaviour of the dependent variable to be initially approximated so that the global energy becomes stationary. From

variational calculus, the minimum stationary value leading to stable equilibrium is found when the first variation of the global energy vanishes.

The concepts of differential calculus can be used to perform the minimization of the global energy. In terms of solid mechanics, this concept is known as the principle of minimum potential energy. The correct displacement field satisfying the equilibrium equations is the one that results in the potential energy being an absolute minimum. The solution of both equilibrium equations and boundary conditions is considered exact, however at times can be difficult to construct for complex FE problems. Therefore approximate solutions can be obtained by assuming kinematically acceptable displacement fields with unknown coefficients. The coefficients are determined in such a way that the total potential energy of the system is a minimum [28].

The total potential energy of the structural system, as shown in figure 3.3 is defined as:

$$\pi_p = W + \Omega \quad (3.10)$$

where π_p is the total potential energy, W is the strain energy and Ω is the potential energy that arises due to the presence of body forces, surface tractions, and the initial residual stresses. The strain energy is the capacity of the internal forces/stresses to do work through strains in the structure. For a linearly elastic material, the strain energy of the deformed structure is given as:

$$W = \frac{1}{2} \iiint (\boldsymbol{\varepsilon} - \boldsymbol{\varepsilon}^*)^T \boldsymbol{\sigma} dV \quad (3.11)$$

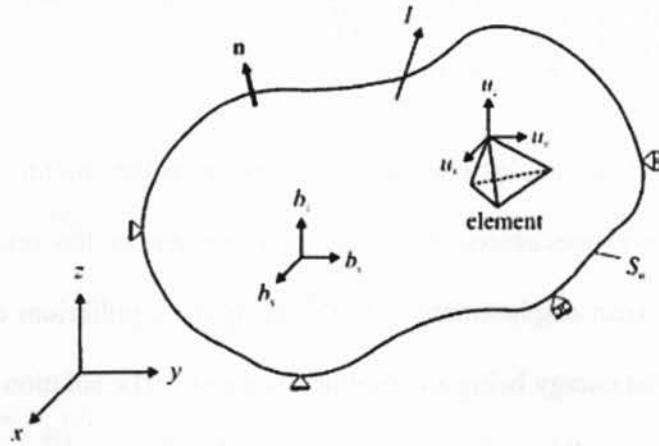


Figure 3.3: A 3D body with displacement constraints, surface tractions, body forces, and concentrated forces.

where σ is the vector of stress components arising from the difference between the total strains, ϵ , and the initial strains, ϵ^* . This stress vector can be better describes as:

$$\sigma = D(\epsilon - \epsilon^*) \quad (3.12)$$

where:

$$\sigma^T = \{\sigma_{xx} \ \sigma_{yy} \ \sigma_{zz} \ \sigma_{xy} \ \sigma_{yz} \ \sigma_{zx}\} \quad (3.13)$$

and

$$\epsilon^T = \{\epsilon_{xx} \ \epsilon_{yy} \ \epsilon_{zz} \ \gamma_{xy} \ \gamma_{yz} \ \gamma_{zx}\} \quad (3.14)$$

The material property matrix D is expressed as:

$$D = \frac{E}{(1+\nu)(1-2\nu)} \begin{bmatrix} 1-\nu & \nu & \nu & 0 & 0 & 0 \\ \nu & 1-\nu & \nu & 0 & 0 & 0 \\ \nu & \nu & 1-\nu & 0 & 0 & 0 \\ 0 & 0 & 0 & (1-2\nu)/2 & 0 & 0 \\ 0 & 0 & 0 & 0 & (1-2\nu)/2 & 0 \\ 0 & 0 & 0 & 0 & 0 & (1-2\nu)/2 \end{bmatrix} \quad (3.15)$$

where σ_{ij} and ϵ_{ij} represent the stress and strain components respectively, with $i, j = x, y, z$ being the Cartesian coordinates. E and ν both represent the elastic modulus and Poisson's ratio in equation (3.15).

The potential energy arising from body forces, surface tractions, and the initial residual stresses are not applicable to the system under analysis for this thesis [28].

3.3. Unit Cell Model

The particular material used in the development of our PMM composite unit cell model is Al 6061-T6 reinforced with 10 and 20 volume percent of aluminum oxide ceramic particles. Details of mechanical properties for both the metallic matrix and ceramic reinforcement can be found in Appendix A (Tables (A1-1) and (A1-3)). Since the PMM composite model is loaded statically beyond its local yield stress, a kinematic hardening curve had to be added to the ANSYS Al 6061-T6 material library, to account for the non-linearity in the Al 6061-T6 alloy matrix during plastic deformation. Figure 3.4 shows the Al 6061-T6 plastic strain-stress curve at room temperature imported into the ANSYS material library.

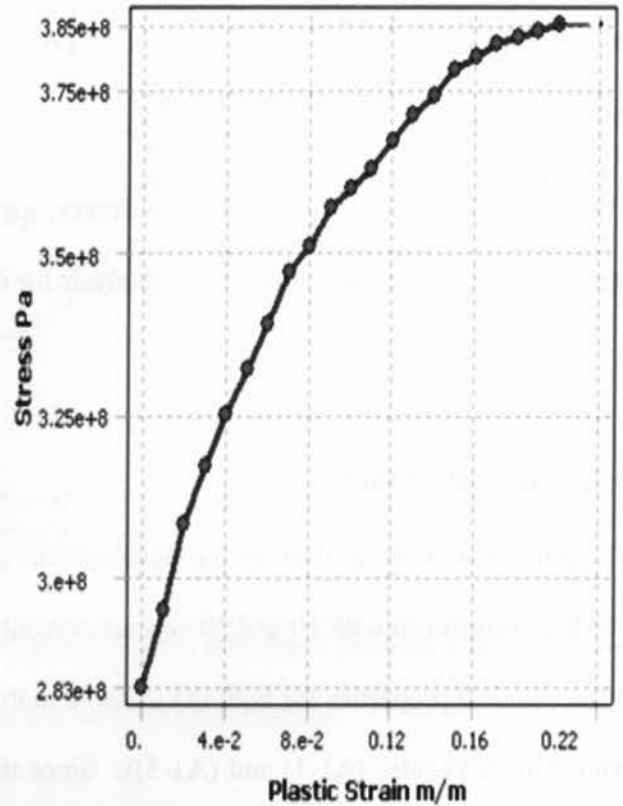
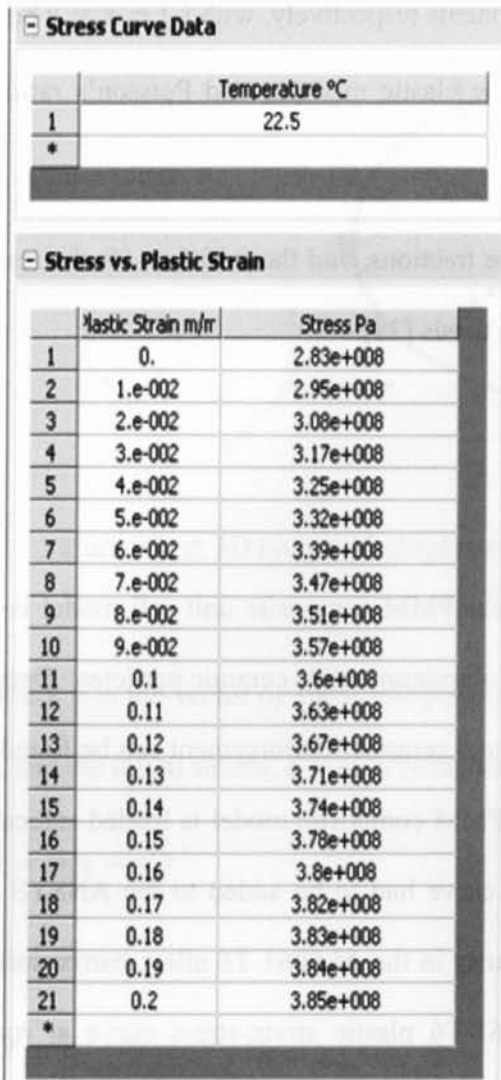


Figure 3.4: Al 6061-T6 plastic strain-stress curve at room temperature.

The stress-strain analysis of the PMMC is a 3D plasticity problem. To properly model this problem the cylinder with the spherical particle inclusion would be representative of one unit cell. Figure 3.5 shows a typical cross-section of a PMM composite unit cell with a spherical particle, representative of the volume fraction of particle reinforcement, at the centre of the cylinder.

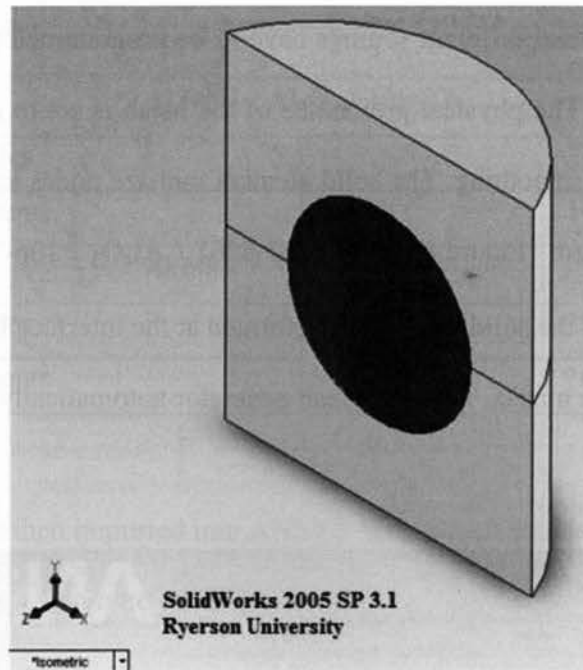


Figure 3.5: Typical cross-section model of a single unit cell PMM composite.

The cylinder dimensions are defined from the condition that the height H is twice as large as its radius. The definition of the matrix cylinder allows for the calculation of the spherical particle radius with the following equation:

$$r^3 = \frac{3 \cdot V_p}{4 \cdot \pi} R^2 H \quad (3.16)$$

In equation (3.16), the value of r represents the spherical particle radius, V_f is the volume fraction of distributed particles, R is the matrix cylinder radius, and H is the height of the cylinder. All calculations were conducted for a model with $H=2R$.

Two physical 3D models were generated with Solidworks 2005 for the PMM composites with the two reinforcement volume fractions of 10 and 20 percent. Each model was imported into ANSYS Workbench 11 where they were first meshed. ANSYS workbench has a built in mesh

generator, however, several different settings have to be programmed to efficiently generate the mesh for the analysis. The physical preference of the mesh is set to mechanical, with medium meshing relevance and smoothing. The solid element midsize nodes and element size were both set to program controlled. Figure 3.6 shows Al 6061 / Al₂O₃ / 10p-T6 PMM composite fully meshed. Refinement of the solid mesh was performed at the interface between the reinforcement particle and the metallic matrix. ANSYS Mesh generator automatically set the mesh shape of the 3D solid to tetrahedral.

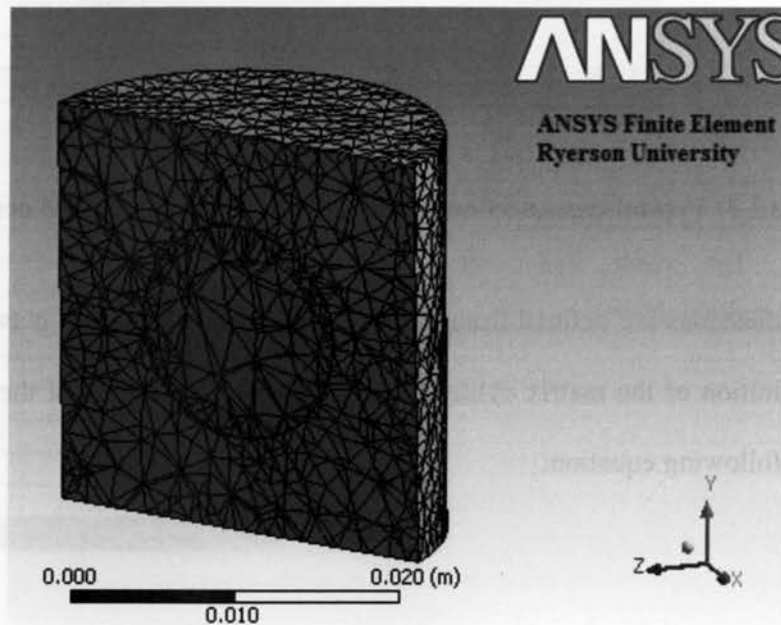


Figure 3.6: Typical Mesh generated for the PMM composite using ANSYS Workbench 11.

Table 3.1 details the meshing properties of the two PMM composites analyzed using ANSYS Workbench 11.

Table 3.1: Meshing properties for both PMM composites.

| Al 6061 / Al₂O₃ / 10p-T6 | |
|---|--------|
| Nodes | 28,345 |
| Elements | 16,316 |
| Al 6061 / Al₂O₃ / 20p-T6 | |
| Nodes | 29,312 |
| Elements | 16,951 |

The generated mesh was then imported into ANSYS Workbench simulation. Once imported, the material properties of the reinforcement particle and metallic matrix were respectively set to Al₂O₃ and Al 6061-T6. Both materials were set to flexible for their stiffness behaviour and with non-linear effects turned on for just the Al 6061-T6 matrix. The model geometry also had to be manipulated by changing the connectivity between the reinforcement particle and the metallic matrix to be perfectly bonded with symmetric behaviour.

The time-stepped static analysis is then set-up to evaluate the stress-strain behaviour of the PMM composite during uniaxial loading. The loading conditions were set to a uniaxial force that was ramped from zero to 100,000 Newton's in the positive y-direction. The boundary conditions were set as to fix the bottom end of the PMM composite and to allow zero displacement in the x and z directions about the outside of the PMMC to maintain compatibility. Due to the high deformation upon loading, the analysis settings were set to large displacement, with program controlled spring stiffness. The output controls were then set to capture the stress and strain data at each individual time step in the analysis.

3.4. Results of Finite Element

The results of a typical normal strain and stress distribution (y-direction) of the Al 6061-Al₂O₃ PMM composite are respectively shown in figures 3.7 and 3.8.

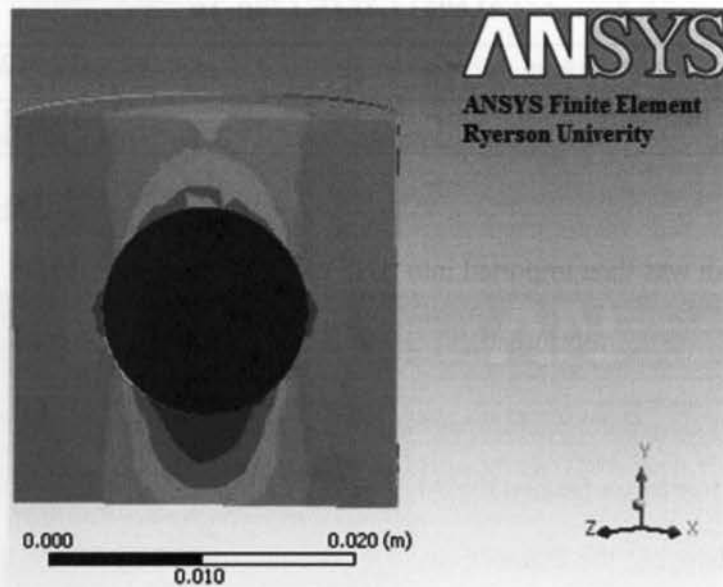


Figure 3.7: Typical normal strain distribution of an Al 6061-T6 PMM composite.

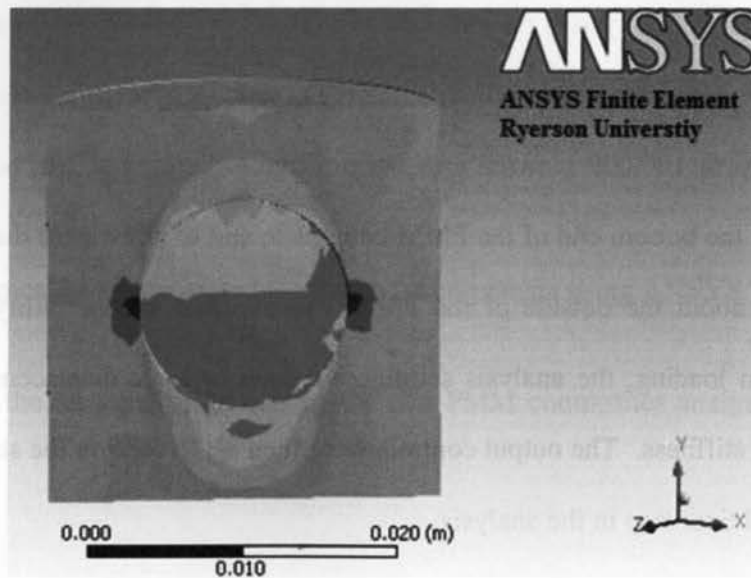


Figure 3.8: Typical normal stress distribution of an Al 6061-T6 PMM composite.

Note that the stress is maximized on either side of the notch where the matrix meets the particle under tensile loading. This is obvious since the occurrence of a notch results in a stress increase locally.

The results of the stress-strain behaviour of both PMM composite simulated models were recorded initially in tabular form within the ANSYS output file and then used to generate the two simulated stress-strain curves shown in figure 3.9. These data are shown in conjunction with the experimental results conducted by Lease [29] for both of the same materials and a typical Al 6061-T6 stress-strain curve.

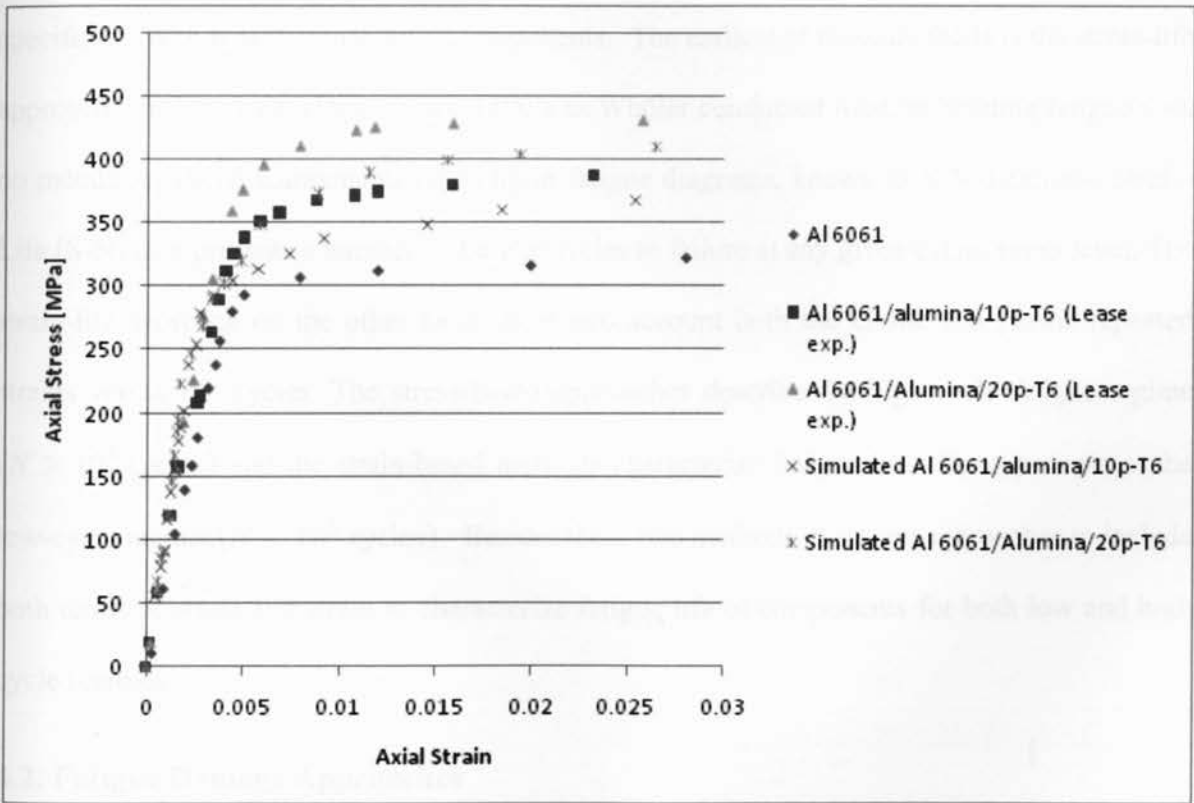


Figure 3.9: Stress-strain diagram of simulated and experimental Al 6061 PPM composites.

The results show a 10% lower stress-strain trend in simulated results as compared with the experimental data collected by Lease [29]. This small discrepancy shows a good agreement of simulated stress-strain curves generated based on FE analysis when compared with experimentally obtained stress-strain data [29] of Al 6061 / Al₂O₃ / 10p-T6 and Al 6061 / Al₂O₃ / 20p-T6.



Chapter 4

Fatigue Damage Approaches

4.1. Fatigue Damage Behaviour of Materials

The word fatigue as defined by the ASTM standards, contained in ASTM E 1150, states in note 1 that “fatigue is the process of progressive localized permanent structural change occurring in a material subjected to conditions that produce fluctuating stresses and strains at some point or points and that may culminate in cracks or complete fracture after a sufficient number of fluctuations [30]. There have been several different methods developed to date that deal specifically with repeated loading of components. The earliest of these methods is the stress-life approach which was developed in the 1800’s as Whöler conducted rotating-bending fatigue tests on metallic material components resulting in fatigue diagrams, known as S-N diagrams. Stress-Life (S-N) data presents a number of fatigue cycles to failure at any given cyclic stress level. The strain-life approach on the other hand takes into account both the elastic and plastic repeated strains versus life cycles. The stress-based approaches describe the high-cycle fatigue regime ($N > 10^5$ cycles) and the strain-based methods characterize fatigue life of components at the low-cycle regime ($N < 10^5$ cycles). Besides these two methods, there are approaches to include both terms of stress and strain to characterize fatigue life of components for both low and high cycle regimes.

4.2. Fatigue Damage Approaches

The damage caused by fatigue on a component increases with the number of applied cycles in a cumulative manner which could result in component failure. The theory of cumulative fatigue

damage has been studied for quite some time, as seen by Palmgren's [31] concept of the linear rule more than 80 years ago. Miner [32] then expressed the linear rule in mathematical form in 1945. Since then, the studies of cumulative fatigue damage models have received increasing attention.

Most cumulative fatigue damage models proposed before the 1970's was predominately phenomenological. These theories were more concerned with the estimation of the total life of components under specific types of loadings. These theories made no distinction of the initiation of the crack and the crack propagation. While those models developed after the 1970's gradually developed into more semi-analytical or analytical theories.

There are three main categories of uniaxial and multiaxial damage models that have been proposed and published throughout literature. The mean stress, energy, and critical plane approaches each have their own strengths and weaknesses. It was not until the early 1970's where multiaxial fatigue research started to become better established. Today, increased research in this area has been conducted both experimentally and theoretically; however, it is yet to establish a fatigue damage theory to universally characterize fatigue damage of materials undergoing loading conditions. The following sections present a few of the most popular damage models employed in this thesis.

4.2.1. Smith-Watson-Topper (S.W.T) Approach

It has been established that tensile mean stress has a detrimental influence on the fatigue life, while compressive mean stresses increase the performance and is also known to increase the fatigue strength of a component. The Smith-Watson-Topper (S.W.T.) parameter was established

to account for the effects of mean stresses in the strain-life approach. The variables of interest with the S.W.T. damage parameter are the maximum stress, σ_{max} , and the strain range, $\Delta\varepsilon$, of the stable hysteresis loop [33]. Figure 4.1 schematically presents a hysteresis loop of a cycle fluctuating with a stress ratio of $R = \frac{\sigma_{min}}{\sigma_{max}} = -1$.

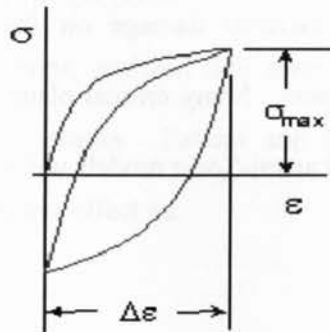


Figure 4.1: Stable hysteresis loop.

The strain range of the hysteresis loop provides the driving force for growing small micro-cracks. The higher the value of maximum stress the easier it is for these micro-cracks to grow. The S.W.T. parameter was proposed to account for this damage as:

$$SWT_{damage} = \sigma_{max} \frac{\Delta\varepsilon}{2} \quad (4.1)$$

A loading cycle with high maximum stress and small strain range cycles can do as much damage as a cycle with low maximum stresses and high cyclic strains.

4.2.2. Critical Plane Approach

One major disadvantage many damage models neglect to account for is that they can not describe the experimentally observed reality that fatigue cracking tends to originate and

propagate along specific critical planes. Researchers have concluded that materials experience either shear dominated or tensile dominated fatigue cracking behaviour. Many materials will exhibit one form of cracking before transitioning to the other during crack propagation. The type of cracking a material will experience is mainly dependent on the material itself, the local state of stress/strain and the magnitude of stresses and strains. The critical plane damage models were developed based on physical material damage on the crystallographic planes where the maximum resolved shear stress acts. Many critical plane damage models have been proposed, however, the Brown-Miller and Fatemi-Socie models will be focused in the present thesis.

4.2.2.1. Brown-Miller Approach

Brown and Miller developed an approach that was based on a physical interpretation of the mechanisms that controlled fatigued crack growth. Brown and Miller figured that the fatigue lives of materials could be correlated by considering both the maximum shear strain and tensile strain acting across the maximum shear strain plane as the principal controlling parameters. Based on this idea, they developed gamma planes, which were essentially contours of constant life plotted with the normal strain value, ϵ_n , on the horizontal axis versus shear strain, γ , on the vertical axis.

Brown and Miller defined two types of cracks that may propagate along these critical planes. Type A cracks and Type B cracks. Type A cracks were defined as long shallow cracks that grew along the surface of the material, much like cracks that are created from torsion loading. Type B cracks grew into the depth of the material. This theory is expressed in equation form as:

$$\Delta\gamma + S\Delta\epsilon_n = \text{constant} \quad (4.2)$$

where $\Delta\gamma$ is the shear range of strain on the plane experiencing the maximum range of shear, $\Delta\epsilon_n$ is the normal strain range on this plane, and S is a material constant.

4.2.2.2. Fatemi-Socie Approach

A few years later after Brown and Miller proposed their critical plane damage theory, Fatemi and Socie, based on their own observations, realized that mean stresses affect the development, density, and orientation of the microcracks. Fatemi and Socie modified the Brown-Miller damage model to include the mean stress effect as:

$$\gamma_{max} \left(1 + K \frac{\sigma_n}{\sigma_y} \right) = constant \quad (4.3)$$

where γ_{max} is the maximum shear strain amplitude, σ_n is the tensile mean stress perpendicular to the plane of maximum shear strain amplitude, σ_y is the materials yield stress and K is a material constant. The value of K varied with fatigue life. For long fatigue lives, the value of K approached 1, while for short fatigue lives the value of K reduced.

4.2.3. Energy Approach

Multiaxial damage models which relate the fatigue life of a specimen to work or strain energy are considered here and are termed energy models. Energy methods have been able to correlate experimentally obtained fatigue lives quite well when measuring with hysteresis loops.

During cyclic loading, energy is absorbed mainly because of plastic deformation. The majority of this mechanical energy is converted into heat, while the remaining part of the energy causes

damage in the material. The magnitude of damage experienced by a material during fatigue cycles is very much dependent on loading inputs and the fatigue resistance of a material is directly related to its capacity to absorb the energy input.

To calculate the total strain energy, the elastic and plastic strain energy components should be calculated separately as:

$$dw_t = dw^e + dw^p \quad (4.4)$$

The elastic strain energy density is defined as:

$$W^e = \int \sigma_{ij} d\varepsilon_{ij}^e \quad (4.5)$$

The stress-strain relationship for an isotropic elastic material is given as:

$$\varepsilon_{ij}^e = \frac{1+\nu}{E} \sigma_{ij} - \frac{\nu}{E} \sigma_{kk} \delta_{ij} \quad (4.6)$$

where ν is the Poisson's ratio, E is the elastic modulus and δ_{ij} is the Kronecker delta which is equal to unity when $i = j$ and zero when $i \neq j$.

The elastic cyclic strain energy is therefore calculated from equation (4.5) for the positive stress parts of the cycle:

$$\Delta W^e = \int_{H(\sigma_i^{min})\sigma_i^{min}}^{H(\sigma_i^{max})\sigma_i^{max}} \sigma_i d\varepsilon_i \quad (4.7)$$

where σ_i and ε_i are the principal stress and strain components, respectively. The Heaviside function [34] $H(\sigma_i)$ is defined as:

$$H(\sigma_i) = 1 \quad \text{for } \sigma_i \geq 0 \quad (4.8a)$$

$$H(\sigma_i) = 0 \quad \text{for } \sigma_i < 0 \quad (4.8b)$$

Substitution of equation (4.6) into equation (4.7) and performing the integration yields:

$$\Delta W^e = \frac{1}{2E} [(I_1^{max})^2 - 2(1 + \nu)I_2^{max}] \quad (4.9)$$

where the first and second invariants of the stress tensor are defined as $I_1 = \sigma_1 + \sigma_2 + \sigma_3$ and $I_2 = \sigma_1\sigma_2 + \sigma_2\sigma_3 + \sigma_3\sigma_1$. For the uniaxial stress state condition, equation (4.9) reduces to:

$$\Delta W^e = \frac{1}{2E} (\sigma_{max})^2 \quad (4.10)$$

The total elastic strain energy is shown graphically in figure 4.2

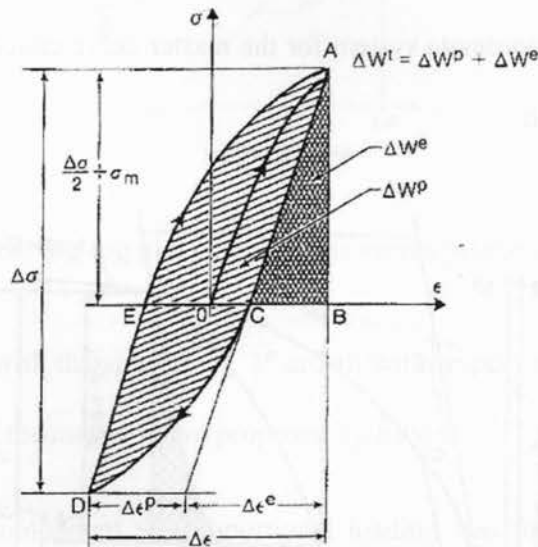


Figure 4.2: Elastic and plastic strain energy densities for a single uniaxial cycle [35].

The plastic strain energy is expressed as:

$$\Delta W^P = \int \sigma_{ij} d\epsilon_{ij}^P \quad (4.11)$$

The stress-strain relationship of the master curve is expressed by Ramberg-Osgood equation:

$$\frac{\Delta \varepsilon}{2} = \frac{\Delta \varepsilon^e}{2} + \frac{\Delta \varepsilon^P}{2} = \frac{\Delta \sigma^*}{2E} + \left(\frac{\Delta \sigma}{2K^*} \right)^{1/n^*} \quad (4.14)$$

where the values of n^* and K^* are found from the best fit log-log curve of the materials true stress versus the plastic strain shown in figure 4.4. The slope of this curve represents the ductility exponent n^* and the magnitude of the true stress at the plastic strain $\varepsilon_p = 1$, corresponds to the materials ductility coefficient K^* .

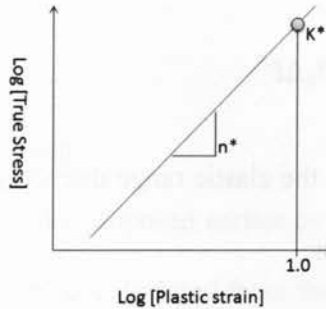


Figure 4.4: log-log plot of true stress versus plastic strain.

Note that measured values with the subscript ()^{*} are all with respect to the master curve origin of 0^{*} shown in figure 4.3 of the master curve proposed by Ellyin.

Finding the plastic strain component for proportional loading was formulated by [35], and is theoretically shown as:

$$\varepsilon_{ij}^P = \frac{3 \cdot S_{ij}^*}{(2K^*)^{1/n^*}} (\bar{\sigma}^*)^{(1-n^*)/n^*} \quad (4.15)$$

Equivalent stress and plastic strain components are defined as:

$$\bar{\sigma}^* = \left(\frac{3}{2} S_{ij}^* S_{ij}^* \right)^{1/2}, \quad \bar{\varepsilon}^P = \left(\frac{2}{3} \varepsilon_{ij}^P \varepsilon_{ij}^P \right)^{1/2} \quad (4.16)$$

Substituting equations (4.15) and (4.16) into equation (4.12) results in equation (4.17). This equation corresponds to the total strain energy density during plastic deformation and is expressed as:

$$\Delta W^P = \int \bar{\sigma}^* d\bar{\epsilon}^P \quad (4.17)$$

The range of equivalent stress and the range of equivalent plastic strain are denoted respectively with $\Delta\bar{\sigma}^*$ and $\Delta\bar{\epsilon}^P$. Referring to figure 4.3, the area of the hysteresis loop denoted by OBCDO is calculated by [36]:

$$\Delta W^P = \frac{1-n^*}{1+n^*} (\Delta\bar{\sigma} - \delta\bar{\sigma}_0) \Delta\bar{\epsilon}^P + \delta\bar{\sigma}_0 \Delta\bar{\epsilon}^P \quad (4.18)$$

where $\delta\bar{\sigma}_0$ reflects the increase in the elastic range due to cyclic strain hardening. This increase in elastic range can be expressed as:

$$\delta\bar{\sigma}_0 = \Delta\bar{\sigma} - \Delta\bar{\sigma}^* = \Delta\bar{\sigma} - 2K^* \left(\frac{\Delta\bar{\epsilon}^P}{2} \right)^{n^*} \quad (4.19)$$

The plastic strain energy density given by equation (4.18) can be expressed in terms of the equivalent stress by transforming the equivalent plastic strain range through equations (4.15) and (4.16):

$$\Delta\bar{\epsilon}^P = 2 \left(\frac{\Delta\bar{\sigma}^*}{2K^*} \right)^{1/n^*} \quad (4.20)$$

Substitution of equation (4.20) into equation (4.18) will thus result in:

$$\Delta W^P = \frac{2(1-n^*)(2K^*)^{-1/n^*}}{1+n^*} (\Delta\bar{\sigma}^*)^{(n^*+1)/n^*} + \frac{2}{(2K^*)^{1/n^*}} \delta\bar{\sigma}_0 (\Delta\bar{\sigma}^*)^{1/n^*} \quad (4.21)$$

Therefore the total strain energy, ΔW^t , is found by adding the elastic strain energy of equation 4.9 with that of the plastic strain energy of equation (4.21):

$$\Delta W^t = \Delta W^e + \Delta W^P \quad (4.22)$$

The calculation of the plastic strain energy density followed a constitutive law relating the plastic strain to the deviatoric stress. The theory used to establish the plastic strain energy followed a deformation type of plasticity theory, which would predict similar results in the case of incremental theory of proportional or nearly proportional loading [37].

4.2.4. Critical Plane-Energy Approach

The critical plane-energy damage model proposed earlier by Varvani [38] integrated the normal energy range and the shear energy range, calculated from the critical plane where the stress and strain Mohr's circles are the largest during loading and unloading reversals of cycles. This damage parameter incorporates both the normal and shear stress and strain components on the critical plane and provides a weighting factor of the normal and shear components using fatigue parameters. The damage parameter also takes into account the effect of mean stress applied, which is applied normal to the plane of maximum shear. Also, the parameter increases with the addition of hardening caused by out-of-phase straining, while this is neglected to be accounted for in earlier developed strain based damage parameters.

Varvani's damage parameter has been formulated for uniaxial and multiaxial fatigue conditions. For a thin-walled tubular specimen, the strain and stress tensors subjected to both axial and torsional fatigue are given by:

$$\Delta \varepsilon_{ij} = \begin{pmatrix} -v_{eff} \Delta \varepsilon_{ap} & \Delta \left(\frac{\gamma_{ap}}{2} \right) & 0 \\ \Delta \left(\frac{\gamma_{ap}}{2} \right) & \Delta \varepsilon_{ap} & 0 \\ 0 & 0 & -v_{eff} \Delta \varepsilon_{ap} \end{pmatrix} \quad (4.23)$$

$$\Delta \sigma_{ij} = \begin{pmatrix} 0 & \Delta \tau_a & 0 \\ \Delta \tau_a & \Delta \sigma_a & 0 \\ 0 & 0 & 0 \end{pmatrix} \quad (4.24)$$

The values of axial strain range $\Delta \varepsilon_{ap}$ and shear strain range $\Delta \left(\frac{\gamma_{ap}}{2} \right)$ are given as:

$$\Delta \varepsilon_{ap} = \Delta \varepsilon_a \sin \theta \quad (4.25)$$

$$\Delta \left(\frac{\gamma_{ap}}{2} \right) = \Delta \left(\frac{\gamma_a}{2} \right) \sin(\theta - \phi) \quad (4.26)$$

where $\Delta \varepsilon_a$ and $\Delta \left(\frac{\gamma_a}{2} \right)$ are the values of the applied axial and the shear strain amplitude respectively. The value of θ responds to the angle during a cycle of strain at which the Mohr's circle is the largest and has a maximum value of shear strain. The phase delay ϕ represents the delay between the strains on the axial and the torsional axes. Also, from equation (4.24), $\Delta \sigma_a$ and τ_a represent the axial and shear stress ranges. From equation (4.23), the value of effective Poisson's ratio, v_{eff} , is calculated to be:

$$v_{eff} = \frac{v_e \varepsilon_e + v_p \varepsilon_p}{\varepsilon_e + \varepsilon_p} \quad (4.27)$$

where the value of elastic Poisson's ratio, v_e , is less than 0.5, while the value of plastic Poisson's ratio, v_p , is equal to 0.5. The elastic and plastic strains in equation (4.27) are found to be:

$$\varepsilon_e = \frac{\sigma_a}{E} \quad (4.28a)$$

$$\varepsilon_p = \varepsilon_{ap} - \frac{\sigma_a}{E} \quad (4.28b)$$

The critical plane in which both the strain and stress on the Mohr's circle is largest, represents the values of maximum shear strain and the corresponding normal strain range for the loading, θ_1 , and un-loading, θ_2 angles. These values of maximum shear and normal strain range are both found as:

$$\Delta \left(\frac{\gamma_{max}}{2} \right) = \left(\frac{\varepsilon_1 - \varepsilon_3}{2} \right)_{\theta_1} - \left(\frac{\varepsilon_1 - \varepsilon_3}{2} \right)_{\theta_2} \quad (4.29a)$$

$$\Delta \varepsilon_n = \left(\frac{\varepsilon_1 + \varepsilon_3}{2} \right)_{\theta_1} - \left(\frac{\varepsilon_1 + \varepsilon_3}{2} \right)_{\theta_2} \quad (4.29b)$$

The values of principal strains ε_1 , ε_2 and ε_3 are calculated straight from the strain Mohr's circle. Figure 4.5(a) depicts graphically the principal strains on the Mohr's circle.

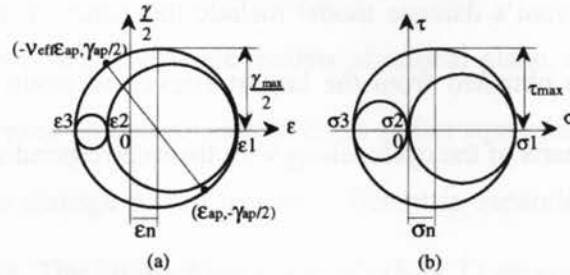


Figure 4.5: (a) Strain Mohr's circle; (b) Stress Mohr's circle [38].

where the values of principal strain are found to be:

$$\varepsilon_1 = (1 - \nu_{eff}) \frac{\varepsilon_{ap}}{2} + \frac{1}{2} \left[\varepsilon_{ap}^2 (1 + \nu_{eff})^2 + \left(\frac{\gamma_{ap}}{2} \right)^2 \right]^{1/2} \quad (4.30a)$$

$$\varepsilon_2 = -\nu_{eff} \varepsilon_{ap} \quad (4.30b)$$

$$\varepsilon_3 = (1 - \nu_{eff}) \frac{\varepsilon_{ap}}{2} - \frac{1}{2} \left[\varepsilon_{ap}^2 (1 + \nu_{eff})^2 + \left(\frac{\gamma_{ap}}{2} \right)^2 \right]^{1/2} \quad (4.30c)$$

The maximum shear stress range and its corresponding normal stress range are found from the largest stress Mohr's circle (figure 4.5(b)) during the loading and un-loading reversals of fatigue cycles:

$$\Delta\tau_{max} = \left(\frac{\sigma_1 - \sigma_3}{2}\right)_{\theta_1} - \left(\frac{\sigma_1 - \sigma_3}{2}\right)_{\theta_2} \quad (4.31a)$$

$$\Delta\sigma_n = \left(\frac{\sigma_1 + \sigma_3}{2}\right)_{\theta_1} - \left(\frac{\sigma_1 + \sigma_3}{2}\right)_{\theta_2} \quad (4.31b)$$

The principal stresses, σ_1 , σ_2 and σ_3 are calculated from the stress Mohr's circle as:

$$\sigma_1 = \frac{\sigma_a}{2} + \frac{1}{2}[\sigma_a^2 + 4\tau_a^2]^{1/2} \quad (4.32a)$$

$$\sigma_2 = 0 \text{ (Plane Stress)} \quad (4.32b)$$

$$\sigma_3 = \frac{\sigma_a}{2} - \frac{1}{2}[\sigma_a^2 + 4\tau_a^2]^{1/2} \quad (4.32c)$$

The components of Varvani's damage model include the range of maximum shear stress and shear strain which were obtained from the largest stress and strain Mohr's circle during the loading and un-loading parts of the cycle, along with their corresponding normal stress and strain range on that plane:

$$\frac{1}{(\sigma'_f \varepsilon'_f)} (\Delta\sigma_n \Delta\varepsilon_n) + \frac{1}{(\tau'_f \gamma'_f)} \left(\Delta\tau_{max} \Delta\left(\frac{\gamma_{max}}{2}\right) \right) = f(N_f) \quad (4.33)$$

where the values of σ'_f and ε'_f are the axial fatigue strength and ductility coefficients, respectively, and τ'_f and γ'_f represents the shear fatigue strength and ductility coefficient, respectively. These coefficients are better understood graphically, as shown in figure 4.6.

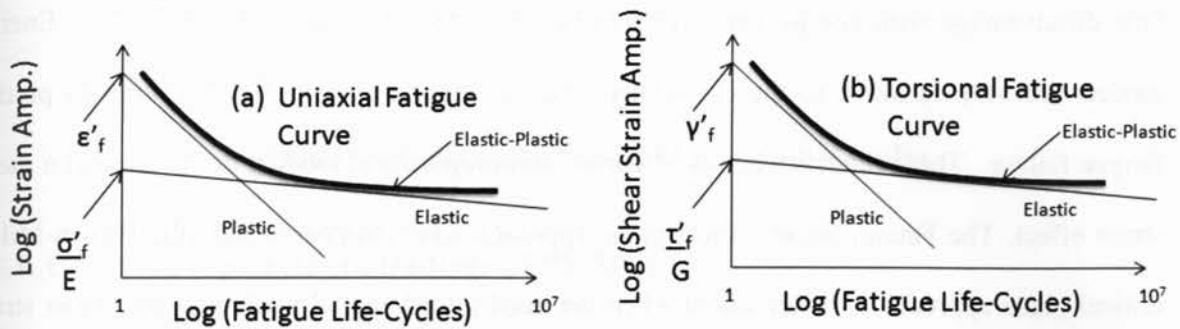


Figure 4.6: Graphical representation of fatigue life-strain curve for (a) axial strain (b) shear strain

[38].

4.3. Comparison of Damage Approaches

4.3.1. Advantages/Disadvantages

The stress and the strain based damage parameters are among the first models to evaluate fatigue life of components. Other fatigue damage models of critical plane, energy, and critical plane-energy were developed based on components of stress and/or strain for low-cycle and high-cycle fatigue regimes. Fatigue damage parameters are different in capability and they possess some strengths and weaknesses. The Smith-Watson-Topper (S.W.T) approach is applied to correlate the fatigue life of components when fatigue failure is dominantly due to tensile cracking. When tensile cracking was the dominant crack mode, the S.W.T. model showed a good ability to account for the effects of cyclic hardening or softening [39]. However, the S.W.T. model can not predict the tension-compression loading cases when the maximum stress applied are very low.

Both the critical plane and energy models have been equally successful in correlating experimental fatigue life data. Since energy based models reflect the path dependency of the fatigue process, this allows for explicit consideration of the multiaxial stress-strain response.

One disadvantage with energy approaches is that they tend to diverge at long lives. Energy models are very sensitive to the constitutive model employed when they are used to predict fatigue failure. These models when used during non-proportional loading do not predict a mean stress effect. The Fatemi-Socie critical plane approach when compared with the Brown-Miller critical plane approach is better suited when the need for additional hardening and mean stress have to be accounted for. Also, both critical plane models require a damage parameter constant for each specific material and loading condition. This makes the use of these models difficult when there is limited information regarding the materials cyclic fatigue. Critical plane models have also been criticized for their lack of adherence to rigorous continuum mechanics fundamentals. The critical plane-energy model of Varvani has successfully correlated multiaxial fatigue life damage for various in-phase and out-of-phase multiaxial fatigue straining conditions, where a mean stress was applied normal to the maximum shear plane and during out-of-phase fatigue tests where additional hardening is experienced.

Chapter 5

Damage Assessment of PMMCs and Results

5.1. General Parameters in Damage of PMMCs

5.1.1. Crack Initiation and Growth

PMMC's have complex fatigue behaviour, which are mainly affected due to the incorporation of reinforcement [25]. Extensive research in crack initiation of silicon carbide and alumina reinforced aluminum matrix has been performed [25,40]. Many different sources of crack initiation have been identified with these materials. Crack initiation is mostly due to fracture of the reinforcement particle, decohesion of the reinforcement from the matrix, fracture of large particles and porosity in the composite.

Reinforcement materials are very brittle in nature. These particles usually fracture in the initial stages of fatigue during the first few cycles. Microcracks then advance into the matrix alloy. This phenomenon is due to the high local strain concentration produced by microcracks in the reinforcement with the surrounding matrix. This form of crack initiation is most commonly observed in PMMCs reinforced with alumina [41,42].

The decohesion of the reinforcement from the matrix usually occurs in the interface between the reinforcement and the matrix, or in the matrix near the matrix-reinforcement interface. This is most commonly found in PMMCs reinforced with silicon carbide [43]. In most cases of decohesion, cracks are initiated from particle clusters [44]. Large inclusions and intermetallics in the PMMC are prone to fracture because of their brittle nature. This crack initiation behaviour is

most commonly seen with 2000 series aluminum alloy matrices because of their high alloy content [45].

Fatigue cracks can also initiate in MMCs due to porosity. A PMMC containing large pores will typically fail due to a fatigue crack initiated from one of these pores. When PMMCs are produced through liquid metallurgy, pores will typically arise from incomplete penetration of the metal matrix alloy into the particle cluster [46]. Fatigue cracks initiate at or near the surface of a PMMC material, regardless of the initiating defect. This verifies that surface defects are exposed to higher cyclic plastic strains, and once fractured, exposed to higher stress-intensity factors than those defects located within a bulk material. Consequently, cracks initiate far earlier from surface defects than the interior of the material, and thus grow faster once initiated [13].

The fatigue life of PMMCs is increased under load-controlled conditions due to the increase in the materials stiffness and strength [47]. An increase in fatigue life is attributed to the higher elastic modulus of PMMCs than its metallic matrix. Under load-controlled fatigue conditions a PMMC displays a lower total strain as compared with its base alloy, resulting in an increased life. In strain-controlled condition, the strain in PMMC and the base alloy are the same (isostrain condition), but the stress in the PMMC material would be higher. The higher stress levels in the PMMC result in fracture or decohesion of the reinforcement, and therefore reduce the fatigue life of materials.

The direction of crack growth in PMMCs is driven by the interaction between the reinforcement particles and the fatigue crack. This is because reinforcement particles change the stress field surrounding the crack tip. This change in stress-field depends on factors such as whether or not the particle fractures, decoheres, or remains intact during fatigue cycles. Therefore the main

factors controlling the fatigue process of PMMCs are the reinforcement type, reinforcement volume fraction and size, and the matrix aging condition.

5.1.2. The Effect of Particle Size and Volume fraction

To date, it is difficult to find any direct comparisons between the fatigue behaviour of similar alloys reinforced with various types of particles. This is due to the pre-eminence of silicon carbide as the reinforcing particle type for MMCs. For elongated particles, such as whiskers, they will inhibit crack growth when the fatigue crack is propagating perpendicular to the particle and accelerates the crack growth when propagating parallel to the particle [48]. The effect of reinforcement volume fraction varies with the average size of the reinforcement. It has been observed that an increase in volume fraction decreases the fatigue crack growth rate when the MMC is reinforced with large particles ($>10\mu\text{m}$) [49] and increases the fatigue crack growth rate in MMCs reinforced with small particles ($<3\ \mu\text{m}$) [45]. This difference of fatigue crack growth rate arises from the fact that a fatigue crack reacts differently when interacting with particles of various size. When a fatigue crack interacts with a small particle, the particle tends to constrain the crack growth since smaller particles have fewer tendencies to fracture when compared to large particles. This results in a flat fracture path, low levels of roughness induced closure, and faster fatigue crack growth. For a given reinforcement volume fraction, MMCs with larger particles tend to be distributed further apart from one another. Since these larger particles are more prone to fracture when compared to smaller particles, they tend to promote the fatigue crack.

5.1.3. The Effect of Aging Treatment

For un-reinforced aluminum alloys, the fatigue crack growth threshold decreases with the increased aging [50]. The aging treatment changes the slip characteristics of the metal matrix. When particles are introduced to the matrix, they suppress this effect [51]. This suppression is because fatigue cracks are more likely to grow towards cracked particles and leave behind un-cracked small particles. Therefore, the crack propagation path is controlled by the size, spacing, and fracture characteristics of the reinforced particles.

5.2. Fatigue Tests and Data

The techniques, specimens, and equipment used in fatigue testing of un-reinforced metal alloys resemble those used for the testing of PMMCs. The difference lies in the preparation of PMMCs when compared with base alloys. This section presents materials and fatigue test data available in literature [10,45,56,57] employed in this thesis. Four sets of PMMC alloys fatigue tested under various conditions were described in detail.

5.2.1. Aluminum 6061 / Al₂O₃ / 20p-T6

The material used in this study is made commercially available with an aluminum 6061 metal alloy matrix with 20 % by volume of aluminum oxide (Al₂O₃) particles. This PMMC is manufactured by Duralcan in the USA. It is produced in large batches by mixing molten aluminum and ceramic particles using their own proprietary methods [52]. The material used for this data set was produced by extruding the PMMC at 350°C through a 2-hole extrusion die, with the final solid circular rod having a diameter of 31.7mm. Prior to component machining, the

PMMC was heat treated to the T6 condition. The distribution of aluminum oxide particles remained essentially macroscopically isotropic and there was little direction dependency of any mechanical properties of the final material specimen. Table 5.1 details the uniaxial properties of aluminum oxide, aluminum 6061-T6 and 6061 / Al₂O₃ / 20p-T6.

Table 5.1: Uniaxial mechanical properties of Al 6061 / Al₂O₃ / 20p-T6 and its constituents [53,54].

| | Young's Modulus [GPa] | Poisson's Ratio | 0.2% Yield Strength [MPa] | Ultimate Strength [MPa] | Elongation [%] |
|--|------------------------------|------------------------|----------------------------------|--------------------------------|-----------------------|
| Aluminum Oxide | 399 | 0.25 | NA | NA | NA |
| 6061-T6 | 69 | 0.33 | 276 | 310 | 20 |
| 6061 / Al ₂ O ₃ / 20p-T6 | 97 | 0.31 | 351 | 372 | 4 |

In Table 5.1 the inclusion of ceramic particles in the alloy matrix improved the stiffness of the material by almost 41%. The yield and ultimate strength of the PMMC is also improved from that of the base alloy by 27% and 20% respectively. However, due to the increase in stiffness caused by the ceramic particles, the elongation percentage of the PMMC is reduced by 80%.

Fatigue tests were performed on Al 6061 / Al₂O₃ / 20p-T6 specimens under strain-controlled tensile, torsional, and tensile-torsion conditions. Tests were conducted at room temperature using a digitally controlled, closed-loop, servo hydraulic testing machine with a constant amplitude, fully reversed loading condition (R= -1). For all the loading cases performed on this material, the high amplitude tests were run at a frequency of 0.5 Hz and low amplitude tests were run at 1 Hz. Proportional loading was performed for all combined uniaxial/torsion tests, at the biaxial strain ratio of:

$$\lambda = \frac{\frac{\Delta\gamma}{2}}{\frac{\Delta\varepsilon}{2}} = \sqrt{3} \quad (5.1)$$

The value of the biaxial strain ratio was chosen such that the axial and shear strain amplitudes levels could be considered equivalent according to the von Mises criteria. For the torsional and combined uniaxial/torsional cases, the tests were first run at strain-controlled until the torque or torque/loads were stabilized, then the tests would resume under torque or torque/load settings. This is common procedure to avoid unnecessary damage to the extensometer at failure.

Figures 5.1a and 5.1b presents specimen geometries used for the fatigue tests for this material. The dimensions shown in this figure correspond to the recommended uniaxial low cycle fatigue specimen design based on ASTM E606 [55]. Figure 5.1b shows a tubular shaft, which is common to use for torsional and combined axial/torsional fatigue tests since a uniform shear stress and shear strain distribution is assumed constant over the wall thickness.

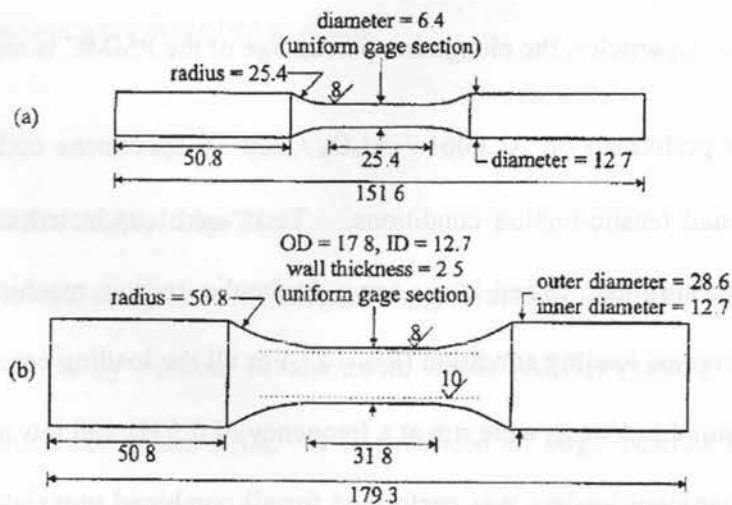


Figure 5.1: Test specimen geometries (a) uniaxial specimen, (b) tubular specimen used for torsional and uniaxial/torsion tests (dimensions in mm) [56].

The life calculations performed during these tests assumed that the fatigue failure of the specimens was controlled by the state of stress and strain on the materials outer surface. Because of this assumption, the outer surface stress/strain states for each loading case was required to be stabilized based on the experimentally obtained data. For the uniaxial loading case, the axial stress was found directly from the stabilized experimental load amplitude using the specimen original test cross-sectional area.

5.2.2. Aluminum 6061 / Al₂O₃ / 22p-T6

The material data was WD-22A also of Duralcan, USA. This material is a 6061-T6 aluminum alloy matrix reinforced with 22 volume percent of aluminum oxide particles. The fatigue test specimens used were cut from extruded tubes that measured with an outside diameter of 45mm and with a wall thickness of 2mm. Figure 5.2 shows the geometric dimension of the extruded tube used for fatigue tests.

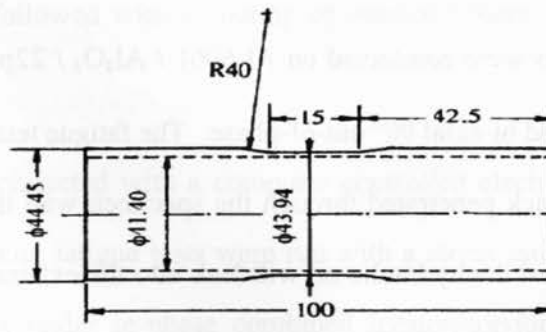


Figure 5.2: Geometry of the thin-walled tubular specimens used for multiaxial fatigue testing

[57].

The PMMC specimens were heat-treated to a T6 condition, then after treatment, the specimens were machined to the final dimensions shown in figure 5.2. Fatigue tests were performed using a servo-hydraulic closed loop machine. The combined uniaxial/pure shear tests were subjected to internal and external pressures (P_i and P_e) with an axial force of F . A schematic diagram of the test machine is shown in figure 5.3 where it is seen how the uniaxial and internal pressures are applied during fatigue test loading.

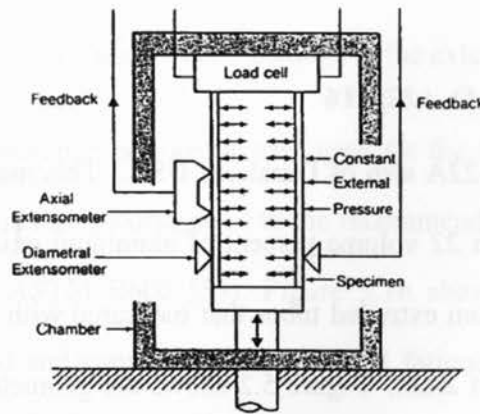


Figure 5.3: Schematic diagram of the test set-up rig [57].

Four types of fatigue tests were conducted on Al 6061 / Al_2O_3 / 22p-T6; uniaxial tension, pure shear, bi-axial in-phase and bi-axial 90° out-of-phase. The fatigue tests would automatically stop cycling once a fatigue crack penetrated through the specimen wall thickness. Once a through-the-wall crack has occurred the hydraulic oil will leak into the external pressure system, causing a loss in pressure in the internal system. Any loss in pressure to the internal system halts the testing of the specimen. For the uniaxial fatigue testing, a relatively small amount of internal pressure was needed to detect cracks without any significant effect on the specimens stress state (≤ 10 MPa in hoop stress)

5.2.3. Aluminum 6061 / SiC / 17w-T6

The two materials tested in this investigation was un-reinforced Al 6061 and Al 6061 reinforced with 17% silicon carbide whisker particulate. The composite was produced through a squeeze casting process. Table 5.2 details the mechanical properties of the PMMC and its matrix constituent.

Table 5.2: Mechanical properties of Al 6061 PMMC and the base alloy [10,45].

| Material | Ultimate Strength [MPa] | Elastic Modulus [GPa] | Elongation [%] |
|--------------------|--------------------------------|------------------------------|-----------------------|
| Al 6061-T6 | 348 | 72 | 33.2 |
| Al 6061/SiC/17w-T6 | 559 | 114 | 10.6 |

The average diameter and length of the whiskers was respectively $0.84\mu\text{m}$ and $4.86\mu\text{m}$. The PMMC was heat-treated to the T6 condition. Initially the extruded PMMC had a circular diameter of 18.9mm, however, after machining and smoothing the dimensions became 8mm in diameters with a gauge length of 5mm. The surfaces of the test specimens were polished with emery papers and then followed with a coating of diamond paste, which gave the material a mirror finish.

The fatigue tests were conducted with a computer controlled electro-hydraulic tension-torsion testing machine. The cyclic fatigue tests were run with a stress ratio of $R=0.1$, and at a stress cycle frequency of 5 Hz under in-phase combined tension-torsion loading. All tests were conducted using load-control conditions, where the combined stress ratio of α ($\alpha = \tau_{\text{max}}/\sigma_{\text{max}}$) remains constant. Where α varied from 0 for pure tension to ∞ for pure torsion.

5.2.4. Ti-6Al-4V / TiC / 10p

This material is referred as CermeTi-10, a titanium alloy (Ti-6Al-4V) matrix reinforced with 10% by weight of titanium carbide particles. The PMMC was produced by a method of cold and hot isostatic pressing. This process blended the Ti-6Al-4V powder with the titanium carbide particles until a uniform distribution of particles was established. Then the blended mixture of matrix powder and particulate was subjected to cold isostatic pressing, followed then by a vacuum sintering. Then the sintered pre-form was hot isostatically pressed. This last process made use of high temperature and pressure to produce the full density of the material. After hot isostatic pressing, the material was furnace cooled. Complete test specimens contained small amounts of porosity and particle clustering. The small amounts of bulk defects did not effectively change the perception of the material from having a uniform particle distribution and to idealize the material as isotropic.

Fatigue tests conducted [58] were performed at 538°C in an air environment. The testing apparatus used was a servocontrolled MTS axial-torsion mechanical machine. Tests 1 and 2 were subjected to fully reversed cyclic loading with a strain range of 1 % with a strain rate of $8.3 \times 10^{-5} s^{-1}$. The criterion for failure considered during testing of this material, aside from complete fracture, was based on the concept of a crack propagating to a given size. For the fully reversed case, failure can be seen as the drop in maximum stress that is not matched by that of the minimum stress. During uniaxial cyclic fatigue tests, the drop in maximum stress was effectively followed by complete rupture of the material. Therefore failure of the material during uniaxial tests was considered at the point where this maximum stress dropped. For the biaxial tubular specimen tests, failure was seen when the peak tensile stress reduced by more than 50% with a developing cusp on the compression side of the hysteresis loop. For the torsion tests, an

analogous rule was applied to determine specimen failure. Tests 3 and 4 are also pure tensile cyclic fatigue tests, however, test 3 was conducted with a strain ratio of 0.6% and strain rate of $8.3 \times 10^{-5} s^{-1}$ while test 4 was conducted with a strain ratio of 1% and a strain rate of $8.3 \times 10^{-6} s^{-1}$. Tests 14 and 15 were subjected to a strain-controlled cyclic loading in pure torsion. Both tests were conducted at a controlled shear strain ratio of 1.2% and strain rate of $8.3 \times 10^{-5} s^{-1}$. Lastly, test 16 was subjected to a 90° out-of-phase axial-torsion cyclic fatigue test. The axial and shear strain ranges were, respectively, 0.7% and 1.2%, and the strain rates in tension and torsion were set at $5.9 \times 10^{-5} s^{-1}$ and $10.2 \times 10^{-5} s^{-1}$, respectively.

Figures 5.4a-d represents stress-fatigue life data of the four different PMMC materials under various uniaxial and multiaxial fatigue loading conditions studied in this thesis.

5.3. Results of Fatigue Damage Assessment

This section presents fatigue damage assessment of various PMMCs tested under various fatigue loading conditions using the most popular damage approaches including Smith-Watson-Topper, Brown-Miller, Fatemi-Socie, and Ellyin. The Varvani critical plane-energy damage approach will be thoroughly outlined in chapter 6. Material characteristics and calculated damage results based on various approaches are tabulated in Tables presented in Appendix A.

5.3.1. Smith-Watson-Topper Damage Assessment

Smith-Watson –Topper damage parameter is determined by accounting for the mean stress effect during the strain-life approach. This section will examine the capability of the S.W.T. damage parameter to assess fatigue damage of components subjected to pure tension, torsion, and combined tension-torsion fatigue loading conditions.

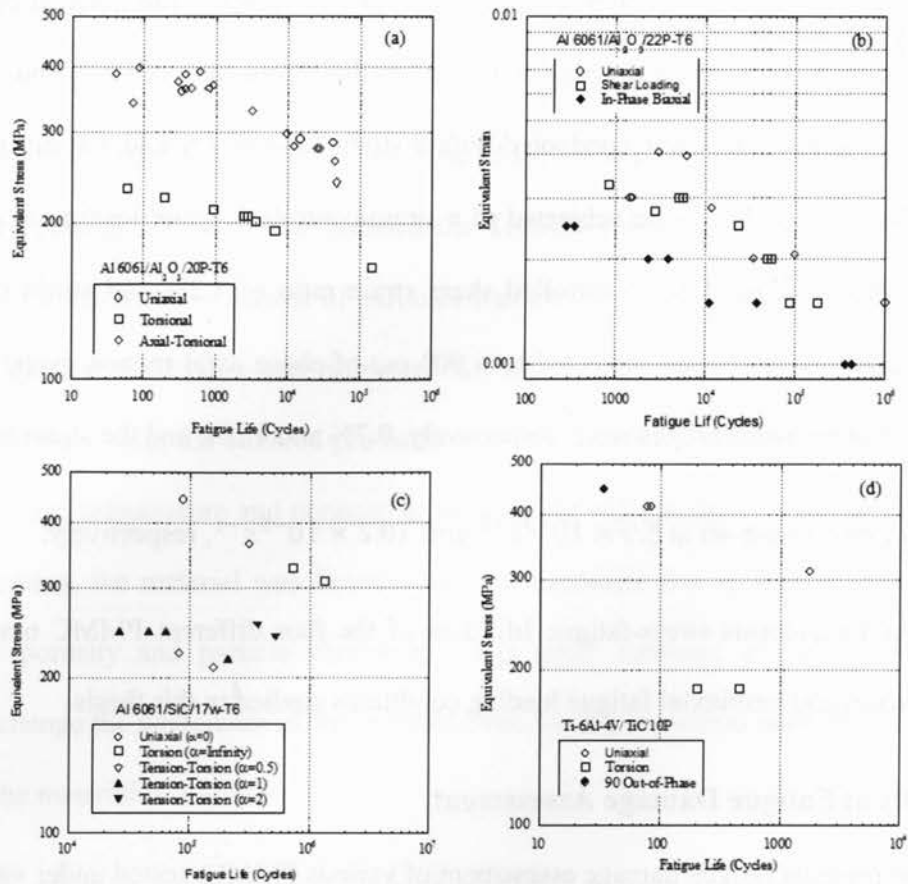


Figure 5.4: Stress-Life data for the four PMMC materials examined in this thesis [46,56,57,58].

This fatigue damage parameter was developed based on the components of the strain amplitude ($\Delta\epsilon/2$) and the maximum normal stress (σ_{max}) obtained from the Mohr's circles. For torsion fatigue loading, S.W.T. damage parameter becomes the product of the shear strain amplitude ($\Delta\gamma/2$) and the maximum shear stress (τ_{max}). For the multiaxial fatigue loading case, the damage parameter is calculated by the summation of the two products mentioned above for both the shear and tensile damage components.

The procedure of damage analysis based on S.W.T. parameter is outlined in a flowchart presented in figure 5.5.

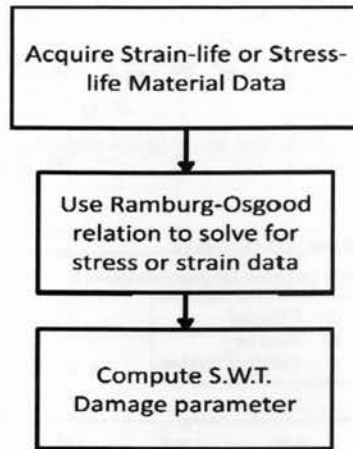


Figure 5.5: S.W.T. damage assessment methodological flowchart.

5.3.1.1. Al 6061 / Al₂O₃ / 20p-T6

The strain-life data for this material was reported in reference [56]. Reported data included fatigue tests for pure tension, torsion, and combined tension-torsion. These data are presented in Appendix A (Tables A2-1 through A2-5). S.W.T damage approach was employed to assess fatigue damage of components tested under tension, torsion, and combined tension-torsion. Results of S.W.T. damage parameter versus fatigue life cycles for Al 6061 / Al₂O₃ / 20p-T6 is presented in figure 5.6.

5.3.1.2. Al 6061 / Al₂O₃ / 22p-T6

The strain-life data [57] were reported for this material under various loading conditions of tension, torsion, and combined in-phase tension-torsion. These data are listed in Appendix A (Tables A2-6 through A2-8). Figure 5.7 presents S.W.T damage parameter collapsing all fatigue tests data in a narrow band for various fatigue lives.

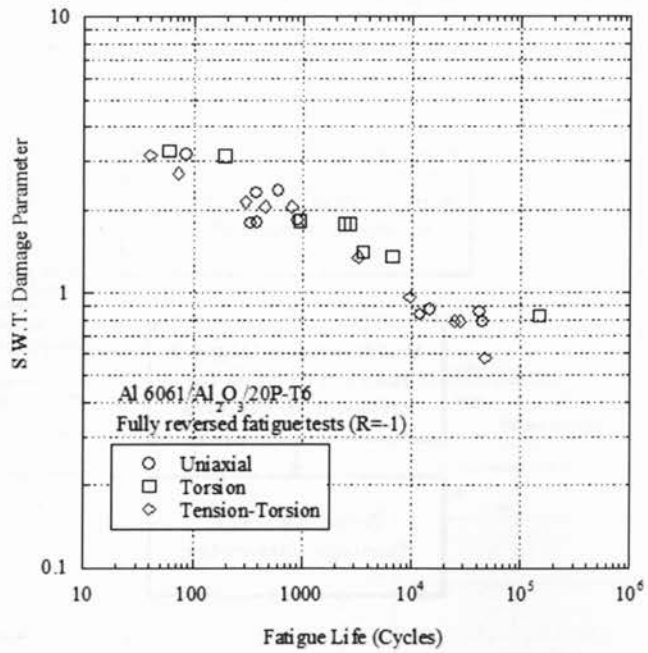


Figure 5.6: The S.W.T. damage parameter versus fatigue lives for Al 6061 / Al₂O₃ / 20p-T6.

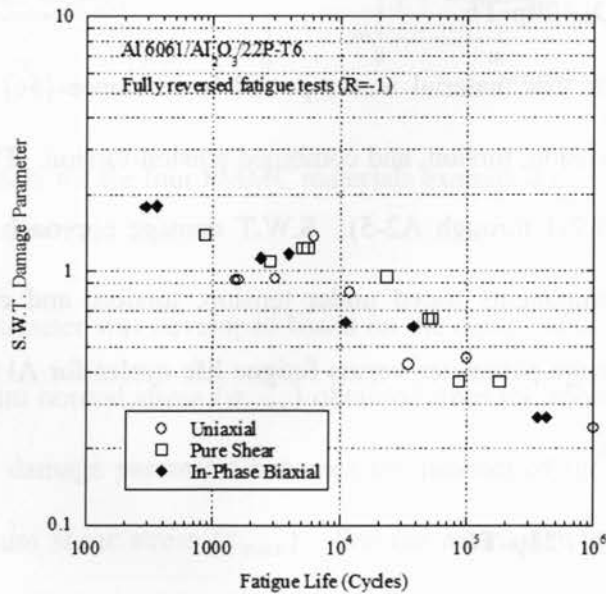


Figure 5.7: S.W.T. damage parameter versus fatigue lives for Al 6061 / Al₂O₃ / 22p-T6.

5.3.1.3. Al 6061 / SiC / 17w-T6

This material has been fatigue tested under five different loading conditions [45] of $\lambda = \tau_{max}/\sigma_{max}$ at 0 (pure tension), ∞ (pure shear), and 0.5, 1, and 2 (in-phase biaxial). These data are listed in Appendix A (Tables A2-9 - A2-13). S.W.T damage parameter versus fatigue lives for tension, torsion, and combined tension-torsion is presented in figure 5.8.

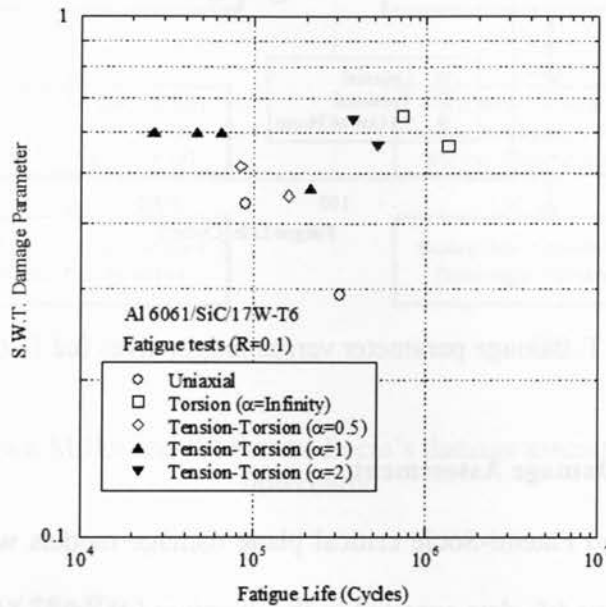


Figure 5.8: S.W.T. damage parameter versus fatigue lives for Al 6061 / SiC / 17w-T6.

5.3.1.4. Ti-6Al-4V / TiC / 10p

Strain-life data for this material were reported [58] for three tests of uniaxial tension (shaft), pure torsion (tube), and multiaxial 90° out-of-phase loading (tube). Strain-life data and calculated S.W.T. damage values are presented in Appendix A (Tables (A-14) – (A-16)). Figure 5.9 presents S.W.T. results versus fatigue lives of components.

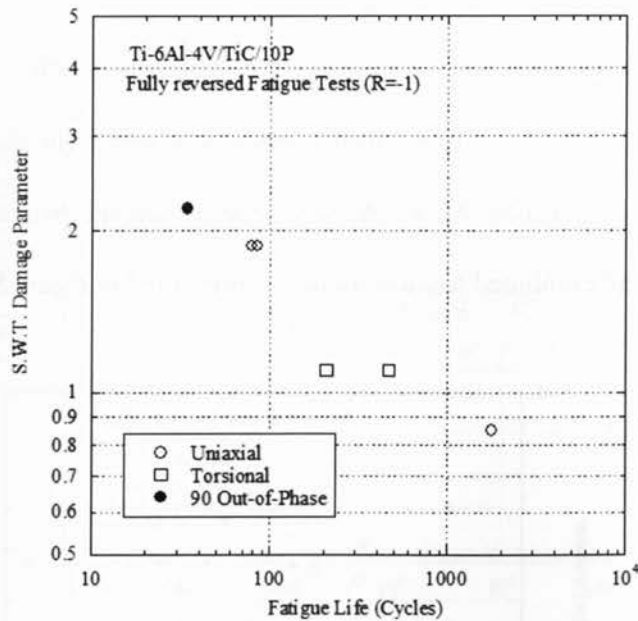


Figure 5.9: S.W.T. damage parameter versus fatigue lives for Ti-6Al-4V / TiC / 10p.

5.3.2. Critical Plane Damage Assessment

Both Brown-Miller and Fatemi-Socie critical plane damage models were evaluated using four sets of multiaxial fatigue life data reported in the literature [45,56,57,58]. Recall that the critical plane damage model is based on physics of material damage along the crystallographic planes where the maximum resolved shear stress is achieved. For damage assessment based on Fatemi-Socie critical plane model, the maximum shear stress and its corresponding maximum normal stress on the maximum shear plane are required. For Brown-Miller's approach, both the normal and shear strain components acting on the critical plane should be calculated first. Equations (4.2) and (4.3) respectively represent Brown-Miller and Fatemi-Socie approaches.

The procedure of damage analysis based on both Brown-Miller and Fatemi-Socie critical plane damage approaches are presented in a flowchart shown in figure 5.10.

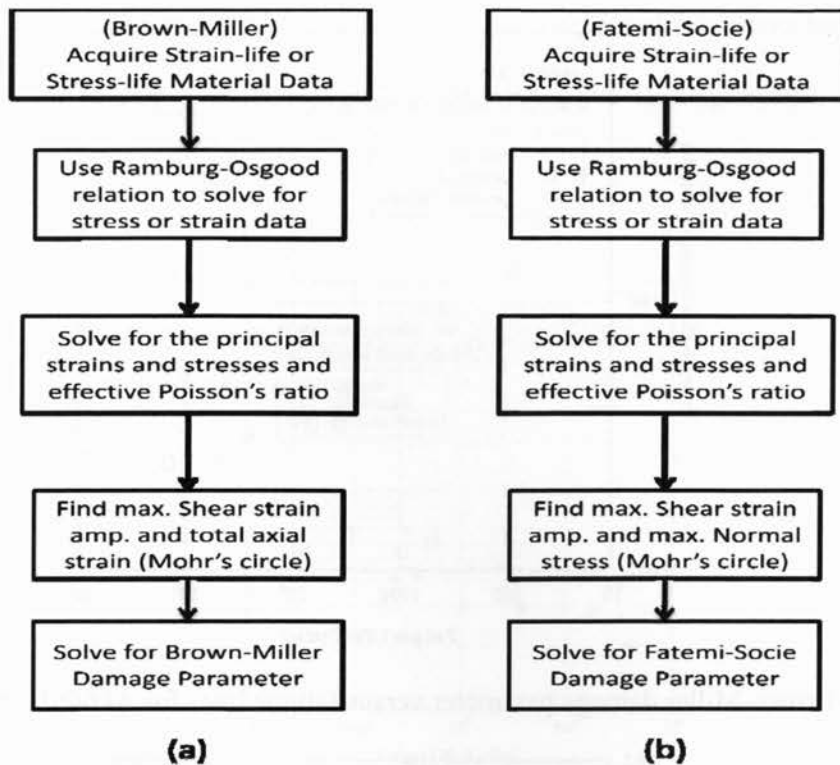


Figure 5.10: (a) Brown-Miller and (b) Fatemi-Socie's damage assessment methodological flowcharts.

5.3.2.1. Al 6061 / Al₂O₃ / 20p-T6

Brown-Miller and Fatemi-Socie critical plane approaches were used to assess fatigue damage of Al 6061 / Al₂O₃ / 20p-T6 components under various fatigue loading conditions of axial, torsion and combined axial-torsion. Results of damage analysis based on critical plane approaches are listed in Tables (A3-1) – (A3-5). Figure 5.11 and 5.12 respectively represent Brown-Miller and Fatemi-Socie damage parameters versus fatigue lives for various loading conditions. Note that the constants used for Brown-Miller and Fatemi-Socie are respectively reported in literature as 0.34 and 0.6.

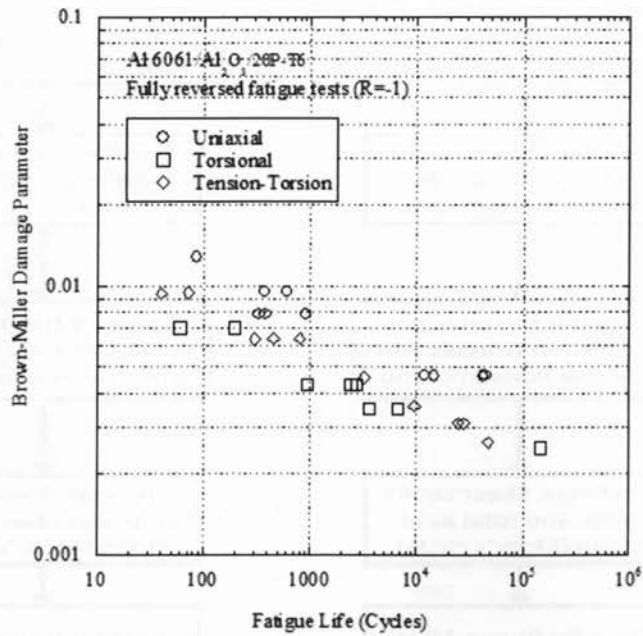


Figure 5.11: Brown-Miller damage parameter versus fatigue lives for Al 6061 / Al₂O₃ / 20p-T6.

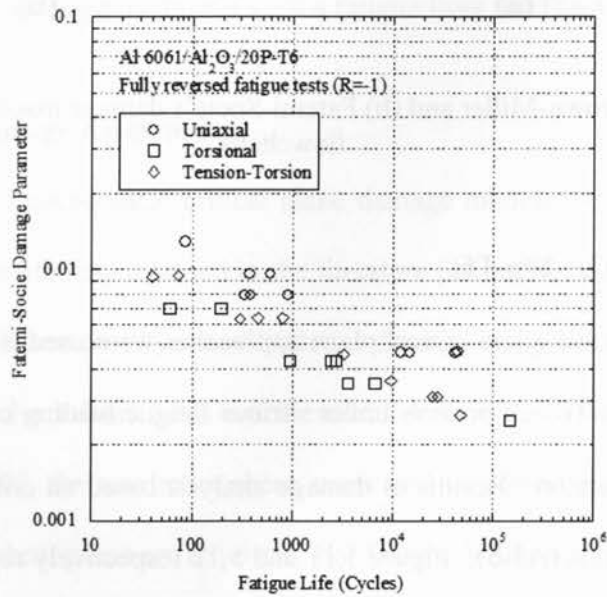


Figure 5.12: Fatemi-Socie damage parameter versus fatigue lives for Al 6061 / Al₂O₃ / 20p-T6.

5.3.2.2. Al 6061 / Al₂O₃ / 22p-T6

Brown-Miller and Fatemi-Socie damage parameters assessed fatigue life data of Al 6061/ Al₂O₃ / 22p-T6 under axial, torsion, and biaxial loading conditions. Results of damage assessment are

presented in Appendix A (Tables (A3-6)-(A3-8)). Figures 5.13 and 5.14 show how critical plane damage approaches collapse fatigue damage data of various loading conditions in a single diagram.

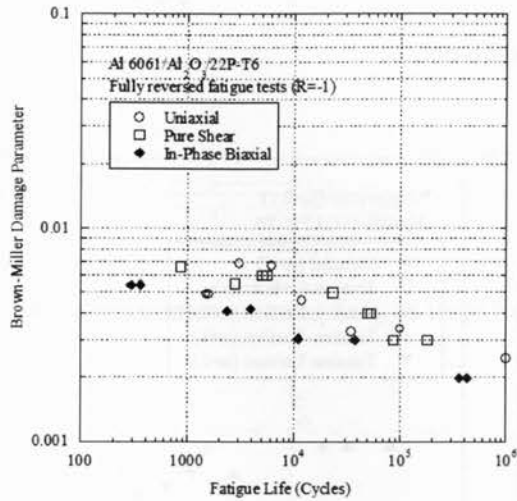


Figure 5.13: Brown-Miller damage parameter versus fatigue lives for Al 6061 / Al₂O₃ / 22p-T6.

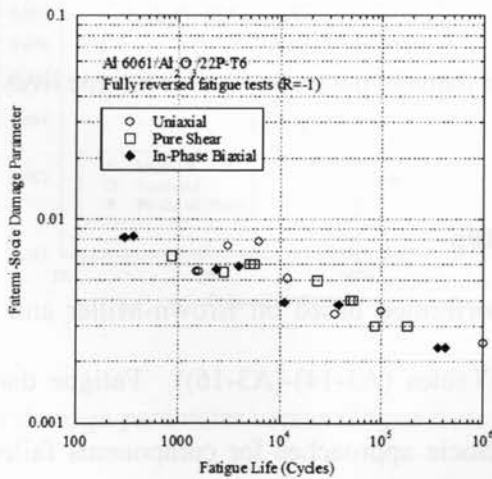


Figure 5.14: Fatemi-Socie damage parameter versus fatigue lives for Al 6061 / Al₂O₃ / 22p-T6.

5.4.2.3. Al 6061 / SiC / 17w-T6

Critical plane damage parameters evaluated fatigue data tested under various uniaxial, torsion, and biaxial loading conditions. Analysis are tabulated in Appendix A (Tables (A3-9)-(A3-13)). The results of Brown-Miller and Fatemi-Socie damage versus fatigue life data are presented in figures 5.15 and 5.16 respectively.

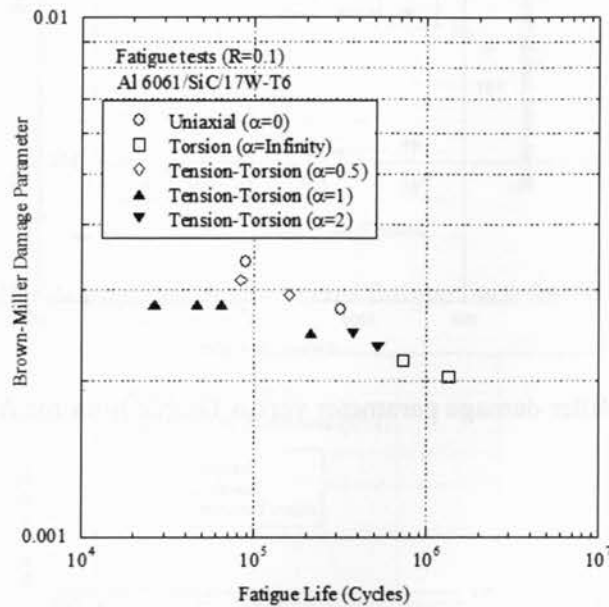


Figure 5.15: Brown-Miller damage parameter versus fatigue lives for Al 6061 / SiC / 17w-T6.

5.3.2.4. Ti-6Al-4V / TiC / 10p

Fatigue damage analysis performed based on Brown-Miller and Fatemi-Socie approaches are tabulated in Appendix A (Tables (A3-14)-(A3-16)). Fatigue damage results calculated using Brown-Miller and Fatemi-Socie approaches for components failed under uniaxial, torsion and biaxial loading conditions are plotted in figures 5.17 and 5.18.

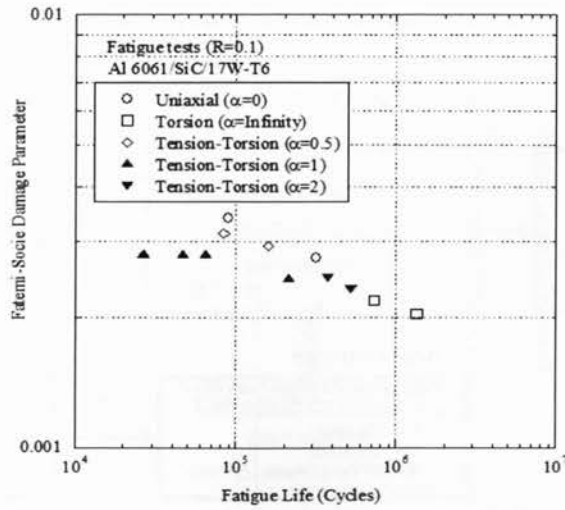


Figure 5.16: Fatemi-Socie damage parameter versus fatigue lives for Al 6061 / SiC / 17w-T6.

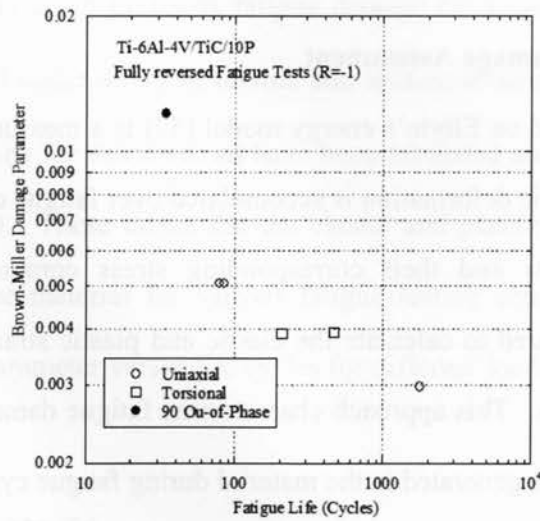


Figure 5.17: Brown-Miller damage parameter versus fatigue lives for Ti-6Al-4V / TiC / 10p.

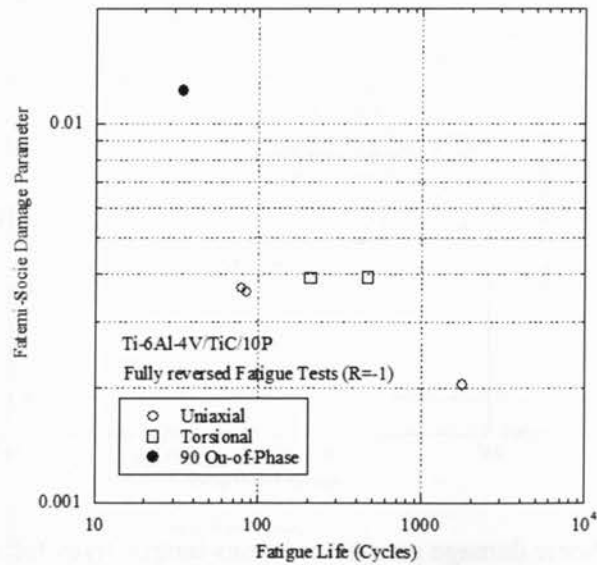


Figure 5.18: Fatemi-Socie damage parameter versus fatigue lives for Ti-6Al-4V / TiC / 10p.

5.3.3. Ellyin's Energy Damage Assessment

Damage assessment based on Ellyin's energy model [57] is a measure of materials damage in a component as cyclic plastic deformation is accumulated over fatigue cycles. Both the plastic and elastic strain components and their corresponding stress components of the stress-strain hysteresis loops are required to calculate the elastic and plastic strain energies for the material subjected to fatigue loads. This approach characterizes fatigue damage based on the integrated elastic and plastic energies generated in the material during fatigue cycles.

The procedure of damage analysis based on Ellyin's energy parameter is outlined in figure 5.19.

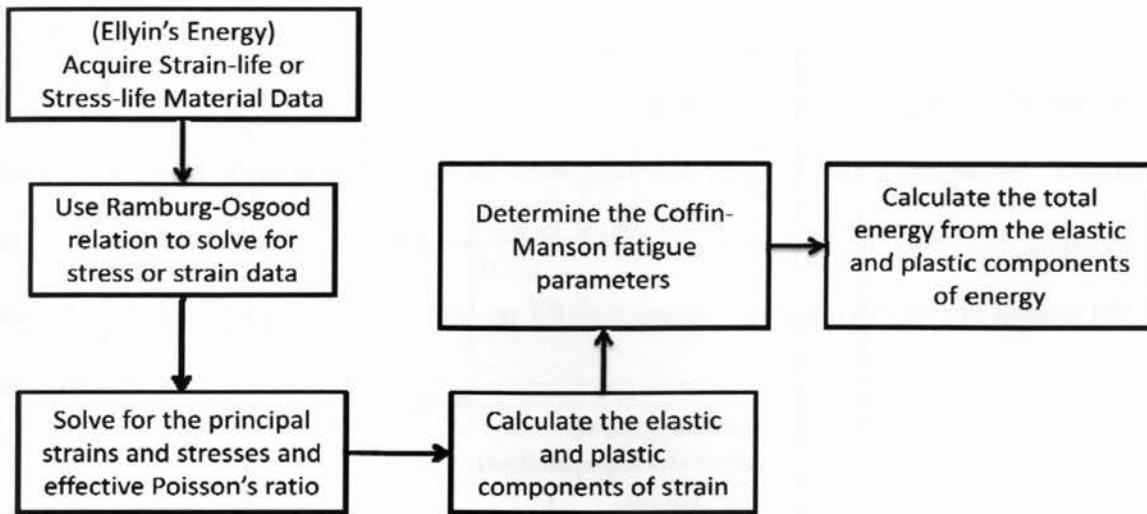


Figure 5.19: Ellyin's Energy damage assessments methodological flowchart.

5.3.3.1. Al 6061 / Al₂O₃ / 20p-T6

Ellyin's approach was employed to assess fatigue damage of components made of Al 6061 / Al₂O₃ / 20p-T6 and tested under uniaxial, torsion and tension-torsion cyclic loading conditions. The damage analysis results for this material have been tabulated and presented in Appendix A (Tables (A4-1) – (A4-3)). These tables list the elastic and plastic strains and the calculated energy components of the material for various fatigue testing conditions. Figure 5.20 plots Ellyin's energy damage parameter versus life cycles for different loading conditions.

5.3.3.2. Al 6061 / Al₂O₃ / 22p-T6

Fatigue damage of Al 6061/ Al₂O₃ / 22p-T6 components tested under uniaxial, torsional and biaxial loading conditions were evaluated by Ellyin's energy approach. The results of Ellyin's parameter are plotted versus fatigue lives in figure 5.21. These results have been tabulated in Tables (A4-4) – (A4-6).

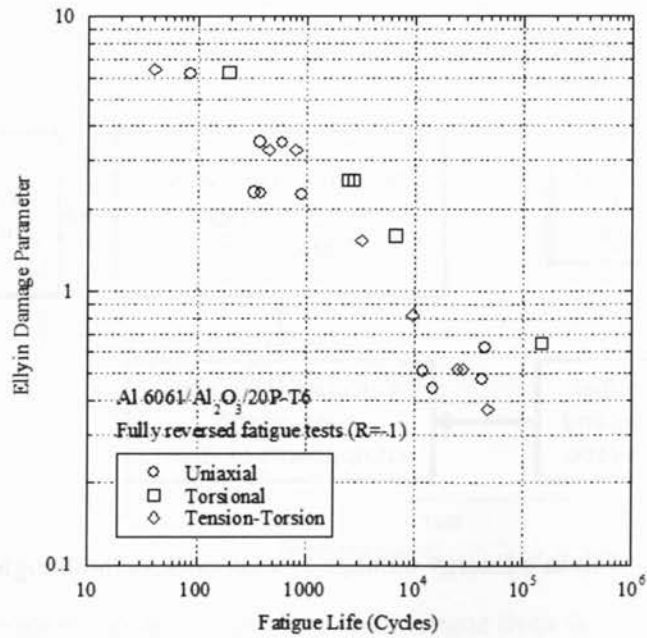


Figure 5.20: Ellyin energy damage parameter versus fatigue lives for Al 6061 / Al₂O₃ / 20p-T6.

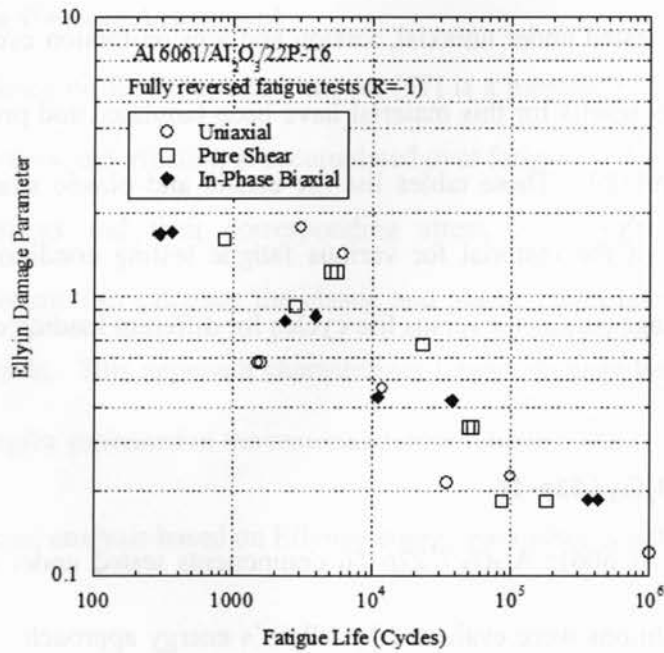


Figure 5.21: Ellyin energy damage parameter versus fatigue lives for Al 6061 / Al₂O₃ / 22p-T6.

5.3.3.3. Al 6061 / SiC / 17w-T6

The energy damage model was employed to assess damage of Al 6061 / SiC / 17w-T6 fatigue tested under uniaxial, shear and combined tension-torsion fatigue loading conditions. Results of analysis were tabulated in Appendix A (Tables (A4-7) – (A4-11)). Figure 5.22 displays the calculated fatigue damage values based on Ellyin's energy approach versus the fatigue life for this material.

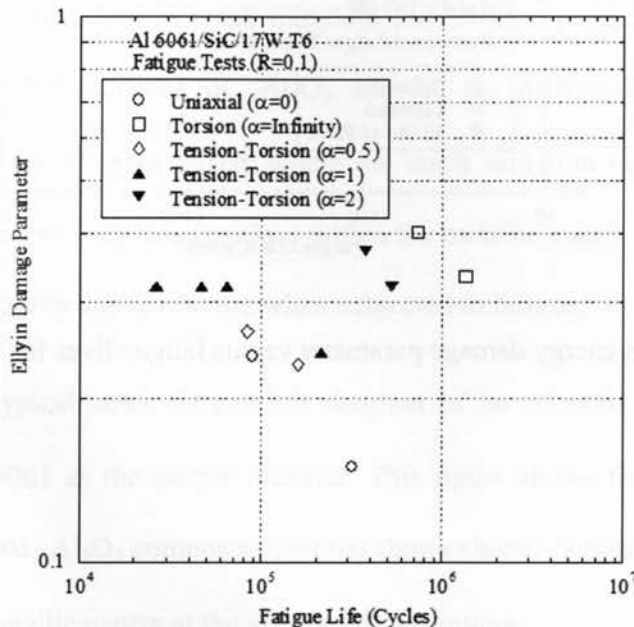


Figure 5.22: Ellyin energy damage parameter versus fatigue lives for Al 6061 / SiC / 17w-T6 Energy.

5.3.3.4. Ti-6Al-4V / TiC / 10p

Ellyin energy model was evaluated based on fatigue tests results conducted under uniaxial, shear and 90° out-of-phase combined tension-torsion loading conditions. Stress, Strain and energy

components are presented in Appendix A (Tables (A4-12)-(A4-14)). The results of energy parameter versus fatigue lives are plotted in figure 5.23.

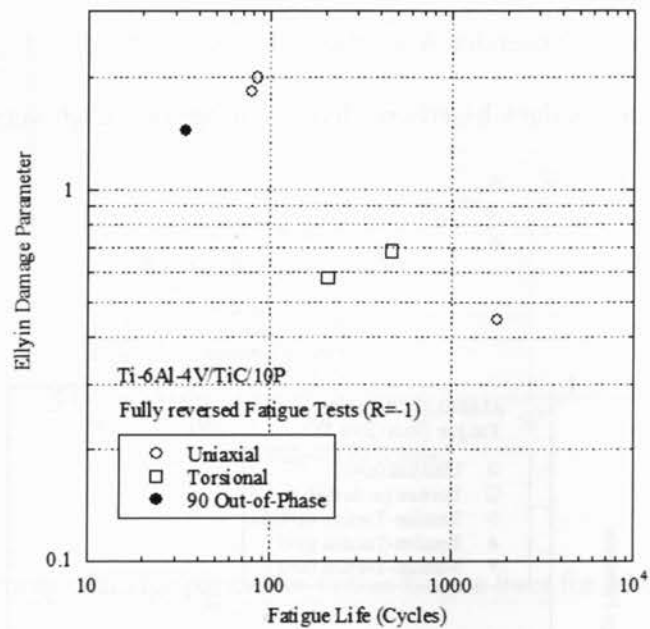


Figure 5.23: Ellyin energy damage parameter versus fatigue lives for Ti-6Al-4V / TiC / 10p.

Chapter 6

Fatigue Model for PMMC Developed Based on Critical Plane-Energy

Approach

6.1. Strain-Life in PMMCs

It is well documented that PMMCs show lowered fatigue strength than the base metallic matrices [59,60,61]. Reinforced particles are prone to an early fracture when metal matrix composites experience cyclic stress, resulting in crack initiation and damage progress within the metallic matrix. Brittle reinforced particles of SiC, Al₂O₃, and TiC are intermetallic materials dispersed within the matrix and act as stress raisers where the crack initiation most likely takes place. Distributed particles occupy countless positions within the metallic matrix leading degradation of composite materials integrity against failure when subjected to fatigue.

Figure 6.1 compares typical strain-fatigue life diagram of an Al 6061 / Al₂O₃ / 20p PMM composite and an Al 6061 as the matrix material. This figure shows that at any given cyclic strain magnitude, Al 6061- Al₂O₃ composite material shows shorter fatigue life as compared with the fatigue life of the metallic matrix at the same strain magnitude.

6.2. Coffin-Manson Relation for PMMCs

The Coffin-Manson relation has been employed to evaluate fatigue life of metal-matrix composites through extensive studies by [63,64,65]. Coffin-Manson equation characterizes fatigue life ($2N_f$) of components based on the cyclic elastic strain ($\Delta\varepsilon_e/2$) and the plastic strain

$(\Delta\varepsilon_p/2)$ and material properties ($\sigma'_f, E, \varepsilon'_f, b, \text{ and } c$). Traditional Coffin-Manson equation for metallic materials is expressed as:

$$\frac{\Delta\varepsilon}{2} = \frac{\Delta\varepsilon_e}{2} + \frac{\Delta\varepsilon_p}{2} = \frac{\sigma'_f}{E} (2N_f)^b + \varepsilon'_f (2N_f)^c \quad (6.1)$$

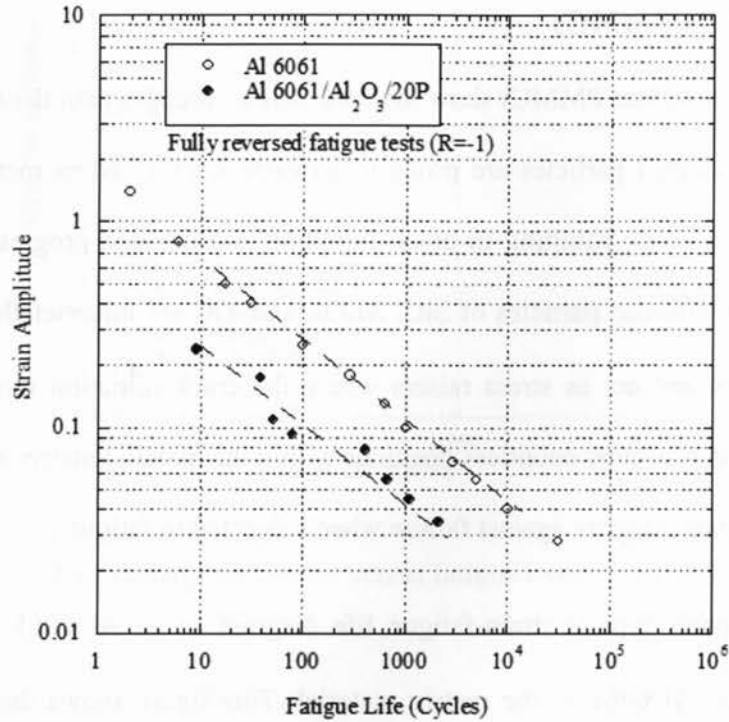


Figure 6.1: Comparison of Strain-Fatigue Life of Al 6061 and Al 6061 / Al₂O₃ / 20p [62].

For particle reinforced metal matrix composites, Coffin-Manson is similarly expressed as:

$$\left(\frac{\Delta\varepsilon}{2}\right)_c = \left(\frac{\sigma'_f}{E}\right)_c (2N_f)^b + (\varepsilon'_f)_c (2N_f)^c \quad (6.1-1)$$

where the subscript c corresponds to the PMM composite.

Figure 6.2 presents strain-life diagrams for both a PMM composite and a metal matrix.

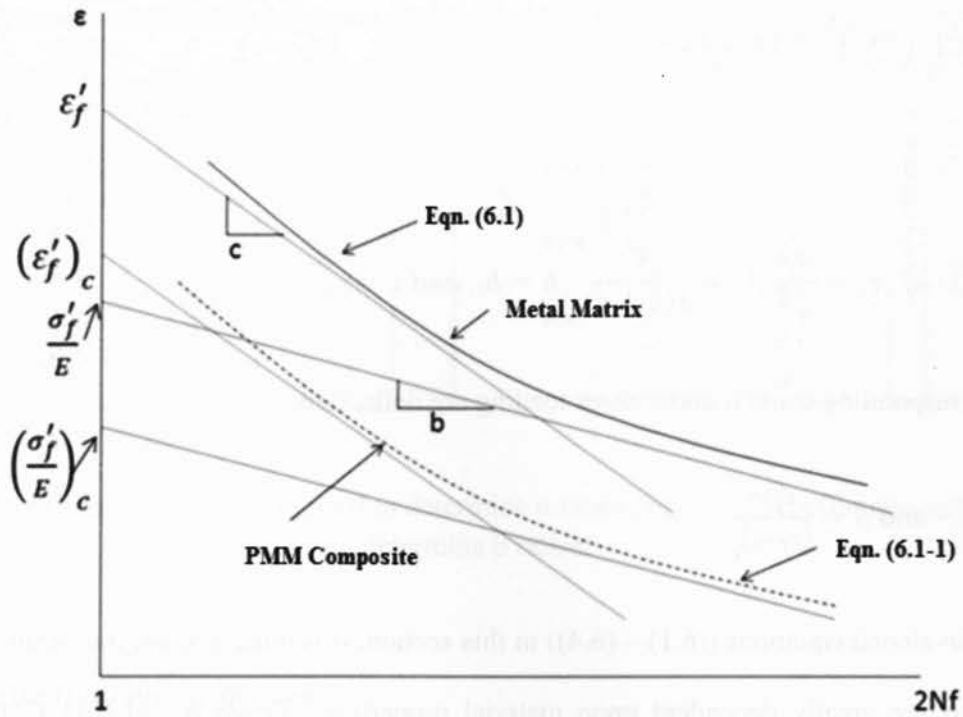


Figure 6.2: Schematic strain-life diagram of metal matrix and PMM composite.

Assuming exponent's b and c are identical for the PMM composite and the metal matrix, a comparison of strain-life diagrams in figure 6.2 leads to establish:

$$\alpha = \frac{\epsilon'_f}{(\epsilon'_f)_c} \text{ and } \beta = \frac{\sigma'_f/E}{(\sigma'_f/E)_c} \quad (6.2)$$

Similarly Coffin-Manson relation for pure shear loading for a metallic matrix and a PMM composites are given respectively as:

$$\frac{\Delta\gamma}{2} = \frac{\tau'_f}{G} (2N_f)^{b_s} + \gamma'_f (2N_f)^{c_s} \quad (6.3)$$

and

$$\frac{\Delta\gamma}{2} = \left(\frac{\tau'_f}{G}\right)_c (2N_f)^{b_s} + (\gamma'_f)_c (2N_f)^{c_s} \quad (6.3-1)$$

where,

$$\gamma'_f = \sqrt{3} \cdot \varepsilon'_f, \tau'_f = \frac{\sigma'_f}{\sqrt{3}}, G = \frac{E}{2(1+\nu)}, b = b_s, \text{ and } c = c_s$$

The corresponding α and β under shear loading are defined as:

$$\alpha = \frac{\gamma'_f}{(\gamma'_f)_c} \text{ and } \beta = \frac{\tau'_f/G}{(\tau'_f/G)_c} \quad (6.4)$$

From developed equations ((6.1) – (6.4)) in this section, it is quite evident that strain-fatigue life diagrams are greatly dependent upon material properties. Terms α and β in Coffin-Manson equations ((6.1) and (6.3)) correspond to the ratios of material properties in the metallic matrix and the PMM composite.

6.3. Results of α and β for Various PMM Composites

The elastic and the plastic materials coefficients (ε'_f) and (σ'_f/E) for both PMMCs and base metal alloys used in this thesis are displayed as bar graph in figures 6.3 a-b. These values are used to determine terms α and β in the critical plane-energy approach.

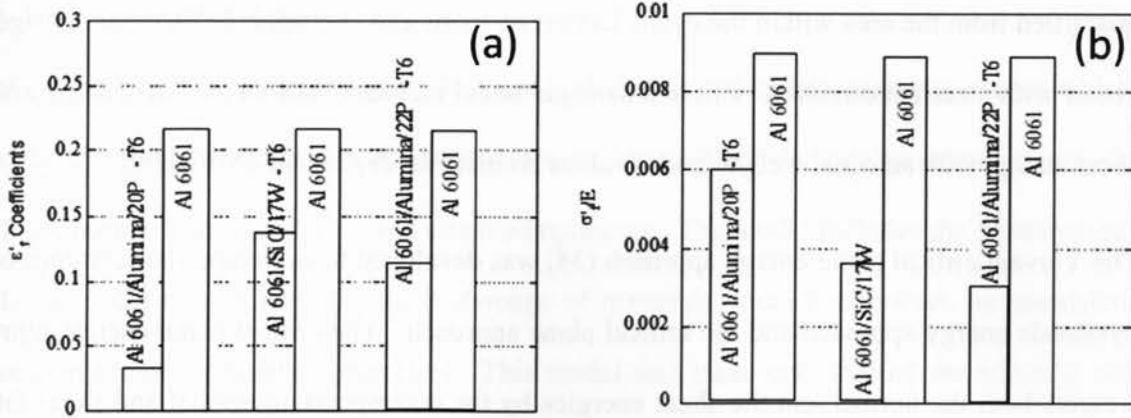


Figure 6.3: (a) ϵ'_f coefficients used to determine α ratios (b) (σ'_f/E) coefficients used to determine β ratios.

6.4. Fatigue Damage Approach

Degradation of fatigue strength in PMM composites is very much due to reinforcement material, debonding of particle-matrix interface, and early fracture of brittle particles under cyclic loads. This highlights the necessity of material constants in fatigue damage approaches.

Damage approaches of S.W.T., Brown-Miller and Fatemi-Socie lack a full involvement of material coefficients or constants and the coefficients of these approaches are not determined readily. Brown-Miller and Fatemi-Socie approaches are defined either in terms of stress components or strain components acting on the critical plane, and fail to present a rigorous model based on fundamentals of continuum mechanics.

Smith-Watson-Topper (S.W.T.) and Ellyin Energy approaches however contribute both stress and strain components in damage assessment of materials. S.W.T. calculates the amount of energy during loading on the maximum shear plane while Ellyin's energy approach calculates energy from the cyclic stress-strain hysteresis loop during each fatigue cycle. Ellyin's energy is

quantified from the area within the cyclic hysteresis loops and excludes the fact that damage is a vector with a certain direction. Ellyin's damage model includes both the normal energy and the shear energy with an equal weight, and involves no material dependent coefficients.

The Varvani critical plane-energy approach [38] was developed to overcome shortcomings of the hysteresis energy approach and the critical plane approach. The critical plane-energy approach weights both the normal and the shear energies by the corresponding normal and shear fatigue properties. Components of the normal and shear energies on this model are calculated from stresses and strains acting on the critical plane of maximum shear stress.

For metallic materials, Varvani's approach [38] is expressed as:

$$V = \frac{\Delta\varepsilon_n \cdot \Delta\sigma_n}{\varepsilon_f' \cdot \sigma_f'} + \frac{\frac{\Delta\gamma_{max}}{2} \cdot \Delta\tau_{max}}{\gamma_f' \cdot \tau_f'} \quad (6.5)$$

Equation (6.5) due to its broadness and inclusion of the normal and shear stress/strain components and more importantly weighting the normal and shear energies respectively with the normal and shear fatigue properties is qualified for damage assessment of PMM composites.

The equation (6.6) for damage assessment of PMM composite is extended as:

$$V_c = \frac{\Delta\varepsilon_n \cdot \Delta\sigma_n}{\frac{\varepsilon_f'}{\alpha} \cdot \frac{\sigma_f'}{\beta}} + \frac{\frac{\Delta\gamma_{max}}{2} \cdot \Delta\tau_{max}}{\frac{\gamma_f'}{\alpha} \cdot \frac{\tau_f'}{\beta}}$$

$$V_c = \alpha \cdot \beta \left[\frac{\Delta\varepsilon_n \cdot \Delta\sigma_n}{\varepsilon_f' \cdot \sigma_f'} + \frac{\frac{\Delta\gamma_{max}}{2} \cdot \Delta\tau_{max}}{\gamma_f' \cdot \tau_f'} \right] \quad (6.6)$$

6.5. Damage Assessment

Varvani critical plane-energy model integrates both the normal and shear energy ranges which is calculated directly from the critical plane. Varvani critical-plane damage parameter incorporates both the normal and shear stress and strain components. The model includes the contribution of both shear and normal components in damage of materials under cyclic loads by normalizing them using material fatigue parameters. This model also takes into account the effect of mean stress and includes the effect of strain-hardening for out-of-phase loading conditions.

The procedure of damage assessment based on Varvani's critical approach is outlined in figure 6.4.

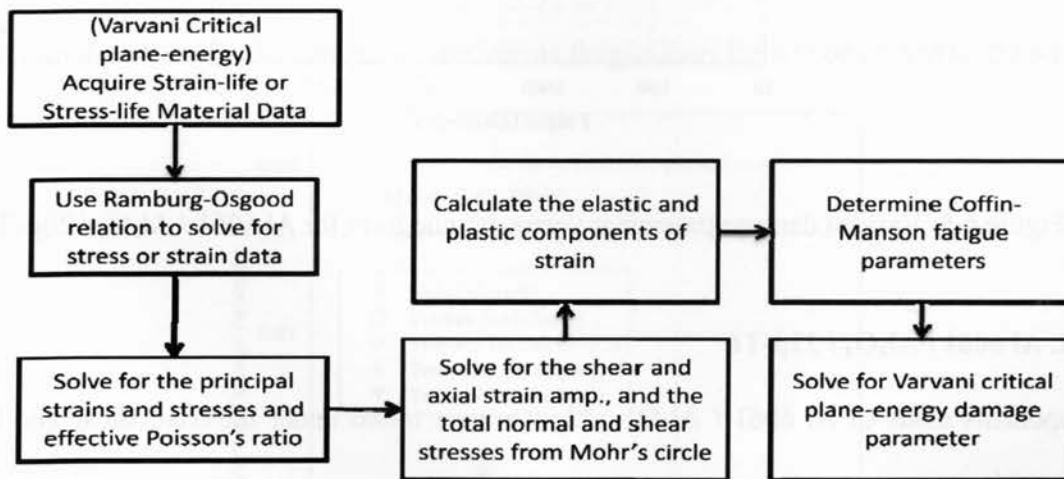


Figure 6.4: Varvani Critical Plane-Energy damage assessment methodological flowchart.

6.5.1. Al 6061 / Al₂O₃ / 20p-T6

Varvani damage approach was utilized to assess damage of Al 6061 / Al₂O₃ / 20p-T6 components tested under various loading conditions. Figure 6.5 shows how Varvani's damage

model collapse fatigue data of various loading in a narrow band. The results of damage assessment based on this model are tabulated in Tables (A5-1) – (A5-3).

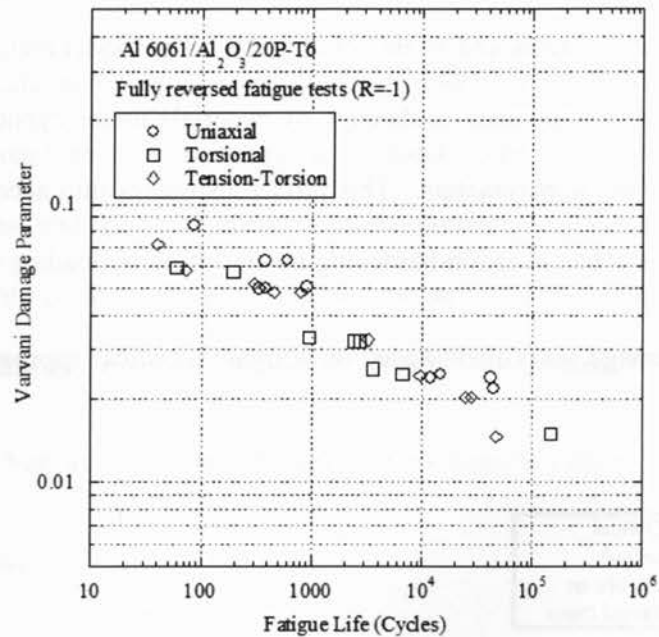


Figure 6.5: Varvani damage parameter versus fatigue lives for Al 6061 / Al₂O₃ / 20p-T6.

6.5.2. Al 6061 / Al₂O₃ / 22p-T6

Components made of Al 6061 / Al₂O₃ / 22p-T6 were tested under uniaxial, shear and biaxial loading conditions [24]. Fatigue data then were evaluated using Varvani's approach and presented in Figure 6.6. Results of analysis are tabulated in Tables (A5-4) – (A5-6).

6.5.3. Al 6061 / SiC / 17w-T6

Fatigue test data [45] performed under uniaxial, torsion and various tension-torsion fatigue loading conditions were evaluated using Varvani's approach and were plotted versus fatigue lives in figure 6.7. Results of damage analysis are presented in Tables (A5-7) – (A5-11).

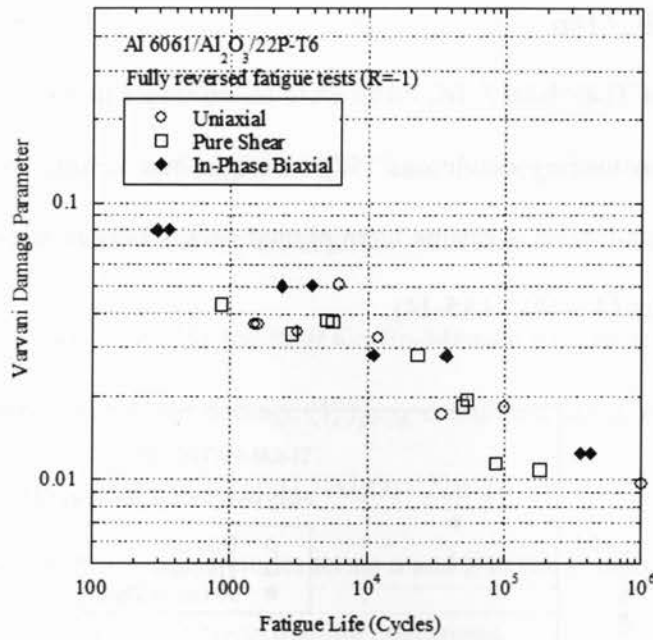


Figure 6.6: Varvani damage parameter versus fatigue lives for Al 6061 / Al₂O₃ / 22p-T6.

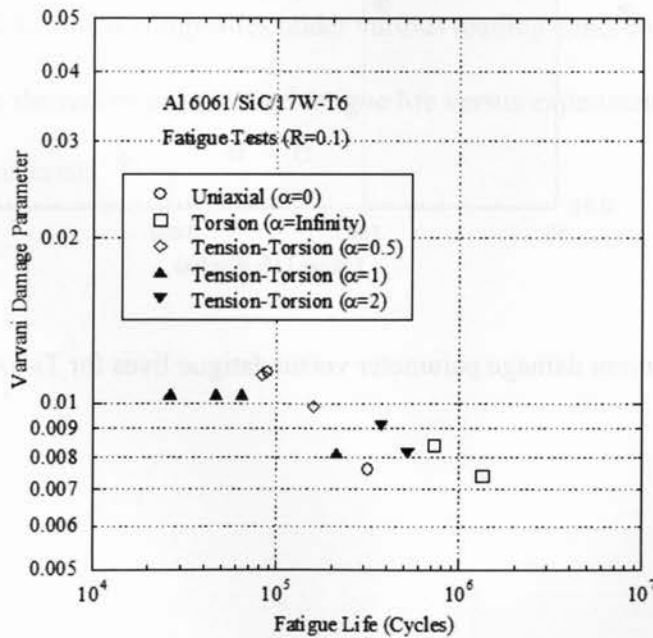


Figure 6.7: Varvani damage parameter versus fatigue lives for Al 6061 / SiC / 17w-T6.

6.5.4. Ti-6Al-4V / TiC / 10p

Components made of Ti-6Al-4V / TiC / 10p were tested under uniaxial, torsion and 90° out-of-phase tension torsion loading conditions [58]. Fatigue test results were evaluated based on Varvani's approach and damage results were plotted versus fatigue lives in figure 6.8. Results are tabulated in Tables (A5-12) – (A5-14).

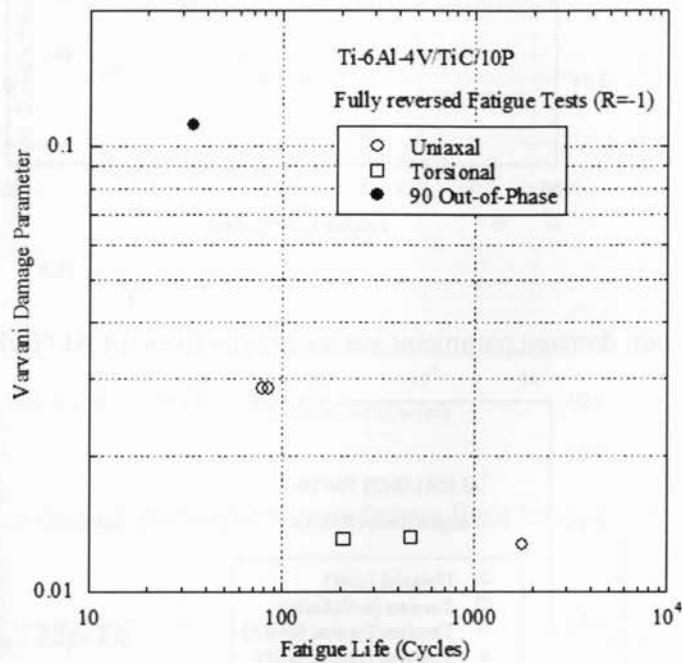


Figure 6.8: Varvani damage parameter versus fatigue lives for Ti-6Al-4V / TiC / 10p.

6.6. Life Prediction Results

Varvani damage approach was extended to characterize the damage of Al 6061 / Al₂O₃ / 20p-T6, Al 6061 / Al₂O₃ / 22p-T6 and Al 6061 / SiC / 17w-T6 composites when terms α and β and the strain-life Coffin-Manson coefficients for the metallic matrix are available.

The strain-life data of Al 6061-T6 [75] and their Coffin-Manson parameters are listed in Appendix A. The results of predicted damage $(V_c)_{pred.}$ calculated based on experimental results $(V_c)_{exp.}$ for Al 6061 / Al₂O₃ / 20p-T6, Al 6061 / Al₂O₃ / 22p-T6 and Al 6061 / SiC / 17w-T6 are tabulated in Table 6.9. Table 6.9 also includes terms α and β of the composite materials tested in tension, torsion, and tension-torsion fatigue loading conditions.

The results of predicted damage $(V_c)_{pred.}$ are in good agreement with the experimental damage $(V_c)_{exp.}$ data collected for PMM composites under various loading conditions. Figure 6.9 presents and compares the results of predicted fatigue life versus experimental fatigue life data for PMM composite materials

Table 6.1: Comparison of calculated damage values V (Eqn (6.5)) based on experimental fatigue data with fatigue damage data predicted using terms α and β and equation (6.6).

| Al 6061/Al ₂ O ₃ /20p-T6 | | | | | | | | | | | |
|--|---------|------------|--------------------------|---|-----------|------------|--------------------------|--|---------|------------|--------------------------|
| Tension ($\alpha=1.8, \beta=7.33$) | | | | Torsion ($\alpha=2, \beta=4$) | | | | Tension-Torsion ($\alpha=1.2, \beta=6$) | | | |
| ϵ (%) | Life | V (Exp) | V _c (Pre.) | γ (%) | Life | V (Exp) | V _c (Pre.) | ϵ/γ (%) | Life | V (Exp) | V _c (Pre.) |
| 0.8 | 85 | 0.085 | 0.065 | 1.4 | 60 | 0.059 | 0.082 | 0.58/1 | 40 | 0.072 | 0.086 |
| 0.6 | 599 | 0.063 | 0.047 | 1.4 | 195 | 0.057 | 0.078 | 0.4/0.7 | 800 | 0.048 | 0.058 |
| 0.6 | 376 | 0.063 | 0.047 | 0.86 | 937 | 0.033 | 0.046 | 0.4/0.7 | 452 | 0.048 | 0.058 |
| 0.5 | 331 | 0.050 | 0.038 | 0.86 | 2,423 | 0.032 | 0.044 | 0.29/0.5 | 3,234 | 0.033 | 0.040 |
| 0.5 | 379 | 0.050 | 0.038 | 0.86 | 2,735 | 0.032 | 0.044 | 0.29/0.5 | 3,233 | 0.033 | 0.040 |
| 0.5 | 909 | 0.050 | 0.038 | 0.70 | 3,601 | 0.026 | 0.035 | 0.23/0.4 | 9,597 | 0.024 | 0.029 |
| 0.3 | 14,712 | 0.025 | 0.017 | 0.70 | 6,19 | 0.025 | 0.034 | 0.2/0.35 | 27,433 | 0.020 | 0.025 |
| 0.3 | 11,886 | 0.024 | 0.017 | 0.50 | 146,788 | 0.015 | 0.021 | 0.2/0.35 | 24,754 | 0.020 | 0.025 |
| 0.3 | 44,640 | 0.022 | 0.016 | | | | | 0.17/0.3 | 47,000 | 0.015 | 0.018 |
| 0.3 | 42,245 | 0.024 | 0.016 | | | | | | | | |
| Al 6061/Al ₂ O ₃ /22p-T6 | | | | | | | | | | | |
| Tension ($\alpha=2, \beta=3.33$) | | | | Torsion ($\alpha=1.65, \beta=4$) | | | | Tension-Torsion ($\alpha=1.32, \beta=5$) | | | |
| ϵ (%) | Life | V (Exp) | V _c (Pre.) | γ (%) | Life | V (Exp) | V _c (Pre.) | ϵ/γ (%) | Life | V (Exp) | V _c (Pre.) |
| 0.3 | 1,574 | 0.037 | 0.038 | 0.2 | 53,475 | 0.019 | 0.022 | 0.2/0.2 | 2,325 | 0.05 | 0.052 |
| 0.2 | 35,000 | 0.017 | 0.018 | 0.25 | 23,053 | 0.028 | 0.032 | .25/.25 | 357 | 0.080 | 0.083 |
| 0.3 | 1,472 | 0.037 | 0.038 | 0.15 | 86,551 | 0.011 | 0.013 | .15/.15 | 10,911 | 0.028 | 0.029 |
| 0.15 | 999,033 | 0.010 | 0.010 | 0.3 | 5,013 | 0.038 | 0.042 | .1/.1 | 358,912 | 0.012 | 0.013 |
| 0.395 | 6,154 | 0.051 | 0.054 | 0.275 | 2,786 | 0.034 | 0.038 | .25/.25 | 291 | 0.080 | 0.083 |
| 0.206 | 99,001 | 0.018 | 0.019 | 0.33 | 855 | 0.043 | 0.049 | .2/.2 | 3,940 | 0.051 | 0.053 |
| 0.405 | 3,029 | 0.035 | 0.037 | 0.15 | 178,295 | 0.011 | 0.012 | .15/.15 | 37,645 | 0.028 | 0.030 |
| 0.281 | 11,882 | 0.033 | 0.035 | 0.2 | 49,178 | 0.018 | 0.021 | .1/.1 | 426,542 | 0.012 | 0.013 |
| | | | | 0.3 | 5,542 | 0.037 | 0.042 | | | | |
| Al 6061/SiC/17w | | | | | | | | | | | |
| Tension ($\alpha=1.5, \beta=2.54$) | | | | Torsion ($\alpha=1.9, \beta=1.96$) | | | | Tension-Torsion ($\alpha=1.7, \beta=2.2$) | | | |
| ϵ (%) | Life | V (Exp) | V _c (Pre.) | γ (%) | Life | V (Exp) | V _c (Pr) | ϵ/γ (%) | Life | V (Ex) | V _c (Pre.) |
| 0.22 | 88,756 | 0.011 | 0.016 | 0.44 | 733,899 | 0.008 | 0.005 | .1/3 | 26,292 | 0.01 | 0.01 |
| 0.18 | 314,730 | 0.008 | 0.011 | 0.41 | 1,338,899 | 0.007 | 0.004 | .1/3 | 46,477 | 0.01 | 0.01 |
| | | | | | | | | .1/3 | 64,519 | 0.01 | 0.01 |
| | | | | | | | | .12/3 | 212,321 | 0.008 | 0.008 |

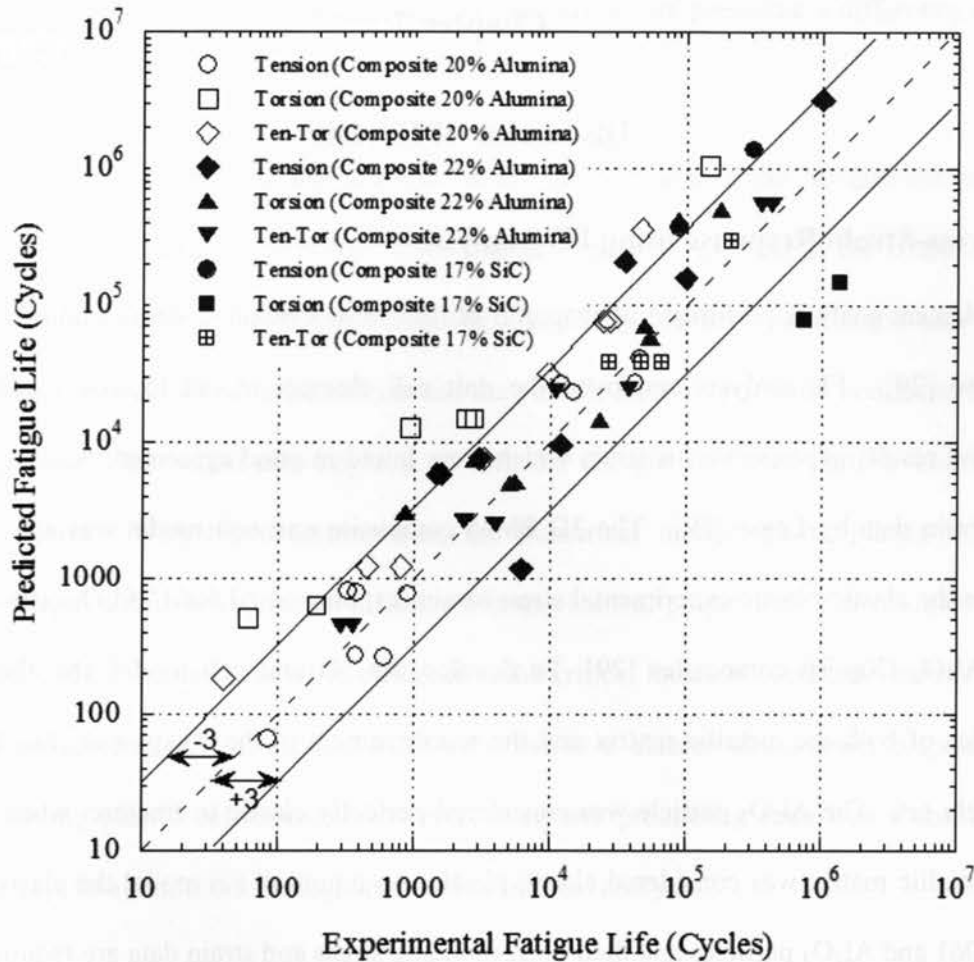


Figure 6.9: Predicted fatigue lives versus experimental fatigue lives for three different PMM composites tested under various loading conditions.

Figure 6.9 verifies good agreements of the experimental and predicted fatigue life results. The predicted lives and the experimental fatigue life for tension, torsion and combined tension-torsion loading conditions fall between the upper and lower bounds within a factor of ± 3 . Of the three life data sets presented in figure 6.9, the Al 6061 / Al₂O₃ / 22p-T6 material shows the predicted and the experimental data along the 45° dashed line representing the best correlations.

Chapter 7

Discussion of Results

7.1. Stress-Strain Response using FE Analysis

Finite element analysis performed in chapter 3 of this thesis evaluated stress-strain data reported by Lease [29]. FE analysis employed the unit cell element model [5,66,67] and achieved numerical results of stress versus strain which were found in good agreement with experimental stress-strain data by Lease [29]. The 3D PMM composite unit cell model was also applied to compare the elastic-plastic experimental stress-strain response of Al 6061/ Al₂O₃ /10p-T6 and Al 6061/ Al₂O₃ /20p-T6 composites [29]. To develop the 3D unit cell model, the elastic-plastic properties of both the metallic matrix and the reinforcement in the Ansys materials library are accurately set. The Al₂O₃ particle was considered perfectly elastic to fracture, where as the Al 6061 metallic matrix was considered elastic-plastic. As inputs of FE model the elastic modulus of Al 6061 and Al₂O₃ particles and their corresponding stress and strain data are required. Ansys workbench material library allowed for the plastic stress-strain response by using a multi-linear plasticity model. This is a built in Multilinear Isotropic Hardening model in Ansys that uses the von Mises yield criterion coupled with an isotropic work hardening assumption. This model is not suited for cyclic or highly non-proportional load histories in small-strain analyses. It is however recommended for large non-cyclic strain analysis, which is preferred for the PMM composite simulations.

Simulated results of stress-strain by Ansys generated for PMM composites under uniaxial loading were found in good agreement with the experimental stress-strain data reported in reference [29]. A comparison of FE results and experimental data showed that elastic strain-

stress possessed the same slope, while plastic strain-stress data presented a difference of 10% in magnitude.

There are several assumptions that are used in the development of the 3D unit cell model that would inevitably lead to errors in the elastic-plastic simulated response of the PMM composite materials. The discontinuous PMM composite was firstly idealized as a single unit cell. This assumes that there are no material defects and the particle remains perfectly bonded to the matrix during loading. This model also neglects to consider the possibility of particle clusters in the metallic matrix. With these assumptions, the numerical models elastic-plastic stress-strain response stayed within a reasonable difference in mechanical properties. The results could have been improved by the use of smaller elements at the critical location of particle-matrix interface. These improvements to the mesh would have led to a clearer stress-strain response of the material during plastic deformation; however, computer processing time was a constraint that had to be kept to a minimum during simulated numerical analysis.

7.2. Fatigue Damage Models Assessment and their Capabilities

7.2.1. Mean Stress Effect

The results of fatigue life are lower in the presence of tensile mean stress and higher in the presence of compressive mean stress [68]. The fatigue life testing of the Al 6061 / SiC / 17w-T6 was conducted with a tensile mean stress ratio of ($R=0.1$). The other three fatigue life data were conducted with the stress ration $R = -1$ (zero mean stress). The capability of the fatigue damage approaches used in this thesis to account for the effect of mean stress was studied. S.W.T. damage model due to its maximum stress component ($\sigma_{max} = \sigma_{mean} + \sigma_{amp}$), takes into

account the effect of mean stress in damage assessment of materials. Ellyin's energy damage model incorporates the effect of mean stress due to the components of stress range and strain range (*ie.*, $\Delta\sigma = \sigma_{min} - \sigma_{max}$). Fatemi-Socie critical plane damage model included a mean stress correlation factor of the maximum value of normal stress during a cycle to modify the damage parameter. Varvani's critical plane-energy damage assessment model showed an analogous mean stress correlation in fatigue damage assessment of materials, where the mean stress acted normal to the critical plane.

7.2.2. Strain Hardening Effect

Under non-proportional loading, the principal stress and strain axes rotate during fatigue loading often causing additional cyclic hardening of materials. A change of loading direction allows more grains to undergo their most favourable orientation for slip, and leads to more active slip systems in producing dislocation interactions and dislocation tangles to form dislocation cells. Interactions strongly affect the hardening behaviour and as the degree of non proportionality increases, the numbers of active slip systems increases. The higher magnitude of strain and stress ranges in the non-proportional tests was due to the effect of an additional strain hardening in the material.

During out-of-phase straining, the magnitude of the normal strain and stress ranges is larger than that for in-phase straining with the same applied shear strain ranges per cycle. Strain hardening effect can be well-described from cyclic stress-strain hysteresis loops. This makes both as Ellyin's and Varvani's energy based models qualified to account this effect in the damage assessment of materials under cyclic loads. While strain-based/ stress-based parameters fail to

take into account this effect. Varvani's damage parameter via its stress and strain ranges increases with the additional hardening caused by non-proportional dependent hardening.

7.2.3. Continuum Mechanics Fundamentals in Models

Critical plane damage parameters developed earlier based on stress or strain components including Brown-Miller and Fatemi-Socie have been criticized for lack of adherence to rigorous continuum mechanics fundamentals. To compensate this, the energy criteria including both stress and strain terms in conjunction with the critical plane approach were developed. One of the most recent damage models of this type was introduced by Varvani [38]. The model is given by the sum of the normal energy range and the shear energy range calculated from the critical plane at which the stress and strain Mohr's circles are the largest during loading and unloading parts of the cycle.

Multiaxial fatigue energy models have been long discussed in terms of normal and shear energy weights. In Guard's approach [69] he found that an empirical weighting factor of $C=0.5$ in the shear energy part of his model gave a good correlation of multiaxial fatigue results for 1% Cr-Mo-V steel for both in-phase and out-of-phase loading conditions.

Tipton [70] found that a good multiaxial fatigue life correlation was obtained for 1045 steel with a scaling factor C of 0.90. Andrews [71] found that a C factor of 0.30 yielded the best correlation of multiaxial life data for AISI 316 stainless steel. Chu et al. [72] weighted the shear energy part of their formulation by a factor of $C=2$ to obtain a good correlation of fatigue results. Liu's [73] and Glinka et al.'s [74] formulations provided an equal weight to normal and shear energies. The empirical factors (C) suggested by each of the authors gave a good fatigue life

correlation for a specific material which suggests that the empirical weighting factor C is material dependent. In the present study, the proposed model correlates multiaxial fatigue lives by normalizing the normal and shear energies using the axial and shear material fatigue properties, respectively, and hence the parameter used no empirical weighting factors.

7.3. Damage Assessment of PMMC's based on Damage Models

Fully reversed fatigue damage data of Al 6061/ Al₂O₃ / 20p-T6, Al 6061/ Al₂O₃ /22p-T6 and Al 6061 / SiC / 17w-T6 composites were evaluated based on various damage models discussed in this thesis including the modified damage model by Varvani. The Ti-6Al-4V / TiC / 10p PMM composite fatigue life data was excluded due to its different metal matrix and its heat treatment other than T6.

Both S.W.T. and Ellyin damage approaches resulted in a wider scatter band when compared with the other three damage approaches of Brown-Miller and Fatemi-Socie critical plane, and Varvani's critical-plane-energy. At high cycle fatigue regime, figure 7.1 presents a decreasing trend and a more unified data for both the critical plane and critical plane-energy approaches. At low cycle regime, Ellyin's and the S.W.T. models correlate the fatigue damage data with life in a more unified fashion than that at high-cycle fatigue regime. At high-cycle fatigue regime, composite materials undergo elastic deformation dominantly, and non-linear response (plastic) deformation of materials during cyclic loads is minimized.

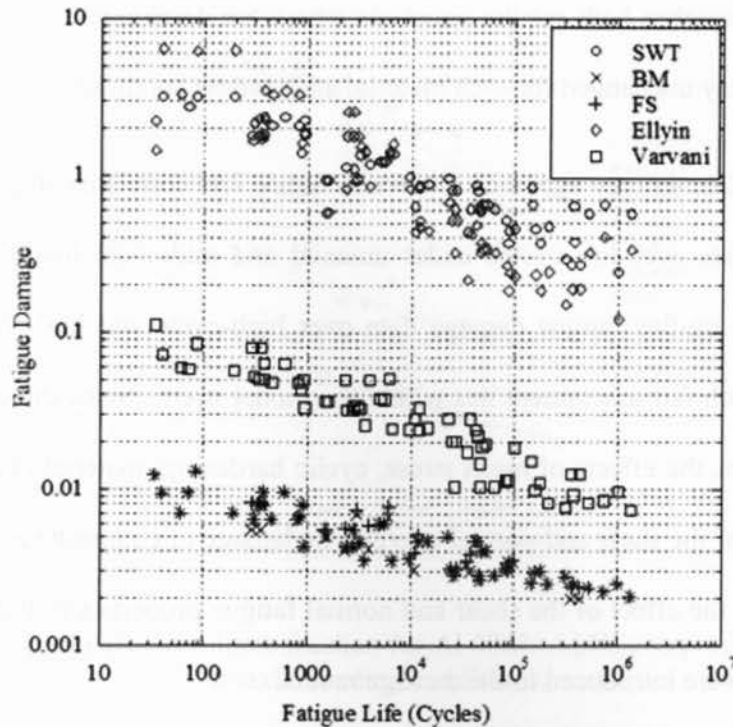


Figure 7.1: Fatigue damage models versus fatigue lives for Al 6061 / Al₂O₃ / 10P-T6, Al 6061 / Al₂O₃ / 20P-T6, and Al 6061 / SiC / 17W-T6 composites tested under various uniaxial and multiaxial loading conditions.

The critical plane-energy assessments show a stronger correlation in predicting the fatigue damage of three Al6061 based composites during uniaxial, shear, and multiaxial fatigue loading conditions at the low-cycle and the high-cycle fatigue regimes. This may suggest that fatigue tensile and shear properties in Varvani's approach weights both the shear and normal energies, while other damage models are not balanced for their shear and normal stress/strain components. Damage assessment based on Brown-Miller and Fatemi-Socie approaches resulted in fairly unified collapsed damage-life data at high cycle fatigue region. While damage data at shorter fatigue lives scattered when evaluated by the critical plane approaches. Brown-Miller and

Fatemi-Socie approaches both require constants which are determined from fatigue life testing. These constants stay unchanged for each material and loading condition.

Varvani critical plane-energy approach (shown in figure 7.1) correlates fatigue damage of PMM composite materials over life cycles under uniaxial and multiaxial loading conditions. This damage approach unifies fatigue damage data over high-cycle and low-cycle fatigue regions. The reason for such fair assessment lies within the model itself. Since the critical plane-energy model incorporates the effects of mean stress, cyclic hardening, material dependent parameters, and contribution of the shear and normal energies in damage of composite materials under cyclic loads. To include the effect of the shear and normal fatigue properties in PMM composites, two terms of α and β were introduced in the damage model.

7.4. The Effect of Particle Volume Fraction

Two materials of Al 6061/ Al₂O₃ /20p-T6 and Al 6061/ Al₂O₃ /22p-T6 consist of volume fractions (V_f) 20% and 22%, respectively, were evaluated under tensile and torsional fatigue loading conditions. The comparison of these two volume fractions may highlight the influence of V_f on the decreasing trend of D-N curves. Figures 7.2 and 7.3 show the slopes D-N data for composites with volume fractions of 20% and 22% tested under uniaxial and torsional fatigue, respectively.

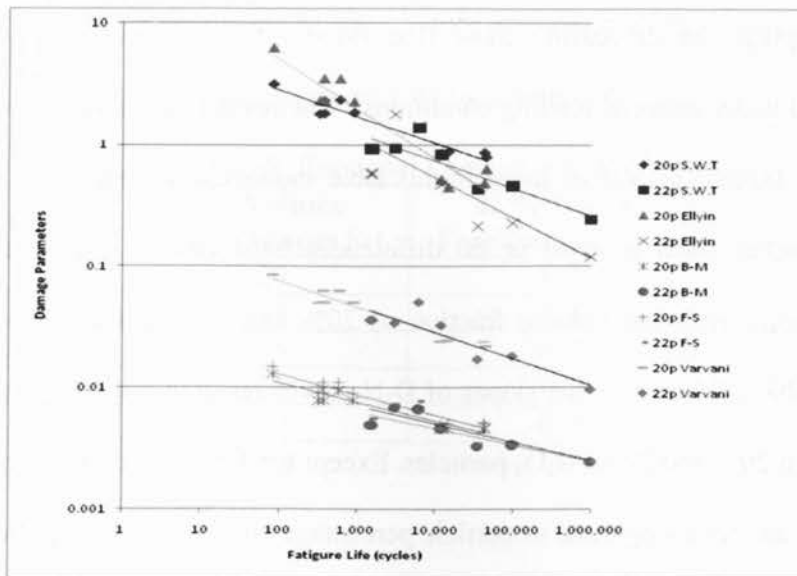


Figure 7.2: Effect of particle volume fraction for Al 6061/ Al₂O₃ composites tested under uniaxial loading conditions.

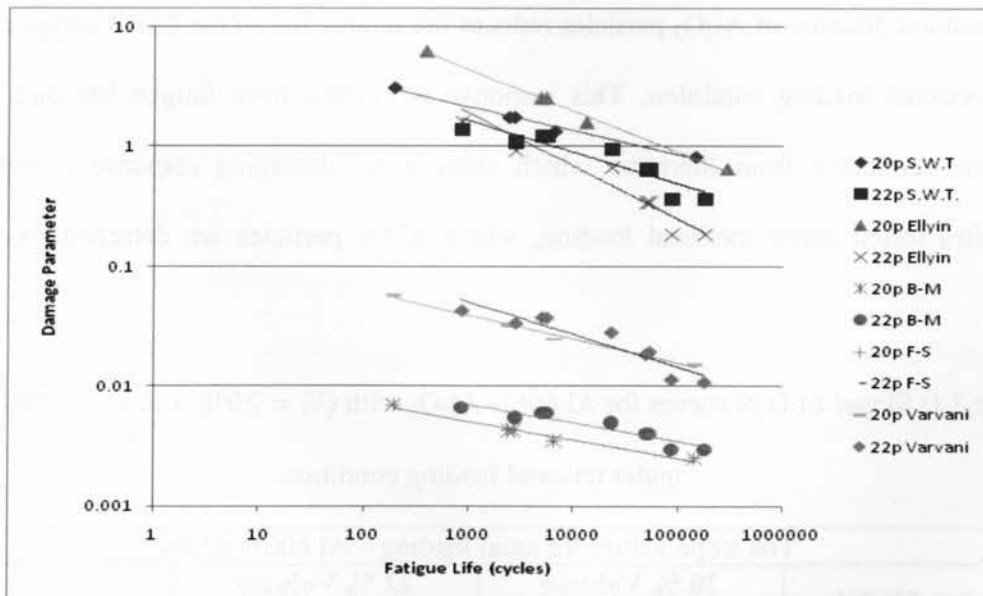


Figure 7.3: Effect of particle volume fraction for Al 6061/ Al₂O₃ composites tested under torsional loading condition.

Figure 7.2 displays the decreasing trend (the slope) of D-N curves for various composite materials tested under uniaxial loading conditions. The results of the slopes of these curves are summarized in Table 7.1. Values listed in this table shows that except Ellyin's approach, other damage approaches show a small or no differences between the slopes of D-N curves for composite samples with the volume fraction of 20% and 22% tested under uniaxial loading conditions. Table 7.2 however list slopes of D-N curves resulted from torsional fatigue tests of composites with 20% and 22% Al₂O₃ particles. Except for Brwon-Miller approach, the slopes in this table show an increasing trend as particle percentage increases. This verifies the fact that the effect of particle volume percentage of MMP composites is more pronounced when components are tested under torsional loading conditions. A higher value of slope corresponds to a steeper D-N curve and therefore a smaller range for predicted fatigue lives. These results indicate that the greater volume fraction of Al₂O₃ particles reduces the fatigue life of the PMM composites tested under torsional loading condition. This response is evident from fatigue life data of PMM composites collected from literature which show more damaging response is reported for composites tested under torsional loading, where Al₂O₃ particles are detached from Al6061 matrix.

Table 7.1: Slopes of D-N curves for Al 6061/ Al₂O₃ with ($V_f = 20\%$ and $V_f = 22\%$) tested under uniaxial loading condition.

| The slope values for axial loading – Al 6061/ Al ₂ O ₃ | | | |
|--|---|---|--------------------------------|
| Damage Model | 20 % Volume Fraction [slopes S ₁] | 22 % Volume Fraction [slopes S ₂] | |
| S.W.T | -0.21 | -0.22 | S ₁ <S ₂ |
| Ellyin | -0.40 | -0.33 | S ₁ >S ₂ |
| Brown-Miller | -0.15 | -0.13 | S ₁ >S ₂ |
| Fatemi-Socie | -0.13 | -0.17 | S ₁ <S ₂ |
| Varvani | -0.21 | -0.21 | S ₁ =S ₂ |

Table 7.2: Slopes of D-N curves for Al 6061/ Al₂O₃ with ($V_f = 20\%$ and $V_f = 22\%$) tested under torsional loading conditions.

| The Slope values: Torsional Loading – Al 6061/ Al ₂ O ₃ | | | |
|---|---|---|--------------------------------|
| Damage Model | 20 % Volume Fraction [slopes S ₁] | 22 % Volume Fraction [slopes S ₂] | |
| S.W.T | -0.20 | -0.26 | S ₁ <S ₂ |
| Ellyin | -0.34 | -0.44 | S ₁ <S ₂ |
| Brown-Miller | -0.15 | -0.15 | S ₁ =S ₂ |
| Fatemi-Socie | -0.15 | -0.27 | S ₁ <S ₂ |
| Varvani | -0.20 | -0.27 | S ₁ <S ₂ |

Chapter 8

Conclusions and Future Research Recommendations

8.1. Conclusions

Fatigue damage of various particle-reinforced metal matrix composites subjected to uniaxial and multiaxial loading conditions have been studied. Composite materials studied in this thesis are Al 6061 / Al₂O₃ / 20p-T6, Al 6061 / Al₂O₃ / 22p-T6, Al 6061 / SiC / 17w-T6, and Ti-6Al-4V / TiC / 10p. The fatigue damage models of Smith-Watson-Topper, Brown-Miller, Fatemi-Socie, Ellyin, and Varvani were used to evaluate fatigue damage over fatigue life of components tested under tensile, torsion, and combined tension-torsion fatigue loading conditions. Over both the low-cycle and high-cycle fatigue regimes, Smith-Watson-Topper approach and Ellyin energy model resulted in a wide scatter range of correlated damage data. Both critical plane models of Brown-Miller and Fatemi-Socie on the other hand collapsed the same fatigue damage data in a reasonably narrower band under uniaxial and multiaxial loading conditions. Fatigue damage model of Varvani successfully correlated fatigue damage in the various loading conditions. Varvani critical plane-energy model is the latest approach incorporating the effects of strain hardening, mean stress, and also material dependent fatigue parameters in damage assessment of materials. Material dependent parameters in this damage approach, enabled an accurate damage assessment of PMMCs as the effect of the shear and normal fatigue properties was accounted in the damage model by means of α and β terms. Material dependent terms of α and β were employed to account for the magnitude of difference between Coffin-Manson coefficients

between the metallic matrix and PMMC. Terms α and β are employed to estimate fatigue damage of PMMCs where strain-life data for the base matrix is enough to be known.

Unit cell FE model was employed to simulate stress-strain results of Al 6061/ Al₂O₃/10p-T6 and Al 6061/ Al₂O₃ / 20p-T6 composites. A single cylindrical shell of metallic matrix Al 6061 with a single spherical ceramic particle Al₂O₃ located in the middle of the cylinder was considered. The volume fraction of the composite determined the total volume size of the particle while holding the matrix volume constant. The simulated stress-strain data were compared with experimentally obtained stress-strain data of the same composite and showed good agreement.

8.2. Future Recommendations

Further research into the fatigue damage assessment of PMM composites is necessary as literature lacks to address various mechanical phenomena, including fatigue response of PMMCs. An extensive amount of fatigue damage data is required to accurately characterize fatigue damage of PMM composites at various conditions including operating temperature, volume fraction of reinforced particles, particle size and shape, and the interface bonding between matrix and particle. Further investigation is essential to find the effect of loading type, loading spectrum, mean stress, environmental and moisture on fatigue damage of this class of composites.

Fatigue life prediction methods based on damage accumulation of microconstituants of PMM composites are yet to be developed. This needs extensive fatigue tests and material modeling.

References

1. A. Brent Strong, Brigham Young University, The History of Composite Materials – Opportunities and Necessities.
2. Miracle DB, Donaldson SL. Introduction to composites. In: ASM handbook. In: Miracle DB, Donaldson SL, editors. Composites, vol. 21. Materials Park: ASM International; 2001. p. 3–17.
3. D.B. Miracle, Metal Matrix composites – From science to technological significance. Material and Manufacturing Directorate, Air Force Research Laboratory. May 2005
4. Lloyd DJ. Int Master Rev 1994;39:1
5. Javier LLorca, Fatigue of Particle-and Whisker-Reinforced Metal-Matrix-Composites. Progress in Materials Science. July 2000
6. ASM Handbook, Volume 21. Composites. 2001, pg. 383
7. B.G. Park, A.G. Crosky, and A.K. Hellier, Material Characterisation and Mechanical Properties of Al₂O₃-Al Metal Matrix Composites. Journal of Material Science Vol. 36 (2001) 2417-2426
8. R.K. Goswami, Ajay Dhar, A.K. Srivastava, and Anil K. Gupta, Effect of Deformation and Ceramic Reinforcement on Work Hardening Behaviour of Hot Extruded 2124 Al-SiCp Metal Matrix Composite. Journal of Composite Materials, Vol. 33, No. 13/1999
9. Embury, J.D., 1985. Metal. Trans. A 16, 2191-2200
10. CES Selector Version 4.6. Granta Design Limited. Build: 2005,2,8,1
11. G. Owolabi, and M. Singh. A comparison between two models that predict the elastic-plastic behaviour of particulate metal matrix composites under multiaxial fatigue type loading
12. P.N. Bindumadhavan, Heng Keng Wah, and O. Prabhakar. Dual Particle size (DPS) composites: Effect on wear and mechanical properties of particulate metal matrix composites. Elsevier Sep. 2000. Pg 112-120
13. J.N. Hall, J.W. Jones, A.K. Sachdev, Mater. Sci. Eng. A138 (1994) pg. 69
14. M. Taya, R.J. Arsenault. Metal Matrix Composites: Thermomechanical behaviour. Pergamon Press, New York, 1989, Pg. 63

15. Materials Data, Metal Matrix Cast Composites, Inc., Waltham MA, 2000
16. H. Zhang, K.T. Ramesh, E.S.C. Chin, High Strain rate response of aluminum 6092 with B_4C composites. *Material Science and Engineering A* 384 (2004) pgs. 26-34
17. M. Wagenhofer, M.A. Erickson-Natishan, R.W. Armstrong, *Scripta Mater.* 41 (1999) pgs. 1177-1184
18. S. Yadev, D.R. Chichili, K.T. Ramesh, *Acta Metal. Mater.* 43 (1995) pg 4453
19. G.M. Newaz et. al. A comparison of mechanical response of MMC at room and elevated temperatures. *Composites Science and Technology* 50 (1994) pgs. 85-90
20. M.A. Martinez, A. Martin, and J. Llorca, *Scripta Metal Mater* 28, (1993) pg. 207
21. Mohammad Jafar Hadianfard, Joseph Healy and Yiu-Wing Mai. Temperature Effect on Fracture Behaviour of an Alumina Particulate-Reinforced 6061 Alumina Composite. *Applied Composite Materials* 1: 93-113 (1994)
22. A.F. Whitehouse and T.W. Clyne, *Proceedings of ICCM/9 Madrid, 1993*, pg. 393
23. J. Onoro, M.D. Salvador, L.E.G. Cambronero. High temperature properties of aluminum alloys reinforced with boron carbide particles. *Materials Science and Engineering A*. September 2008. Pgs. 420-426
24. Z. Xia, F. Ellyin and G. Meijer. Mechanical Behaviour of alumina particle reinforced 6061 aluminum alloy under uniaxial and multiaxial cyclic loading. *Composite Science and Technology* 57 (1997) pgs. 237-248
25. J. Allison And J. Wayne Jones, *Fatigue Behaviour Of Discontinuously Reinforced Metal-Matrix Composites, Fundamentals Of Metal Matrix Composites*, S. Suresh, A. Mortenson, and A. Needleman, ED., 1993
26. J. Gonzalez C.J. *Mech. Phys. Solids* 1998; 46:1-28.
27. Tvergaard V, *International Journal of Fatigue*. 1982. 18:237
28. Madenci, Rodogan and Guven, Ibrahim. *Finite Element Method and Applications in Engineering Using ANSYS*. Springer US. (2006)
29. Kevin Blair Lease. PH.D. Thesis. *Deformation and Fatigue of a Particulate Reinforced Metal Matrix Composite* Iowa University (1994)
30. ASTM E 1150-1987, *Standard Definitions of Fatigue*, 1995 Annual Book of Standards, ASTM, 1995, pg. 753-762

31. Palmgren, A., Die Lebensdauer von Kugellagern. Verfahrenstechnik, Berlin, 1924, 68, 339-341
32. Miner, M. A., Cumulative damage in fatigue. Journal Applied Mechanics. 1945, 67, A 159-A 164.
33. Smith K. N., Watson P. and Topper T.H., A stress-strain function for the fatigue of metals, Journal of Materials, Vol. 5, No 4, 1970, pp.767-776
34. Larson, H. J and Shubert, B.O., Probabilistic Models in Engineering Sciences , Vol. 1. P. 495 New York, 1979
35. Ellyin, F. And Golos, K., A constitutive relation for multiaxial stress states under cyclic conditions. Constitutive law for Engineering Materials – Theory and Application. Elsevier NY. 1987. Pp. 505-512
36. Ellyin, F. And Kujawski, D., Plastic Strain Energy in Fatigue Failure. ASME Journal of Pressure Vessel Technology, Vol. 106 No. 4 1984 pp. 242-247.
37. Kachanov, L.M. Foundation of the theory of plasticity. North-Holland Pub. Co., Amsterdam. 1971
38. A. Varvani-Farahani. A new energy-critical plane parameter for fatigue life assessment of various metallic materials subjected to in-phase and out-of-phase multiaxial fatigue loading conditions. International Journal of Fatigue. Vol. 22 (2000) pp. 295-305
39. Smith RN, Watson P, Topper TH. A stress–strain parameter for the fatigue of metals. J Mat 1970;5(4):767–78.
40. S. Kumai, J.E. King, and J.F. Knott, Fatigue Crack Growth in SiC Particulate-Reinforced Aluminum Alloys, Proc., Fatigue '90: Fourth International Conf. on Fatigue and Fatigue Thresholds, July 1990, p 869–874
41. S.J. Harris and G. Yi, “Fatigue Behaviour of Short-Fibre and Particle-Reinforced Metal Matrix Composites,”Proc., Seventh International Conf. on Composite Materials (ICCM-7), Beijing, People's Republic of China, 1989, p 659–668
42. Melander, M. Rolfson, S. Savage, and S. Preston, Fatigue Crack Growth Behaviour of a α -alumina Short Fibre Reinforced Al- 2Mg Alloy–Part I: Short Cracks, Proc., Fatigue '90: Fourth International Conf. on Fatigue and Fatigue Thresholds, July 1990, p 905–910

43. K. Ishii, K. Tohgo, H. Araki, and K. Oshima, Fatigue Behaviour of SiC/Al Composite Materials, Proc., Sixth International Conf. on Mechanical Behaviour of Materials (ICM-6), July-Aug, 1991, Kyoto, Japan, p 421-426
44. J.J. Bonnen, J.E. Allison, and J.W. Jones, Fatigue Behaviour of a 2xxx Series Aluminum Alloy Reinforced with 15% v/o SiCp, Metall. Trans. A, Vol 23A, 1991, p 1007-1019
45. S. Kumai, J.E. King, and J.F. Knott, Fatigue Crack Growth Behaviour in Molten-Metal Processed SiC Particle-Reinforced Aluminum Alloys, Fatigue Frac. Eng. Mater. Struct., Vol 15 (No. 1), 1992, p 1-11
46. B.R. Crawford and J.R. Griffiths, Initiation and Growth of Short Cracks in an Alumina Reinforced Metal Matrix Composite, Proc., Materials Research Forum 1997: Materials Conservation, Nov 1997, Monash University, Australia, p 105-108
47. J.J. Bonnen, J.E. Allison, and J.W. Jones, Fatigue Behaviour of a 2xxx Series Aluminum Alloy Reinforced with 15% v/o SiCp, Metall. Trans. A, Vol 23A, 1991, p 1007-1019
48. K. Tanaka, M. Kinefuchi, and Y. Akinawa, Fatigue Crack Propagation in SiC Whisker Reinforced Aluminum Alloys, Proc., Fatigue '90: Fourth International Conf. on Fatigue and Fatigue Thresholds, July 1990, p 857-862
49. S. Kumai, J.E. King, and J.F. Knott, Fatigue Crack Growth in SiC Particulate-Reinforced Aluminum Alloys, Proc., Fatigue '90: Fourth International Conf. on Fatigue and Fatigue Thresholds, July 1990, p 869-874S. Suresh, Fatigue of Materials, Cambridge University Press, 1991, p 209-211
50. S. Suresh, Fatigue of Materials, Cambridge University Press, 1991, p 209-211E. Dorre and H. Hubner (1984) Alumina Springer-Verlag
51. T. J. Downes, D.M. Knowles, and J.E. King, Effect of Particle Size and Ageing on the Fatigue Behaviour of an Aluminum Based Metal Matrix Composite, Proc., 8th Biennial Conf. on Fracture (ECF-8), Oct 1990, Turin, p 296-302
52. W.R. Hoover (1989) Commercialization of Duralcan aluminum composites. Design and Manufacturing of advanced composites, ASM-ESD, 211-217
53. E. Dorre and H. Hubner (1984) Alumina Springer-Verlag
54. T.F. Klimowicz (1994) Duralcan Property data. Publication of Duralcan Wrought Products

55. Standard E606-92 (1993) Standard practice for strain-controlled testing 1993. Annual Book of ASTM standards. Vol. 3.01
56. K.B. Lease, R.I. Stephens, Yan Yao Jiang and P. Kurath. Fatigue of a particulate reinforced aluminum metal matrix composite subjected to axial, torsional and combined axial/torsional loading conditions. *Fatigue fracture of engineering materials*. Vol. 19, No. 8, pp. 1031-1043. 1996
57. Z. Xia and F. Ellyin. Multiaxial Fatigue of an aluminum particle reinforced aluminum alloy. (1998) *International Journal of fatigue*. Vol. 20 No. 1. Pp 51-56
58. M.B. Ruggles. Experimental Investigation of Uniaxial and Biaxial Rate-Dependent Behaviour of a Discontinuous Metal-Matrix Composite at 538°C. *Composites Science and Technology*. Vol. 57 (1997) pp. 307-318
59. MD. Rafiquzzaman, Y. Arai and E. Tsuchida. Fracture Mechanisms of Aluminum Cast alloy locally reinforced by SiC Particles and Al₂O₃ Whiskers under Monotonic and cyclic loads. Institute of Materials, Minerals and Mining. (2008)
60. Yulong Li, K.T. Ramesh and E.S.C. Chin. The mechanical response of an A359/SiCp MMC and the A359 aluminum matrix to dynamic shearing deformations. *Materials Science and Engineering*. A 382 (2004) pp. 162-170
61. E. King, C. Mercer, S. Allameh, O. Popoola, and W.O. Soboyejo. An Investigation of Fracture and Fatigue in a Metal/polymer Composite. *Metallurgical and Materials Transactions*. Vol. 32A, Aug 2001
62. Chingshen li, F. Ellyin. Fatigue damage and its localization in particulate metal matrix composites. *Material Science and Engineering*. A214 (1996) pp. 115-121
63. H Ding, O. Hartmann, H. Biermann and H. Mughrabi. Modeling low-cycle fatigue life of particulate-reinforced metal-matrix composites. *Materials Science and Engineering*. A333 (1-2), pp. 295-305 (2002)
64. M.J. Hadianfard and Y.W. Mai. Low Cycle Fatigue Behaviour of Particulate Reinforced Metal Matrix Composites. *Journal of Materials Science* 35 (7), pp. 1715-1723 (2000)
65. P.C. Chen, S.J. Lin, and M.T. Jahn. A Study on the low-cycle Fatigue properties of SiCp/6061 Al Composites. *Journal of Materials Science* 32 (15), pp. 4153-4158 (1997)

66. Guizheng Kang, Sujuan Guo, Cheng Dong. Numerical simulation for uniaxial cyclic deformation of discontinuously reinforced metal matrix composites. *Materials Science and Engineering. A* 426 (2006) pp. 66-76
67. W.J. Fleming, J.M. Temis. Numerical simulation of cyclic plasticity and damage of an aluminum metal matrix composite with particulate SiC inclusions. *International Journal of Fatigue. Vol. 24* (2002) pp. 1079-1088
68. Sines G. The prediction of fatigue fracture under combined stresses at stress concentrations. *Bull Jpn Soc Mech Eng* 1961;4(15):443-53.
69. Garud, Y.S. Multiaxial fatigue: A Survey of the State of the Art. (1981) *Journal of Testing and Evaluation*, 9 (3), pp. 165-1782
70. Tipton, S.M. (1984) *Fatigue Behaviour Under Multiaxial Loading in the Presence of a Notch: Methodologies for the Prediction of Life to Crack Initiation and Life Spent in Crack Propagation*. Ph.D. Thesis, Mechanical Engineering Department, Stanford University, Stanford, CA
71. Andrews, R.M. (1986) *High Temperature Fatigue of AISI 316 Stainless Steel Under Complex Biaxial Loading*. Ph.D. Thesis, University of Sheffield, UK
72. Chu, Chin-Chan, Conle, F. Albrecht, Bonnen, John J.F. Multiaxial stress-strain modeling and fatigue life prediction of SAE axle shafts (1993) *ASTM Special Technical Publication*, (1191), pp. 37-54.
73. Liu, K.C. Method based on virtual strain-energy parameters for multiaxial fatigue life prediction (1993) *ASTM Special Technical Publication*, (1191), pp. 67-84.
74. Glinka, G., Shen, G., Plumtree, A. Multiaxial fatigue strain energy density parameter related to the critical fracture plane (1995) *Fatigue and Fracture of Engineering Materials and Structures*, 18 (1), pp. 37-46.
75. Lin, H., Nayeb-Hashemi, H. And Pelloux, R.M. Constitutive relations and fatigue life prediction for anisotropic Al-6061-T6 rods under biaxial proportional loadings. *International Journal of Fatigue. Vol. 14, Iss. 4, July 1992*, pp. 249-259

Appendix A

Appendix A details the theoretical and experimental material and fatigue data used throughout this thesis. Tables (A1-1) through (A1-8) present the mechanical properties of the metallic matrix alloys, the ceramic reinforcements, and the various particle metal matrix composites studied in this thesis. Tables (A1-9) through (A1-12) present the Coffin-Manson parameters for each of the particle metal matrix composites used in this thesis. Tables (A2-1) through (A2-16) present the experimental data of the four PMM composite materials under strain and stress controlled fatigue testing. This data was composed of uniaxial, torsion, and combined biaxial tension/torsion loading conditions. Along with the experimental data, the Smith-Watson-Topper damage parameters were tabulated for each cyclic fatigue data set. Tables (A3-1) through (A3-16) tabulate the cyclic fatigue results of the Brown-Miller and Fatemi-Socie critical plane damage parameters for each of the four PMM composites studied in this thesis. Tables (A4-1) through (A4-14) present Ellyin's energy damage parameters for each PMM composite studied during fatigue cycling. Tables (A5-1) through (A5-14) present the Varvani critical plane-energy damage parameters for each of the four PMM composite materials undergoing cyclic fatigue test

Table A1-1: Al 6061-T6 Mechanical Properties

| Aluminum 6061-T6 | |
|------------------------------|-------|
| Density [kg/m ³] | 2730 |
| Elongation [%] | 12 |
| Elastic Limit [MPa] | 290 |
| Poisson's Ratio | 0.335 |
| Ultimate Strength [MPa] | 320 |
| Elastic Modulus [GPa] | 74 |

Table A1-2: Ti-6Al-4V Mechanical Properties

| Ti-6Al-4V | |
|------------------------------|------|
| Density [kg/m ³] | 4430 |
| Elongation [%] | 13 |
| Elastic Limit [MPa] | 1080 |
| Poisson's Ratio | 0.37 |
| Ultimate Strength [MPa] | 1270 |
| Elastic Modulus [GPa] | 119 |

Table A1-3: Aluminum Oxide (Al₂O₃) Mechanical Properties

| Aluminum Oxide (Alumina Particulate) | |
|---|------|
| Density [kg/m ³] | 4000 |
| Elongation [%] | N/A |
| Elastic Limit [MPa] | 273 |
| Poisson's Ratio | 0.27 |
| Ultimate Strength [MPa] | 273 |
| Elastic Modulus [GPa] | 410 |

Table A1-4: Silicon Carbide (SiC) Mechanical Properties

| Silicon Carbide Particulate | |
|------------------------------------|------|
| Density [kg/m ³] | 3210 |
| Elongation [%] | N/A |
| Elastic Limit [MPa] | 525 |
| Poisson's Ratio | 0.24 |
| Ultimate Strength [MPa] | 525 |
| Elastic Modulus [GPa] | 461 |

Table A1-5: Titanium Carbide (TiC) Mechanical Properties

| Titanium Carbide Particulate | |
|-------------------------------------|--------|
| Density [kg/m ³] | 13,900 |
| Elongation [%] | N/A |
| Elastic Limit [MPa] | 250 |
| Poisson's Ratio | 0.25 |
| Ultimate Strength [MPa] | 250 |
| Elastic Modulus [GPa] | 375 |

Table A1-6: 6061 / Al₂O₃ / 20p-T6 Mechanical Properties

| 6061/ Al₂O₃ / 20p-T6 | |
|---|-------|
| Density [kg/m ³] | 2970 |
| Elongation [%] | 2.1 |
| Elastic Limit [MPa] | 360 |
| Poisson's Ratio | 0.31 |
| Ultimate Strength [MPa] | 389 |
| Elastic Modulus [GPa] | 100 |
| Ramberg-Osgood Coefficient K' | 571.6 |
| Ramberg-Osgood Exponent n' | 0.069 |

Table A1-7: 6061 / SiC / 17w-T6 Mechanical Properties

| 6061/SiC/17w-T6 | |
|-------------------------------|-------|
| Density [kg/m ³] | 2785 |
| Elongation [%] | 3.4 |
| Elastic Limit [MPa] | 469 |
| Poisson's Ratio | 0.30 |
| Ultimate Strength [MPa] | 670 |
| Elastic Modulus [GPa] | 121 |
| Ramberg-Osgood Coefficient K' | 869 |
| Ramberg-Osgood Exponent n' | 0.146 |

Table A1-8: Ti-6Al-4V / TiC / 10p Mechanical Properties

| Ti-6Al-4V / TiC / 10p | |
|-------------------------------|-------|
| Density [kg/m ³] | 4507 |
| Elongation [%] | 2.1 |
| Elastic Limit [MPa] | 945 |
| Poisson's Ratio | 0.35 |
| Ultimate Strength [MPa] | 960 |
| Elastic Modulus [GPa] | 120 |
| Ramberg-Osgood Coefficient K' | 760.7 |
| Ramberg-Osgood Exponent n' | 0.08 |

Table A1-9: 6061 / Al₂O₃ / 20p-T6 Coffin-Manson Fatigue Parameters

| 6061 / Al ₂ O ₃ / 20p-T6 | | | |
|--|--------|-----------------|-----------|
| σ'_f [Mpa] | 596 | τ'_f [MPa] | 344 |
| ϵ'_f | 0.034 | γ'_f | 0.3193744 |
| b | -0.107 | b_s | -0.107 |
| c | -0.414 | c_s | -0.414 |

Table A1-10: 6061 / Al₂O₃ / 22p-T6 Coffin-Manson Fatigue Parameters

| 6061 / Al₂O₃ / 22p-T6 | | | |
|--|--------|-----------------------------------|-----------|
| σ'_f [MPa] | 596 | τ'_f [MPa] | 344 |
| ϵ'_f | 0.034 | γ'_f | 0.3193744 |
| b | -0.107 | b_s | -0.107 |
| c | -0.414 | c_s | -0.414 |

Table A1-11: 6061 / SiC / 17w-T6 Coffin-Manson Fatigue Parameters

| 6061/ SiC / 17w-T6 | | | |
|--------------------|---------|-----------------|---------|
| σ'_f [MPa] | 638 | τ'_f [MPa] | 368 |
| ϵ'_f | 0.12 | γ'_f | 0.069 |
| b | -0.0978 | b_s | -0.0978 |
| c | -0.67 | c_s | -0.67 |

Table A1-12: Ti-6Al-4V / TiC / 10p Coffin-Manson Fatigue Parameters

| Ti-6Al-4V / TiC / 10p | | | |
|------------------------------|--------|-----------------|-------|
| σ'_f [MPa] | 492 | τ'_f [MPa] | 284 |
| ϵ'_f | 0.1107 | γ'_f | 0.192 |
| b | -0.08 | b_s | -0.08 |
| c | -0.40 | c_s | -0.40 |

Table A1-12: Al 6061-T6 tension, torsion and combined tension-torsion strain-life data

| $\Delta\epsilon/2$ (%) | $\Delta\gamma/2$ (%) | $N_{10\%}$ | λ |
|------------------------|----------------------|------------|-----------|
| 0.59 | - | 2160 | 0 |
| 0.655 | - | 1470 | 0 |
| 0.7 | - | 1140 | 0 |
| 0.755 | - | 670 | 0 |
| 0.81 | - | 480 | 0 |
| 0.585 | - | 2200 | 0 |
| 0.66 | - | 1450 | 0 |
| 0.745 | - | 690 | 0 |
| - | 0.784 | 3360 | ∞ |
| - | 0.854 | 1980 | ∞ |
| - | 0.924 | 1310 | ∞ |
| - | 1.022 | 960 | ∞ |
| - | 1.092 | 600 | ∞ |
| - | 1.288 | 370 | ∞ |
| - | 0.98 | 3260 | ∞ |
| - | 1.19 | 1900 | ∞ |
| - | 1.372 | 1250 | ∞ |
| - | 1.54 | 940 | ∞ |
| - | 1.736 | 700 | ∞ |
| 0.45 | 0.45 | 2810 | 1 |
| 0.55 | 0.55 | 1020 | 1 |
| 0.70 | 0.70 | 390 | 1 |
| 0.35 | 0.70 | 1680 | 2 |
| 0.45 | 0.90 | 930 | 2 |
| 0.55 | 1.10 | 280 | 2 |
| 0.515 | 0.525 | 1810 | 1 |

| | | | |
|-------|-------|------|---|
| 0.56 | 0.574 | 1320 | 1 |
| 0.672 | 0.672 | 780 | 1 |
| 0.41 | 0.82 | 1580 | 2 |
| 0.50 | 1.01 | 920 | 2 |
| 0.61 | 1.23 | 500 | 2 |

Table A2-1: 6061 / Al₂O₃ / 20p-T6 Experimental Strain-Life Data and Calculated S.W.T.

damage Parameters for Pure Tension (Shaft test specimen)

| Tensile Strain Amplitude ($\Delta\varepsilon/2$) | Maximum Stress (σ_{max}) [MPa] | Fatigue Life (N_f) | S.W.T. Damage Parameter |
|--|---|--|------------------------------------|
| 0.008 | 396 | 85 | 3.168 |
| 0.006 | 390 | 599 | 2.34 |
| 0.006 | 385 | 376 | 2.31 |
| 0.005 | 358 | 331 | 1.79 |
| 0.005 | 361 | 379 | 1.805 |
| 0.005 | 367 | 909 | 1.835 |
| 0.003 | 290 | 14,712 | 0.87 |
| 0.003 | 280 | 11,886 | 0.84 |
| 0.003 | 262 | 44,640 | 0.786 |
| 0.003 | 285 | 42,245 | 0.855 |

Table A2-2: 6061 / Al₂O₃ / 20p-T6 Experimental Strain-Life Data and Calculated S.W.T.

damage Parameters for Pure Torsion (Shaft test specimen)

| Shear Strain Amplitude ($\Delta\gamma/2$) | Maximum Shear Stress (τ_{max}) [MPa] | Fatigue Life (N_f) | S.W.T. Damage Parameter |
|--|--|------------------------|----------------------------|
| 0.014 | 224 | 195 | 3.136 |
| 0.0086 | 206 | 2,735 | 1.7716 |
| 0.0086 | 206 | 2,423 | 1.7716 |
| 0.007 | 193 | 6,619 | 1.351 |
| 0.005 | 165 | 146,788 | 0.825 |

Table A2-3: 6061 / Al₂O₃ / 20p-T6 Experimental Strain-Life Data and Calculated S.W.T.

damage Parameters for Pure Torsion (tubular test specimen)

| Shear Strain Amplitude ($\Delta\gamma/2$) | Maximum Shear Stress (τ_{max}) [MPa] | Fatigue Life (N_f) | S.W.T. Damage Parameter |
|--|--|------------------------|----------------------------|
| 0.014 | 233 | 60 | 3.262 |
| 0.0086 | 212 | 937 | 1.8232 |
| 0.007 | 201 | 3,601 | 1.407 |

Table A2-4: 6061 / Al₂O₃ / 20p-T6 Experimental Strain-Life Data and Calculated S.W.T.

damage Parameters for Combined Tension-Torsion (Shaft test specimen)

| Tensile Strain Amplitude ($\Delta\epsilon/2$) | Maximum Stress (σ_{max}) [MPa] | Shear Strain Amplitude ($\Delta\gamma/2$) | Maximum Shear Stress (τ_{max}) [MPa] | Fatigue Life (N_f) | S.W.T. Damage Parameter |
|---|---|---|---|----------------------------------|--------------------------------|
| 0.0058 | 240 | 0.01 | 176 | 40 | 3.152 |
| 0.004 | 231 | 0.007 | 162 | 800 | 2.058 |
| 0.004 | 231 | 0.007 | 162 | 452 | 2.058 |
| 0.0029 | 215 | 0.005 | 144 | 3,234 | 1.3435 |
| 0.0029 | 215 | 0.005 | 144 | 3,233 | 1.3435 |
| 0.0023 | 200 | 0.004 | 127 | 9,597 | 0.968 |
| 0.002 | 192 | 0.0035 | 116 | 27,433 | 0.79 |
| 0.002 | 192 | 0.0035 | 116 | 24,754 | 0.79 |
| 0.0017 | 162 | 0.003 | 102 | 47,000 | 0.5814 |

Table A2-5: 6061 / Al₂O₃ / 20p-T6 Experimental Strain-Life Data and Calculated S.W.T. damage Parameters for Combined Tension-Torsion (Tubular test specimen)

| Tensile Strain Amplitude ($\Delta\varepsilon/2$) | Maximum Stress (σ_{max}) [MPa] | Shear Strain Amplitude ($\Delta\gamma/2$) | Maximum Shear Stress (τ_{max}) [MPa] | Fatigue Life (N_f) | S.W.T. Damage Parameter |
|--|--|---|---|----------------------------------|--------------------------------|
| 0.0058 | 180 | 0.01 | 167 | 72 | 2.714 |
| 0.004 | 255 | 0.007 | 159 | 304 | 2.133 |

A2-6: 6061 / Al₂O₃ / 22p-T6 Experimental Strain-Life Data and Calculated S.W.T. damage

Parameters for Pure Tension

| Tensile Strain Amplitude ($\Delta\varepsilon/2$) | Maximum Stress (σ_{max}) [MPa] | Fatigue Life (N_f) | S.W.T. Damage Parameter |
|--|---|--|------------------------------------|
| 0.003 | 307 | 1,574 | 0.921 |
| 0.002 | 214 | 35,000 | 0.428 |
| 0.003 | 307 | 1,472 | 0.921 |
| 0.0015 | 161 | 999,033 | 0.241 |
| 0.00395 | 347 | 6,154 | 1.369 |
| 0.00206 | 220 | 99,001 | 0.454 |
| 0.00405 | 230 | 3,029 | 0.931 |
| 0.00281 | 294 | 1,882 | 0.825 |

A2-7: 6061 / Al₂O₃ / 22p-T6 Experimental Strain-Life Data and Calculated S.W.T. damage

Parameters for Pure Shear

| Shear Strain Amplitude ($\Delta\gamma/2$) | Maximum Shear Stress (τ_{max}) [MPa] | Fatigue Life (N_f) | S.W.T. Damage Parameter |
|--|--|------------------------|----------------------------|
| 0.004 | 162 | 53,475 | 0.649 |
| 0.005 | 190 | 23,053 | 0.951 |
| 0.003 | 122 | 86,551 | 0.367 |
| 0.006 | 205 | 5,013 | 1.229 |
| 0.0055 | 199 | 2,786 | 1.092 |
| 0.0066 | 210 | 855 | 1.389 |
| 0.003 | 122 | 178,295 | 0.367 |
| 0.004 | 162 | 49,178 | 0.648 |
| 0.006 | 205 | 5,542 | 1.229 |

A2-8: 6061 / Al₂O₃ / 22p-T6 Experimental Strain-Life Data and Calculated S.W.T. damage

Parameters for combined bi-axial in-phase tension-torsion

| Tensile Strain Amplitude ($\Delta\varepsilon/2$) | Maximum Stress (σ_{max}) [MPa] | Shear Strain Amplitude ($\Delta\gamma/2$) | Maximum Shear Stress (τ_{max}) [MPa] | Fatigue Life (N_f) | S.W.T. Damage Parameter |
|--|---|---|---|----------------------------------|--------------------------------|
| 0.002 | 213 | 0.00415 | 167 | 2,325 | 1.121 |
| 0.0025 | 266 | 0.00564 | 201 | 357 | 1.796 |
| 0.0015 | 161 | 0.00307 | 125 | 10,911 | 0.626 |
| 0.001 | 107 | 0.00198 | 81 | 358,912 | 0.267 |
| 0.0025 | 266 | 0.00561 | 200 | 291 | 1.787 |
| 0.002 | 213 | 0.00430 | 172 | 3,940 | 1.168 |
| 0.0015 | 161 | 0.00298 | 122 | 37,645 | 0.604 |
| 0.001 | 107 | 0.00198 | 81 | 426,542 | 0.267 |

A2-9: 6061 / SiC / 17w-T6 Experimental Strain-Life Data and Calculated S.W.T. damage

Parameters for $\lambda=0$ (pure tension)

| Tensile Strain Amplitude ($\Delta\varepsilon/2$) | Maximum Stress (σ_{max}) [MPa] | Fatigue Life (N_f) | S.W.T. Damage Parameter |
|--|---|--|------------------------------------|
| 0.002195 | 199 | 88,756 | 0.437 |
| 0.001779 | 164 | 314,730 | 0.291 |

A2-10: 6061 / SiC / 17w-T6 Experimental Strain-Life Data and Calculated S.W.T. damage

Parameters for $\lambda=\infty$ (pure shear)

| Shear Strain Amplitude ($\Delta\gamma/2$) | Maximum Shear Stress (τ_{max}) [MPa] | Fatigue Life (N_f) | S.W.T. Damage Parameter |
|--|--|------------------------|----------------------------|
| 0.00438 | 85 | 733,899 | 0.644 |
| 0.004074 | 79 | 1,338,899 | 0.565 |

A2-11: 6061 / SiC / 17w-T6 Experimental Strain-Life Data and Calculated S.W.T. damage

Parameters for $\lambda=0.5$ (biaxial in-phase)

| Tensile Strain Amplitude ($\Delta\varepsilon/2$) | Maximum Stress (σ_{max}) [MPa] | Shear Strain Amplitude ($\Delta\gamma/2$) | Maximum Shear Stress (τ_{max}) [MPa] | Fatigue Life (N_f) | S.W.T. Damage Parameter |
|--|---|---|---|--|--|
| 0.00184 | 170 | 0.00240 | 85 | 83,588 | 0.516 |
| 0.00173 | 159 | 0.00225 | 79 | 158,322 | 0.453 |

A2-12: 6061 / SiC / 17w-T6 Experimental Strain-Life Data and Calculated S.W.T. damage

Parameters for $\lambda=1$ (equal bi-axial in phase)

| Tensile Strain Amplitude ($\Delta\varepsilon/2$) | Maximum Stress (σ_{max}) [MPa] | Shear Strain Amplitude ($\Delta\gamma/2$) | Maximum Shear Stress (τ_{max}) [MPa] | Fatigue Life (N_f) | S.W.T. Damage Parameter |
|--|---|---|---|----------------------------------|--------------------------------|
| 0.00133 | 123 | 0.00355 | 123 | 26,292 | 0.599 |
| 0.00133 | 123 | 0.00355 | 123 | 46,477 | 0.599 |
| 0.00133 | 123 | 0.00355 | 123 | 64,519 | 0.599 |
| 0.00118 | 109 | 0.00118 | 109 | 212,321 | 0.469 |

A2-13: 6061 / SiC / 17w-T6 Experimental Strain-Life Data and Calculated S.W.T. damage

Parameters for $\lambda=2$ (biaxial in-phase)

| Tensile Strain Amplitude ($\Delta\epsilon/2$) | Maximum Stress (σ_{max}) [MPa] | Shear Strain Amplitude ($\Delta\gamma/2$) | Maximum Shear Stress (τ_{max}) [MPa] | Fatigue Life (N_f) | S.W.T. Damage Parameter |
|---|--|---|---|----------------------------------|--------------------------------|
| 0.000758 | 70 | 0.00414 | 140 | 372,566 | 0.634 |
| 0.000719 | 67 | 0.00388 | 133 | 519,561 | 0.565 |

A2-14: Ti-6Al-4V / TiC / 10p Experimental Strain-Life Data and Calculated S.W.T. damage

Parameters for tensile loading

| Tensile Strain Amplitude ($\Delta\varepsilon/2$) | Maximum Stress (σ_{max}) [MPa] | Fatigue Life (N_f) | S.W.T. Damage Parameter |
|--|---|--|------------------------------------|
| 0.005 | 375 | 78 | 1.875 |
| 0.005 | 375 | 84 | 1.875 |
| 0.003 | 284 | 1,765 | 0.852 |

A2-15: Ti-6Al-4V / TiC / 10p Experimental Strain-Life Data and Calculated S.W.T. damage

Parameters for pure shear loading

| Shear Strain Amplitude ($\Delta\gamma/2$) | Maximum Shear Stress (τ_{max}) [MPa] | Fatigue Life (N_f) | S.W.T. Damage Parameter |
|--|--|------------------------|----------------------------|
| 0.006 | 184 | 206 | 1.104 |
| 0.006 | 184 | 466 | 1.104 |

A2-16: Ti-6Al-4V / TiC / 10p Experimental Strain-Life Data and Calculated S.W.T. damage

Parameters for multiaxial 90° out-of-phase loading

| Tensile Strain Amplitude ($\Delta\epsilon/2$) | Maximum Stress (σ_{max}) [MPa] | Shear Strain Amplitude ($\Delta\gamma/2$) | Maximum Shear Stress (τ_{max}) [MPa] | Fatigue Life (N_f) | S.W.T. Damage Parameter |
|---|---|---|---|------------------------|-------------------------|
| 0.0035 | 325 | 0.006 | 178 | 34 | 2.203 |

A3-1: Al 6061 / Al₂O₃ / 20p-T6 Critical Plane damage models calculated variables and
Parameters for Uniaxial Loading (Shaft test specimen)

| Brown-Miller Data | | | Fatemi-Socie Data | | |
|------------------------|-----------------------|-------------------------------------|------------------------|--------------------------|-------------------------------------|
| $\Delta\gamma_{max}/2$ | $\Delta\varepsilon_n$ | Brown-Miller Damage Parameter | $\Delta\gamma_{max}/2$ | $\sigma_{n_{max}}$ [MPa] | Fatemi-Socie Damage Parameter |
| 0.0113 | 0.00478 | 0.0128 | 0.0113 | 198 | 0.01509 |
| 0.0084 | 0.00376 | 0.00951 | 0.0084 | 195 | 0.00112 |
| 0.00838 | 0.00375 | 0.00952 | 0.00838 | 193 | 0.0111 |
| 0.00687 | 0.00320 | 0.00788 | 0.00687 | 179 | 0.00897 |
| 0.006882 | 0.003207 | 0.00788 | 0.006882 | 181 | 0.0090 |
| 0.00693 | 0.003219 | 0.00787 | 0.00693 | 184 | 0.00911 |
| 0.00408 | 0.002068 | 0.00463 | 0.00408 | 145 | 0.00509 |
| 0.00407 | 0.002048 | 0.00464 | 0.00407 | 140 | 0.00504 |
| 0.00413 | 0.002013 | 0.00467 | 0.00413 | 131 | 0.00505 |
| 0.00413 | 0.002058 | 0.00464 | 0.00413 | 143 | 0.00513 |

A3-2: Al 6061 / Al₂O₃ / 20p-T6 Critical Plane damage models calculated variables and
Parameters for Torsion Loading (Shaft test specimen)

| Brown-Miller Data | | | Fatemi-Socie Data | | |
|------------------------|--------------------|-------------------------------------|------------------------|--------------------------|-------------------------------------|
| $\Delta\gamma_{max}/2$ | $\Delta\epsilon_n$ | Brown-Miller Damage Parameter | $\Delta\gamma_{max}/2$ | $\sigma_{n_{max}}$ [MPa] | Fatemi-Socie Damage Parameter |
| 0.007 | 0 | 0.007 | 0.007 | 0 | 0.007 |
| 0.0043 | 0 | 0.0043 | 0.0043 | 0 | 0.0043 |
| 0.0043 | 0 | 0.0043 | 0.0043 | 0 | 0.0043 |
| 0.0035 | 0 | 0.0035 | 0.0035 | 0 | 0.0035 |
| 0.0025 | 0 | 0.0025 | 0.0025 | 0 | 0.0025 |

A3-3: Al 6061 / Al₂O₃ / 20p-T6 Critical Plane damage models calculated variables and

Parameters for Torsion Loading (Tubular test specimen)

| Brown-Miller Data | | | Fatemi-Socie Data | | |
|------------------------|-----------------------|-------------------------------------|------------------------|--------------------------|-------------------------------------|
| $\Delta\gamma_{max}/2$ | $\Delta\varepsilon_n$ | Brown-Miller Damage Parameter | $\Delta\gamma_{max}/2$ | $\sigma_{n_{max}}$ [MPa] | Fatemi-Socie Damage Parameter |
| 0.007 | 0 | 0.007 | 0.007 | 0 | 0.007 |
| 0.0043 | 0 | 0.0043 | 0.0043 | 0 | 0.0043 |
| 0.0035 | 0 | 0.0035 | 0.0035 | 0 | 0.0035 |

A3-4: Al 6061 / Al₂O₃ / 20p-T6 Critical Plane damage models calculated variables and

Parameters for Combined tension-torsion Loading (Shaft test specimen)

| Brown-Miller Data | | | Fatemi-Socie Data | | |
|------------------------|--------------------|-------------------------------------|------------------------|------------------------|-------------------------------------|
| $\Delta\gamma_{max}/2$ | $\Delta\epsilon_n$ | Brown-Miller Damage Parameter | $\Delta\gamma_{max}/2$ | $\sigma_{n,max}$ [MPa] | Fatemi-Socie Damage Parameter |
| 0.00823 | 0.00337 | 0.00938 | 0.00823 | 120 | 0.00992 |
| 0.00555 | 0.00245 | 0.00638 | 0.00555 | 116 | 0.00664 |
| 0.00555 | 0.00245 | 0.00638 | 0.00555 | 116 | 0.00664 |
| 0.00393 | 0.00187 | 0.00456 | 0.00393 | 108 | 0.00465 |
| 0.00393 | 0.00187 | 0.00456 | 0.00393 | 108 | 0.00465 |
| 0.00306 | 0.00154 | 0.00358 | 0.00306 | 100 | 0.00358 |
| 0.00262 | 0.00138 | 0.00309 | 0.00262 | 96 | 0.00305 |
| 0.00262 | 0.00138 | 0.00309 | 0.00262 | 96 | 0.00305 |
| 0.00223 | 0.00117 | 0.00263 | 0.00223 | 81 | 0.00254 |

A3-5: Al 6061 / Al₂O₃ / 20p-T6 Critical Plane damage models calculated variables and

Parameters for Combined Tension-Torsion Loading (Tubular test specimen)

| Brown-Miller Data | | | Fatemi-Socie Data | | |
|------------------------|-----------------------|-------------------------------------|------------------------|--------------------------|-------------------------------------|
| $\Delta\gamma_{max}/2$ | $\Delta\varepsilon_n$ | Brown-Miller Damage Parameter | $\Delta\gamma_{max}/2$ | $\sigma_{n_{max}}$ [MPa] | Fatemi-Socie Damage Parameter |
| 0.00835 | 0.00325 | 0.00945 | 0.00835 | 90 | 0.00963 |
| 0.00550 | 0.00250 | 0.00635 | 0.00550 | 127.5 | 0.00669 |

A3-6: Al 6061 / Al₂O₃ / 22p-T6 Critical Plane damage models calculated variables and
Parameters for Uniaxial Loading

| Brown-Miller Data | | | Fatemi-Socie Data | | |
|------------------------|-----------------------|-------------------------------------|------------------------|--------------------------|-------------------------------------|
| $\Delta\gamma_{max}/2$ | $\Delta\varepsilon_n$ | Brown-Miller Damage Parameter | $\Delta\gamma_{max}/2$ | $\sigma_{n_{max}}$ [MPa] | Fatemi-Socie Damage Parameter |
| 0.0044 | 0.0016 | 0.00494 | 0.0044 | 154 | 0.00555 |
| 0.0029 | 0.0011 | 0.00327 | 0.0029 | 107 | 0.00343 |
| 0.0044 | 0.0016 | 0.00494 | 0.0044 | 154 | 0.00555 |
| 0.00217 | 0.00083 | 0.00245 | 0.00217 | 80 | 0.00247 |
| 0.00602 | 0.00188 | 0.00666 | 0.00602 | 173 | 0.00781 |
| 0.00299 | 0.00113 | 0.00337 | 0.00299 | 110 | 0.00355 |
| 0.00620 | 0.00190 | 0.00685 | 0.00620 | 115 | 0.00742 |
| 0.00410 | 0.00152 | 0.00462 | 0.00410 | 147 | 0.00513 |

A3-7: Al 6061 / Al₂O₃ / 22p-T6 Critical Plane damage models calculated variables and

Parameters for Torsion Loading

| Brown-Miller Data | | | Fatemi-Socie Data | | |
|------------------------|-----------------------|-------------------------------------|------------------------|--------------------------|-------------------------------------|
| $\Delta\gamma_{max}/2$ | $\Delta\varepsilon_n$ | Brown-Miller Damage Parameter | $\Delta\gamma_{max}/2$ | $\sigma_{n_{max}}$ [MPa] | Fatemi-Socie Damage Parameter |
| 0.004 | 0 | 0.004 | 0.004 | 0 | 0.004 |
| 0.005 | 0 | 0.005 | 0.005 | 0 | 0.005 |
| 0.003 | 0 | 0.003 | 0.003 | 0 | 0.003 |
| 0.006 | 0 | 0.006 | 0.006 | 0 | 0.006 |
| 0.0055 | 0 | 0.0055 | 0.0055 | 0 | 0.0055 |
| 0.0066 | 0 | 0.0066 | 0.0066 | 0 | 0.0066 |
| 0.003 | 0 | 0.003 | 0.003 | 0 | 0.003 |
| 0.004 | 0 | 0.004 | 0.004 | 0 | 0.004 |
| 0.006 | 0 | 0.006 | 0.006 | 0 | 0.006 |

A3-8: Al 6061 / Al₂O₃ / 22p-T6 Critical Plane damage models calculated variables and

Parameters for bi-axial in-phase loading

| Brown-Miller Data | | | Fatemi-Socie Data | | |
|------------------------|-----------------------|-------------------------------------|------------------------|--------------------------|-------------------------------------|
| $\Delta\gamma_{max}/2$ | $\Delta\varepsilon_n$ | Brown-Miller Damage Parameter | $\Delta\gamma_{max}/2$ | $\sigma_{n_{max}}$ [MPa] | Fatemi-Socie Damage Parameter |
| 0.00415 | -0.00015 | 0.0041 | 0.00415 | 214 | 0.00567 |
| 0.00564 | -0.00064 | 0.00542 | 0.00564 | 268 | 0.00822 |
| 0.00307 | -0.00007 | 0.00305 | 0.00307 | 161 | 0.00392 |
| 0.00198 | 0.00002 | 0.00199 | 0.00198 | 107 | 0.00234 |
| 0.00561 | -0.00061 | 0.00540 | 0.00561 | 268 | 0.00817 |
| 0.00430 | -0.0003 | 0.00420 | 0.00430 | 214 | 0.00588 |
| 0.00298 | 0.00002 | 0.00299 | 0.00298 | 161 | 0.00380 |
| 0.00198 | 0.00002 | 0.00199 | 0.00198 | 107 | 0.00234 |

A3-9: Al 6061 / SiC / 17w-T6 Critical Plane damage models calculated variables and Parameters

for $\lambda=0$ (pure tension)

| Brown-Miller Data | | | Fatemi-Socie Data | | |
|------------------------|-----------------------|-------------------------------------|------------------------|--------------------------|-------------------------------------|
| $\Delta\gamma_{max}/2$ | $\Delta\varepsilon_n$ | Brown-Miller Damage Parameter | $\Delta\gamma_{max}/2$ | $\sigma_{n_{max}}$ [MPa] | Fatemi-Socie Damage Parameter |
| 0.002883 | 0.00151 | 0.00339 | 0.002883 | 100 | 0.00342 |
| 0.002333 | 0.00123 | 0.00275 | 0.002333 | 82 | 0.00269 |

A3-10: Al 6061 / SiC / 17w-T6 Critical Plane damage models calculated variables and

Parameters for $\lambda=\infty$ (pure shear)

| Brown-Miller Data | | | Fatemi-Socie Data | | |
|------------------------|-----------------------|-------------------------------------|------------------------|--------------------------|-------------------------------------|
| $\Delta\gamma_{max}/2$ | $\Delta\varepsilon_n$ | Brown-Miller Damage Parameter | $\Delta\gamma_{max}/2$ | $\sigma_{n_{max}}$ [MPa] | Fatemi-Socie Damage Parameter |
| 0.002191 | 0 | 0.002191 | 0.002191 | 0 | 0.002191 |
| 0.002037 | 0 | 0.002037 | 0.002037 | 0 | 0.002037 |

A3-11: Al 6061 / SiC / 17w-T6 Critical Plane damage models calculated variables and
Parameters for $\lambda=0.5$ (in-phase bi-axial tension-torsion)

| Brown-Miller Data | | | Fatemi-Socie Data | | |
|------------------------|--------------------|-------------------------------------|------------------------|--------------------------|-------------------------------------|
| $\Delta\gamma_{max}/2$ | $\Delta\epsilon_n$ | Brown-Miller Damage Parameter | $\Delta\gamma_{max}/2$ | $\sigma_{n_{max}}$ [MPa] | Fatemi-Socie Damage Parameter |
| 0.0027 | 0.0013 | 0.003133 | 0.0027 | 85 | 0.00313 |
| 0.00253 | 0.0012 | 0.002931 | 0.00253 | 79 | 0.002903 |

A3-12: Al 6061 / SiC / 17w-T6 Critical Plane damage models calculated variables and

Parameters for $\lambda=1$ (in-phase bi-axial tension-torsion)

| Brown-Miller Data | | | Fatemi-Socie Data | | |
|------------------------|-----------------------|-------------------------------------|------------------------|--------------------------|-------------------------------------|
| $\Delta\gamma_{max}/2$ | $\Delta\varepsilon_n$ | Brown-Miller Damage Parameter | $\Delta\gamma_{max}/2$ | $\sigma_{n_{max}}$ [MPa] | Fatemi-Socie Damage Parameter |
| 0.002486 | 0.000917 | 0.002798 | 0.002486 | 61 | 0.002772 |
| 0.002486 | 0.000917 | 0.002798 | 0.002486 | 61 | 0.002772 |
| 0.002486 | 0.000917 | 0.002798 | 0.002486 | 61 | 0.002772 |
| 0.002194 | 0.000813 | 0.002471 | 0.002194 | 55 | 0.002419 |

A3-13: Al 6061 / SiC / 17w-T6 Critical Plane damage models calculated variables and

Parameters for $\lambda=2$ (in-phase bi-axial tension-torsion)

| Brown-Miller Data | | | Fatemi-Socie Data | | |
|------------------------|--------------------|-------------------------------------|------------------------|--------------------------|-------------------------------------|
| $\Delta\gamma_{max}/2$ | $\Delta\epsilon_n$ | Brown-Miller Damage Parameter | $\Delta\gamma_{max}/2$ | $\sigma_{n_{max}}$ [MPa] | Fatemi-Socie Damage Parameter |
| 0.00229 | 0.0005 | 0.002472 | 0.00229 | 35 | 0.002445 |
| 0.00216 | 0.0005 | 0.002326 | 0.00216 | 33 | 0.002292 |

A3-14: Ti-6Al-4V / TiC /10p Critical Plane damage models calculated variables and Parameters
for tensile loading

| Brown-Miller Data | | | Fatemi-Socie Data | | |
|------------------------|-----------------------|-------------------------------------|------------------------|------------------------|-------------------------------------|
| $\Delta\gamma_{max}/2$ | $\Delta\varepsilon_n$ | Brown-Miller Damage Parameter | $\Delta\gamma_{max}/2$ | $\sigma_{n,max}$ [MPa] | Fatemi-Socie Damage Parameter |
| 0.00336 | 0.005 | 0.005062 | 0.00336 | 94 | 0.00368 |
| 0.00338 | 0.005 | 0.00508 | 0.00338 | 94 | 0.00360 |
| 0.00195 | 0.003 | 0.002975 | 0.00195 | 71 | 0.00205 |

A3-15: Ti-6Al-4V / TiC / 10p Critical Plane damage models calculated variables and Parameters
for torsion loading

| Brown-Miller Data | | | Fatemi-Socie Data | | |
|------------------------|-----------------------|-------------------------------------|------------------------|--------------------------|-------------------------------------|
| $\Delta\gamma_{max}/2$ | $\Delta\varepsilon_n$ | Brown-Miller Damage Parameter | $\Delta\gamma_{max}/2$ | $\sigma_{n_{max}}$ [MPa] | Fatemi-Socie Damage Parameter |
| 0.00390 | 0 | 0.00390 | 0.00390 | 0 | 0.00390 |
| 0.00393 | 0 | 0.00393 | 0.00393 | 0 | 0.00393 |

A3-16: Ti-6Al-4V / TiC / 10p Critical Plane damage models calculated variables and Parameters
 for 90° out of phase bi-axial tension-torsion loading

| Brown-Miller Data | | | Fatemi-Socie Data | | |
|------------------------|-----------------------|-------------------------------------|------------------------|--------------------------|-------------------------------------|
| $\Delta\gamma_{max}/2$ | $\Delta\varepsilon_n$ | Brown-Miller Damage Parameter | $\Delta\gamma_{max}/2$ | $\sigma_{n_{max}}$ [MPa] | Fatemi-Socie Damage Parameter |
| 0.010977 | 0.0035 | 0.0122 | 0.010977 | 163 | 0.0122 |

A4-1: Al 6061 / Al₂O₃ / 20p-T6 Energy damage model calculated variables and parameters for

Tensile loading (solid shaft test specimen)

| Axial Elastic Deformation $(\Delta\varepsilon_e/2)$ | Axial Plastic Deformation $(\Delta\varepsilon_p/2)$ | Axial Elastic Strain Energy (W_{ten}^e) | Axial Plastic Strain Energy (W_{ten}^p) | Total Axial Strain Energy (W_{ten}) |
|---|---|---|---|---|
| 0.004082 | 0.003918 | 0.808 | 5.39 | 6.203 |
| 0.004021 | 0.001979 | 0.784 | 2.684 | 3.468 |
| 0.003969 | 0.002031 | 0.764 | 2.712 | 3.483 |
| 0.00369 | 0.001309 | 0.661 | 1.630 | 2.290 |
| 0.003722 | 0.001278 | 0.671 | 1.604 | 2.276 |
| 0.003784 | 0.001216 | 0.694 | 1.552 | 2.246 |
| 0.00299 | 1.03E-05 | 0.433 | 0.0103 | 0.444 |
| 0.002887 | 0.000113 | 0.404 | 0.110 | 0.514 |
| 0.002701 | 0.000299 | 0.354 | 0.2723 | 0.626 |
| 0.002938 | 6.19E-05 | 0.419 | 0.0613 | 0.480 |

A4-2: Al 6061 / Al₂O₃ / 20p-T6 Energy damage model calculated variables and parameters for
Torsion loading (solid shaft test specimen)

| Shear Elastic Deformation ($\Delta\gamma_e/2$) | Shear Plastic Deformation ($\Delta\gamma_p/2$) | Shear Elastic Strain Energy (W_{shear}^e) | Shear Plastic Strain Energy (W_{shear}^p) | Total Shear Strain Energy (W_{shear}) |
|--|--|---|---|---|
| 0.00605 | 0.00795 | 0.677 | 5.605 | 6.2827 |
| 0.00556 | 0.003036 | 0.573 | 1.9685 | 2.5416 |
| 0.00556 | 0.003036 | 0.573 | 1.9685 | 2.5416 |
| 0.00521 | 0.001787 | 0.503 | 1.0856 | 1.5886 |
| 0.00445 | 0.000543 | 0.3676 | 0.2821 | 0.6498 |

A4-3: Al 6061 / Al₂O₃ / 20p-T6 Energy damage model calculated variables and parameters for combined tension-torsion loading (solid shaft test specimen)

| Axial Elastic Strain ($\Delta\varepsilon_e/2$) | Axial Plastic Strain ($\Delta\varepsilon_p/2$) | Axial Elastic Strain Energy (W_{ten}^e) | Axial Plastic Strain Energy (W_{ten}^p) | Shear Elastic Strain ($\Delta\gamma_e/2$) | Shear Plastic Strain ($\Delta\gamma_p/2$) | Shear Elastic Strain Energy (W_{shear}^e) | Shear Plastic Strain Energy (W_{shear}^p) | Total Strain Energy (W) |
|--|--|---|---|---|---|---|---|---|
| 0.00247 | 0.00333 | 0.2969 | 2.781 | 0.00474 | 0.00524 | 0.4183 | 2.9078 | 6.4036 |
| 0.00238 | 0.00162 | 0.275 | 1.3024 | 0.00437 | 0.00262 | 0.3544 | 1.339 | 3.2708 |
| 0.00238 | 0.00162 | 0.275 | 1.3024 | 0.00437 | 0.00262 | 0.3544 | 1.339 | 3.2708 |
| 0.00222 | 0.00068 | 0.2382 | 0.512 | 0.00389 | 0.00111 | 0.28 | 0.5036 | 1.53386 |
| 0.00222 | 0.00068 | 0.2382 | 0.512 | 0.00389 | 0.00111 | 0.28 | 0.5036 | 1.53386 |
| 0.00206 | 0.00024 | 0.2061 | 0.166 | 0.00343 | 0.00057 | 0.2178 | 0.2278 | 0.8177 |
| 0.00198 | 2.06E-05 | 0.1900 | 0.01379 | 0.00313 | 0.00036 | 0.1817 | 0.134 | 0.5195 |
| 0.00198 | 2.06E-05 | 0.1900 | 0.01379 | 0.00313 | 0.00036 | 0.1817 | 0.134 | 0.5195 |
| 0.00167 | 2.99E-05 | 0.1352 | 0.01687 | 0.00275 | 0.00024 | 0.1405 | 0.0786 | 0.3713 |

A4-4: Al 6061 / Al₂O₃ / 22p-T6 Energy damage model calculated variables and parameters for
tension loading

| Axial Elastic Deformation ($\Delta\varepsilon_e/2$) | Axial Plastic Deformation ($\Delta\varepsilon_p/2$) | Axial Elastic Strain Energy (W_{ten}^e) | Axial Plastic Strain Energy (W_{ten}^p) | Total Axial Strain Energy (W_{ten}) |
|---|---|---|---|---|
| 0.002869 | 0.000131 | 0.4404 | 0.1399 | 0.5803 |
| 0.00199 | 0.000001 | 0.2138 | 0.0008356 | 0.2145 |
| 0.002869 | 0.000131 | 0.4404 | 0.1399 | 0.58034 |
| 0.001500 | 0.0000 | 0.1203 | 0 | 0.1203 |
| 0.003239 | 0.000711 | 0.5613 | 0.85817 | 1.4195 |
| 0.002060 | 0.00000 | 0.227 | 0 | 0.227 |
| 0.002149 | 0.001901 | 0.2471 | 1.52276 | 1.76985 |
| 0.002745 | 0.000065 | 0.40316 | 0.066367 | 0.4695 |

A4-5: Al 6061 / Al₂O₃ / 22p-T6 Energy damage model calculated variables and parameters for
shear loading

| Shear Elastic Deformation ($\Delta\gamma_e/2$) | Shear Plastic Deformation ($\Delta\gamma_p/2$) | Shear Elastic Strain Energy (W_{shear}^e) | Shear Plastic Strain Energy (W_{shear}^p) | Total Shear Strain Energy (W_{shear}) |
|--|--|---|---|---|
| 0.003967 | 3.2833E-05 | 0.32137 | 0.01853 | 0.33991 |
| 0.004658 | 0.0003418 | 0.4431 | 0.22653 | 0.66962 |
| 0.002998 | 1.4985E-06 | 0.1835 | 0.0006393 | 0.1842 |
| 0.005012 | 0.000987 | 0.51305 | 0.7042 | 1.21728 |
| 0.004863 | 0.000637 | 0.4829 | 0.4407 | 0.923635 |
| 0.0051477 | 0.0014522 | 0.54112 | 1.0636 | 1.604705 |
| 0.002998 | 1.4985E-06 | 0.18359 | 0.000639 | 0.1842357 |
| 0.003967 | 3.2833E-05 | 0.32138 | 0.018531 | 0.33991 |
| 0.0050129 | 0.000987 | 0.51305 | 0.704224 | 1.21728 |

A4-6: Al 6061 / Al₂O₃ / 22p-T6 Energy damage model calculated variables and parameters for combined in-phase tension-torsion loading

| Axial Elastic Strain ($\Delta\varepsilon_e/2$) | Axial Plastic Strain ($\Delta\varepsilon_p/2$) | Axial Elastic Strain Energy (W_{ten}^e) | Axial Plastic Strain Energy (W_{ten}^p) | Shear Elastic Strain ($\Delta\gamma_e/2$) | Shear Plastic Strain ($\Delta\gamma_p/2$) | Shear Elastic Strain Energy (W_{shear}^e) | Shear Plastic Strain Energy (W_{shear}^p) | Total Strain Energy (W) |
|---|---|---|---|--|--|---|---|--------------------------------------|
| 0.00199 | 9.34E-06 | 0.212 | 0.00693 | 0.00409 | 5.5E-05 | 0.343 | 0.03228 | 0.8133 |
| 0.00248 | 1.49E-05 | 0.330 | 0.01385 | 0.00491 | 0.00074 | 0.4923 | 0.5203 | 1.701 |
| 0.0015 | 0 | 0.120 | 0 | 0.00307 | 3.7E-06 | 0.1922 | 0.00162 | 0.4349 |
| 0.001 | 0 | 0.0535 | 0 | 0.00198 | 4.8E-09 | 0.08005 | 1.38E-06 | 0.187 |
| 0.00248 | 1.49E-05 | 0.3304 | 0.01385 | 0.00489 | 0.00071 | 0.49016 | 0.4953 | 1.6739 |
| 0.00199 | 9.34E-06 | 0.212 | 0.00693 | 0.00422 | 8.35E-05 | 0.3639 | 0.05015 | 0.8519 |
| 0.0015 | 0 | 0.12 | 0 | 0.00298 | 2.15E-06 | 0.1817 | 0.18255 | 0.4233 |
| 0.001 | 0 | 0.0535 | 0 | 0.00198 | 3.91E-09 | 0.08005 | 0.08005 | 0.187 |

A4-7: Al 6061 / SiC / 17w-T6 Energy damage model calculated variables and parameters for

$\alpha=0$ (tension)

| Axial Elastic Deformation $(\Delta\varepsilon_e/2)$ | Axial Plastic Deformation $(\Delta\varepsilon_p/2)$ | Axial Elastic Strain Energy (W_{ten}^e) | Axial Plastic Strain Energy (W_{ten}^p) | Total Axial Strain Energy (W_{ten}) |
|---|---|---|---|---|
| 0.002153 | 4.17E-05 | 0.21458 | 0.024801 | 0.239382 |
| 0.001768 | 1.09E-05 | 0.14479 | 0.005296 | 0.150089 |

A4-8: Al 6061 / SiC / 17w-T6 Energy damage model calculated variables and parameters for

$\alpha=\infty$ (Pure shear)

| Shear Elastic Deformation $(\Delta\gamma_e/2)$ | Shear Plastic Deformation $(\Delta\gamma_p/2)$ | Shear Elastic Strain Energy (W_{shear}^e) | Shear Plastic Strain Energy (W_{shear}^p) | Total Shear Strain Energy (W_{shear}) |
|--|--|---|---|---|
| 0.00416 | 0.000223 | 0.30576 | 0.097801 | 0.403563 |
| 0.003924 | 0.00015 | 0.272114 | 0.061891 | 0.334004 |

A4-9: Al 6061 / SiC / 17w-T6 Energy damage model calculated variables and parameters for

$\alpha=0.5$ (in-phase combined tension-torsion)

| Axial Elastic Strain ($\Delta\varepsilon_e/2$) | Axial Plastic Strain ($\Delta\varepsilon_p/2$) | Axial Elastic Strain Energy (W_{ten}^e) | Axial Plastic Strain Energy (W_{ten}^p) | Shear Elastic Strain ($\Delta\gamma_e/2$) | Shear Plastic Strain ($\Delta\gamma_p/2$) | Shear Elastic Strain Energy (W_{shear}^e) | Shear Plastic Strain Energy (W_{shear}^p) | Total Strain Energy (W) |
|--|--|---|---|---|---|---|---|---|
| 0.00183 | 1.37E-05 | 0.1552 | 0.00695 | 0.00239 | 5.13E-06 | 0.1016 | 0.00129 | 0.26503 |
| 0.00171 | 8.84E-06 | 0.1364 | 0.00419 | 0.00225 | 3.30E-06 | 0.0893 | 0.00078 | 0.2307 |

A4-10: Al 6061 / SiC / 17w-T6 Energy damage model calculated variables and parameters for

$\alpha=1.0$ (in-phase combined tension-torsion)

| Axial Elastic Strain ($\Delta\varepsilon_e/2$) | Axial Plastic Strain ($\Delta\varepsilon_p/2$) | Axial Elastic Strain Energy (W_{ten}^e) | Axial Plastic Strain Energy (W_{ten}^p) | Shear Elastic Strain ($\Delta\gamma_e/2$) | Shear Plastic Strain ($\Delta\gamma_p/2$) | Shear Elastic Strain Energy (W_{shear}^e) | Shear Plastic Strain Energy (W_{shear}^p) | Total Strain Energy (W) |
|--|--|---|---|---|---|---|---|---|
| 0.00133 | 1.53E-06 | 0.0817 | 0.00056 | 0.00348 | 6.58E-05 | 0.2140 | 0.02412 | 0.3204 |
| 0.00133 | 1.53E-06 | 0.0817 | 0.00056 | 0.00348 | 6.58E-05 | 0.2140 | 0.02412 | 0.3204 |
| 0.00133 | 1.53E-06 | 0.0817 | 0.00056 | 0.00348 | 6.58E-05 | 0.2140 | 0.02412 | 0.3204 |
| 0.00118 | 6.73E-07 | 0.0643 | 0.00022 | 0.00309 | 2.9E-05 | 0.1685 | 0.0095 | 0.2424 |

A4-11: Al 6061 / SiC / 17w-T6 Energy damage model calculated variables and parameters for $\alpha=2.0$ (in-phase combined tension-torsion)

| Axial Elastic Strain ($\Delta\varepsilon_e/2$) | Axial Plastic Strain ($\Delta\varepsilon_p/2$) | Axial Elastic Strain Energy (W_{ten}^e) | Axial Plastic Strain Energy (W_{ten}^p) | Shear Elastic Strain ($\Delta\gamma_e/2$) | Shear Plastic Strain ($\Delta\gamma_p/2$) | Shear Elastic Strain Energy (W_{shear}^e) | Shear Plastic Strain Energy (W_{shear}^p) | Total Strain Energy (W) |
|--|--|---|---|---|---|---|---|---|
| 0.00076 | 3.28E-08 | 0.0267 | 6.86E-06 | 0.00397 | 0.00016 | 0.279 | 0.0681 | 0.373 |
| 0.00072 | 2.29E-08 | 0.0239 | 4.54E-06 | 0.00377 | 0.00011 | 0.251 | 0.0451 | 0.320 |

A4-12: Ti-6Al-4V / TiC / 10p Energy damage model calculated variables and parameters

(tension)

| Axial Elastic Deformation $(\Delta\varepsilon_e/2)$ | Axial Plastic Deformation $(\Delta\varepsilon_p/2)$ | Axial Elastic Strain Energy (W_{ten}^e) | Axial Plastic Strain Energy (W_{ten}^p) | Total Axial Strain Energy (W_{ten}) |
|---|---|---|---|---|
| 0.00388 | 0.00112 | 0.7056 | 1.122 | 1.828 |
| 0.00371 | 0.001296 | 0.695 | 1.298 | 1.993 |
| 0.00295 | 5.36E-05 | 0.406 | 0.0407 | 0.446 |

A4-13: Ti-6Al-4V / TiC / 10p Energy damage model calculated variables and parameters (shear)

| Shear Elastic Deformation ($\Delta\gamma_e/2$) | Shear Plastic Deformation ($\Delta\gamma_p/2$) | Shear Elastic Strain Energy (W_{shear}^e) | Shear Plastic Strain Energy (W_{shear}^p) | Total Shear Strain Energy (W_{shear}) |
|--|--|---|---|---|
| 0.00596 | 4.32E-05 | 0.557 | 0.02135 | 0.57839 |
| 0.00568 | 0.000322 | 0.522 | 0.1591 | 0.6815 |

A4-14: Ti-6Al-4V / TiC / 10p Energy damage model calculated variables and parameters for 90°
out-of-phase combined tension-torsion

| Axial Elastic Strain ($\Delta\varepsilon_e/2$) | Axial Plastic Strain ($\Delta\varepsilon_p/2$) | Axial Elastic Strain Energy (W_{ten}^e) | Axial Plastic Strain Energy (W_{ten}^p) | Shear Elastic Strain ($\Delta\gamma_e/2$) | Shear Plastic Strain ($\Delta\gamma_p/2$) | Shear Elastic Strain Energy (W_{shear}^e) | Shear Plastic Strain Energy (W_{shear}^p) | Total Strain Energy (W) |
|---|---|---|---|--|--|---|---|--------------------------------------|
| 0.00327 | 0.00023 | 0.5312 | 0.2008 | 0.00555 | 0.00045 | 0.492 | 0.2161 | 1.44 |

A5-1: Al 6061 / Al₂O₃ / 20p-T6 Critical Plane-Energy damage model calculated variables and parameters for Tensile loading (solid shaft test specimen)

| <i>Principal Strains</i> | | | <i>Principal Stresses [MPa]</i> | | | <i>v_{eff}</i> | Critical Plane – Energy Damage |
|--------------------------|--------------|--------------|---------------------------------|------------|------------|------------------------|--------------------------------|
| ϵ_1 | ϵ_2 | ϵ_3 | σ_1 | σ_2 | σ_3 | | |
| 0.00518 | -0.00164 | -0.00046 | 297 | 0 | 0 | 0.409 | 0.0845 |
| 0.00389 | -0.00121 | -0.00031 | 292 | 0 | 0 | 0.402 | 0.0630 |
| 0.00390 | -0.00119 | -0.00029 | 289 | 0 | 0 | 0.397 | 0.06258 |
| 0.00328 | -0.00094 | -0.00015 | 269 | 0 | 0 | 0.375 | 0.04983 |
| 0.00328 | -0.00094 | -0.00016 | 271 | 0 | 0 | 0.376 | 0.05015 |
| 0.00366 | -0.00097 | -0.0002 | 272 | 0 | 0 | 0.387 | 0.05029 |
| 0.00198 | -0.00054 | -6.1E-05 | 217 | 0 | 0 | 0.360 | 0.02463 |
| 0.001982 | -0.00054 | -5.4E-05 | 210 | 0 | 0 | 0.354 | 0.02387 |
| 0.001968 | -0.00056 | -9.7E-05 | 196 | 0 | 0 | 0.376 | 0.02184 |
| 0.001968 | -0.00056 | -9.5E-05 | 214 | 0 | 0 | 0.375 | 0.02378 |

A5-2: Al 6061 / Al₂O₃ / 20p-T6 Critical Plane-Energy damage model calculated variables and parameters for Torsion loading (solid shaft test specimen)

| <i>Principal Strains</i> | | | <i>Principal Stresses [MPa]</i> | | | <i>v_{eff}</i> | Critical Plane – Energy Damage |
|--------------------------|--------------|--------------|---------------------------------|------------|------------|------------------------|--------------------------------|
| ϵ_1 | ϵ_2 | ϵ_3 | σ_1 | σ_2 | σ_3 | | |
| 0.007 | 0 | -0.007 | 224 | 0 | -224 | 0.4179 | 0.057089 |
| 0.0043 | 0 | -0.0043 | 206 | 0 | -206 | 0.377 | 0.03225 |
| 0.0043 | 0 | -0.0043 | 206 | 0 | -206 | 0.377 | 0.03225 |
| 0.0035 | 0 | -0.0035 | 193 | 0 | -193 | 0.358 | 0.02459 |
| 0.0025 | 0 | -0.0025 | 165 | 0 | -165 | 0.331 | 0.01502 |

A5-3: Al 6061 / Al₂O₃ / 20p-T6 Critical Plane-Energy damage model calculated variables and parameters for combined in-phase tension-torsion (solid shaft test specimen)

| <i>Principal Strains</i> | | | <i>Principal Stresses [MPa]</i> | | | <i>v_{eff}</i> | Critical Plane – Energy Damage |
|--------------------------|--------------|--------------|---------------------------------|------------|------------|------------------------|--------------------------------|
| ϵ_1 | ϵ_2 | ϵ_3 | σ_1 | σ_2 | σ_3 | | |
| 0.0058 | -0.00243 | -0.00243 | 333 | 0 | -93 | 0.419 | 0.07183 |
| 0.004 | -0.00155 | -0.00155 | 315 | 0 | -83 | 0.387 | 0.04805 |
| 0.004 | -0.00155 | -0.00155 | 315 | 0 | -83 | 0.387 | 0.04805 |
| 0.0029 | -0.00103 | -0.00103 | 287 | 0 | -72 | 0.355 | 0.03271 |
| 0.0029 | -0.00103 | -0.00103 | 287 | 0 | -72 | 0.355 | 0.03271 |
| 0.0023 | -0.00076 | -0.00076 | 262 | 0 | -62 | 0.330 | 0.02422 |
| 0.002 | -0.00062 | -0.00062 | 247 | 0 | -55 | 0.312 | 0.02023 |
| 0.002 | -0.00062 | -0.00062 | 247 | 0 | -55 | 0.312 | 0.02023 |
| 0.0017 | -0.00053 | -0.00053 | 211 | 0 | -49 | 0.313 | 0.01463 |

A5-4: Al 6061 / Al₂O₃ / 22p-T6 Critical Plane-Energy damage model calculated variables and parameters for tensile loading

| <i>Principal Strains</i> | | | <i>Principal Stresses [MPa]</i> | | | <i>v_{eff}</i> | Critical Plane – Energy Damage |
|--------------------------|----------------------|----------------------|---------------------------------|----------------------|----------------------|------------------------|--------------------------------|
| <i>ε₁</i> | <i>ε₂</i> | <i>ε₃</i> | <i>σ₁</i> | <i>σ₂</i> | <i>σ₃</i> | | |
| 0.003 | 0 | -0.014 | 307 | 0 | 0 | 0.318 | 0.03655 |
| 0.002 | 0 | -0.009 | 214 | 0 | 0 | 0.31 | 0.01727 |
| 0.003 | 0 | -0.0014 | 307 | 0 | 0 | 0.318 | 0.03655 |
| 0.0015 | 0 | -0.00067 | 161 | 0 | 0 | 0.31 | 0.00972 |
| 0.00395 | 0 | -0.000207 | 347 | 0 | 0 | 0.344 | 0.05113 |
| 0.00206 | 0 | -0.00093 | 220 | 0 | 0 | 0.31 | 0.01833 |
| 0.00405 | 0 | -0.000215 | 230 | 0 | 0 | 0.347 | 0.03453 |
| 0.00281 | 0 | -0.00129 | 294 | 0 | 0 | 0.314 | 0.03301 |

A5-5: Al 6061 / Al₂O₃ / 22p-T6 Critical Plane-Energy damage model calculated variables and parameters for Shear loading

| <i>Principal Strains</i> | | | <i>Principal Stresses [MPa]</i> | | | <i>v_{eff}</i> | Critical Plane – Energy Damage |
|--------------------------|--------------|--------------|---------------------------------|------------|------------|------------------------|--------------------------------|
| ϵ_1 | ϵ_2 | ϵ_3 | σ_1 | σ_2 | σ_3 | | |
| 0.002 | -0.002 | 0 | 163 | -163 | 0 | 0.188 | 0.0195 |
| 0.0025 | -0.0025 | 0 | 204 | -204 | 0 | 0.21 | 0.02832 |
| 0.0015 | -0.0015 | 0 | 122 | -122 | 0 | 0.17 | 0.01143 |
| 0.003 | -0.003 | 0 | 245 | -245 | 0 | 0.231 | 0.03785 |
| 0.00275 | -0.00275 | 0 | 224 | -224 | 0 | 0.214 | 0.0339 |
| 0.0033 | -0.0033 | 0 | 269 | -269 | 0 | 0.247 | 0.04317 |
| 0.0015 | -0.0015 | 0 | 122 | -122 | 0 | 0.192 | 0.010852 |
| 0.002 | -0.002 | 0 | 163 | -163 | 0 | 0.204 | 0.01851 |
| 0.003 | -0.003 | 0 | 245 | -245 | 0 | 0.233 | 0.03753 |

A5-6: Al 6061 / Al₂O₃ / 22p-T6 Critical Plane-Energy damage model calculated variables and parameters for in-phase combined tension-torsion loading

| <i>Principal Strains</i> | | | <i>Principal Stresses [MPa]</i> | | | | |
|--------------------------|--------------|--------------|---------------------------------|------------|------------|-------------|--------------------------------|
| ϵ_1 | ϵ_2 | ϵ_3 | σ_1 | σ_2 | σ_3 | ν_{eff} | Critical Plane – Energy Damage |
| 0.002 | 0.002 | -0.00215 | 214 | 214 | 0 | 0.35 | 0.0503 |
| 0.0025 | 0.0025 | -0.00314 | 267 | 267 | 0 | 0.386 | 0.0797 |
| 0.0015 | 0.0015 | -0.00157 | 161 | 161 | 0 | 0.344 | 0.0285 |
| 0.001 | 0.001 | -0.00098 | 107 | 107 | 0 | 0.329 | 0.0125 |
| 0.0025 | 0.0025 | -0.00311 | 267 | 267 | 0 | 0.383 | 0.0796 |
| 0.002 | 0.002 | -0.0023 | 214 | 214 | 0 | 0.3655 | 0.0507 |
| 0.0015 | 0.0015 | -0.00148 | 161 | 161 | 0 | 0.331 | 0.0281 |
| 0.001 | 0.001 | -0.00098 | 107 | 107 | 0 | 0.3288 | 0.0125 |

A5-7: Al 6061 / SiC / 17w-T6 Critical Plane-Energy damage model calculated variables and parameters for $\alpha=0$ (tension)

| <i>Principal Strains</i> | | | <i>Principal Stresses [MPa]</i> | | | <i>v_{eff}</i> | Critical Plane – Energy Damage |
|--------------------------|--------------|--------------|---------------------------------|------------|------------|------------------------|---------------------------------------|
| ϵ_1 | ϵ_2 | ϵ_3 | σ_1 | σ_2 | σ_3 | | |
| 0.002195 | -0.00069 | -0.00069 | 199 | 0 | 0 | 0.314 | 0.01143 |
| 0.001779 | -0.00055 | -0.00055 | 164 | 0 | 0 | 0.311 | 0.00762 |

A5-8: Al 6061 / SiC / 17w-T6 Critical Plane-Energy damage model calculated variables and parameters for $\alpha=\infty$ (Shear)

| <i>Principal Strains</i> | | | <i>Principal Stresses [MPa]</i> | | | | |
|--------------------------|--------------|--------------|---------------------------------|------------|------------|-------------|--------------------------------|
| ϵ_1 | ϵ_2 | ϵ_3 | σ_1 | σ_2 | σ_3 | ν_{eff} | Critical Plane – Energy Damage |
| 0.001096 | 0 | -0.001096 | 147 | 0 | -147 | 0.320 | 0.008418 |
| 0.001018 | 0 | -0.001018 | 139 | 0 | -139 | 0.317 | 0.007381 |

A5-9: Al 6061 / SiC / 17w-T6 Critical Plane-Energy damage model calculated variables and parameters for $\alpha=0.5$ (In-phase combined tension-torsion)

| <i>Principal Strains</i> | | | <i>Principal Stresses [MPa]</i> | | | ν_{eff} | Critical Plane – Energy Damage |
|--------------------------|--------------|--------------|---------------------------------|------------|------------|-------------|--------------------------------|
| ϵ_1 | ϵ_2 | ϵ_3 | σ_1 | σ_2 | σ_3 | | |
| 0.001985 | -0.00057 | -0.00072 | 205 | 0 | -35 | 0.311 | 0.01227 |
| 0.001858 | -0.00054 | -0.00067 | 192 | 0 | -33 | 0.311 | 0.009887 |

A5-10: Al 6061 / SiC / 17w-T6 Critical Plane-Energy damage model calculated variables and parameters for $\alpha=1.0$ (In-phase combined tension-torsion)

| <i>Principal Strains</i> | | | <i>Principal Stresses [MPa]</i> | | | | |
|--------------------------|--------------|--------------|---------------------------------|------------|------------|-------------|--------------------------------|
| ϵ_1 | ϵ_2 | ϵ_3 | σ_1 | σ_2 | σ_3 | ν_{eff} | Critical Plane – Energy Damage |
| 0.001702 | -0.00041 | -0.00078 | 199 | 0 | -76 | 0.31 | 0.010405 |
| 0.001702 | -0.00041 | -0.00078 | 199 | 0 | -76 | 0.31 | 0.010405 |
| 0.001702 | -0.00041 | -0.00078 | 199 | 0 | -76 | 0.31 | 0.010405 |
| 0.001504 | -0.00037 | -0.00069 | 177 | 0 | -67 | 0.3102 | 0.008154 |

A5-11: Al 6061 / SiC / 17w-T6 Critical Plane-Energy damage model calculated variables and parameters for $\alpha=2.0$ (In-phase combined tension-torsion)

| <i>Principal Strains</i> | | | <i>Principal Stresses [MPa]</i> | | | ν_{eff} | Critical Plane – Energy Damage |
|--------------------------|--------------|--------------|---------------------------------|------------|------------|-------------|--------------------------------|
| ϵ_1 | ϵ_2 | ϵ_3 | σ_1 | σ_2 | σ_3 | | |
| 0.001408 | -0.00024 | -0.00089 | 180 | 0 | -110 | 0.31 | 0.009153 |
| 0.001327 | -0.00022 | -0.00083 | 171 | 0 | -104 | 0.31 | 0.008172 |

A5-12: Ti-6Al-4V / TiC / 10p Critical Plane-Energy damage model calculated variables and parameters for uniaxial loading

| <i>Principal Strains</i> | | | <i>Principal Stresses [MPa]</i> | | | <i>v_{eff}</i> | Critical Plane – Energy Damage |
|--------------------------|--------------|--------------|---------------------------------|------------|------------|------------------------|--------------------------------|
| ϵ_1 | ϵ_2 | ϵ_3 | σ_1 | σ_2 | σ_3 | | |
| 0.0025 | -0.00083 | -0.00083 | 311 | 0 | 0 | 0.334 | 0.02843 |
| 0.0025 | -0.00084 | -0.00084 | 311 | 0 | 0 | 0.337 | 0.028433 |
| 0.0015 | -0.00045 | -0.00045 | 233 | 0 | 0 | 0.300 | 0.012797 |

A5-13: Ti-6Al-4V / TiC / 10p Critical Plane-Energy damage model calculated variables and parameters for Shear loading

| <i>Principal Strains</i> | | | <i>Principal Stresses [MPa]</i> | | | ν_{eff} | Critical Plane – Energy Damage |
|--------------------------|--------------|--------------|---------------------------------|------------|------------|-------------|--------------------------------|
| ϵ_1 | ϵ_2 | ϵ_3 | σ_1 | σ_2 | σ_3 | | |
| 0.003 | -0.0009 | -0.0009 | 92 | 0 | -92 | 0.301 | 0.01318 |
| 0.003 | -0.00093 | -0.00093 | 92 | 0 | -92 | 0.311 | 0.01330 |

A5-14: Ti-6Al-4V / TiC / 10p Critical Plane-Energy damage model calculated variables and parameters for 90° out-of-phase biaxial loading

| <i>Principal Strains</i> | | | <i>Principal Stresses [MPa]</i> | | | | |
|--------------------------|--------------|--------------|---------------------------------|------------|------------|-------------|--------------------------------|
| ϵ_1 | ϵ_2 | ϵ_3 | σ_1 | σ_2 | σ_3 | ν_{eff} | Critical Plane – Energy Damage |
| 0.00669 | -0.0011 | -0.00429 | 403 | 0 | -78 | 0.313 | 0.111 |